HADROPRODUCTION OF D* → (K π) π

BY

THOMAS KNIGHT KROC

B.S.E.P., The Ohio State University, 1981

THESIS

Submitted in partial fulfillment of the requirements
for the degree of Doctor of Philosophy in Physics
in the Graduate College of the
University of Illinois at Urbana-Champaign, 1989

Urbana, Illinois

HADROPRODUCTION OF D* → (K π) π

Thomas Knight Kroc

Department of Physics

University of Illinois at Urbana-Champaign, 1989

A study of the decay $D^{*+} \to (K^- \pi^+) \pi^+$ (and charge conjugate) has been performed based on data taken from n-nucleus collisions by the experiment E400 at the Proton East area of FNAL. A signal was observed at the 3.3σ level that behaves properly under lifetime cuts. A method for determining the acceptance due to spectrometer geometry and analysis cuts was developed with the intention of making the acceptance as independent as possible of biases resulting from the production model chosen for the Monte Carlo studies that determined the acceptance. The acceptance was parameterized in two different ways chosen so that inconsistencies would expose any remaining model dependence. The cross-sections resulting from these two parameterizations were consistent and the average of the two is $\Delta\sigma \cdot$ Br $= 2.36 \pm .72$ (statistical) ± 1.18 (systematic) over the range $-.02 < x_F < .3$. A comparison is made between this cross-section and the cross-section found for the decay $D^* \to (K^+ K^-) \pi$, also measured by E400, over the more limited range $0.< x_F <.14$ and the two values are found to be statistically consistent. The cross-section from $D^* \to (K \pi) \pi$ is compared to cross-sections determined by LEBC, an experiment also using a hadron beam of energy similar to E400, with considerable disagreement although no explicit explanation is readily available. Both experiments, as well as many others, measure cross-sections that are considerably larger than lowest order QCD calculations.

Acknowledgements

Experimental work in high-energy physics is a group effort. Many people made contributions to the effort that made this thesis possible. I will mention some of them here.

The primary contributor was my advisor, Jim Wiss. He is able to maintain a firm grasp of all aspects of a high-energy physics experiment and always has a clear idea of where an analysis is in relation to the final goal. His ability to break complex analyses down into relatively simple and elegant mathematical models always amazes me. I hope I have been able to acquire some of this ability from him.

I would also like to thank my other collaborators from the University of Illinois. Mike Diesburg, who did much of the work with the vee's and their use in calibrating the experiment. John Filaseta, who did a lot of the early work with the data-aquisition system and who did a thorough job in mapping the magnetic fields. Calvin Shipbaugh, who was a major factor in the development of the Čerenkov algorithms.

My collaborators from the University of Colorado, Boulder, John Cumalat, Paul Coteus, Janice Enagonio, and Ray Ladbury were lots of fun to work with in the actual execution of the experiment. Paul deserves special recognition for his efforts in making the Vertex Chamber a useful device, without which the results presented in this thesis would not be possible.

Of my colleagues from Fermilab I especially want to thank Dave Harding for his guidance while working with the data-aquisition system and for his helpful advice as I continue my career. The other Fermilab collaborators who deserve mention are Morris Binkley, Joel Butler, Irwin Gaines, Peter Garbincius, Mike Gormley, John Haggerty, Paul Lebrun, and Jean Slaughter.

Back at the University of Illinois, special recognition is warranted for Dave Lesney and Jerry Wray who maintain our computer system. I am not familiar with the systems of many other institutions but despite my ignorance, I am confident in stating that they maintain one of the best.

On the personal side I want to foremost thank my parents for their love and support in laying the foundation on which all this work rests. I also thank my friends at the Wesley Foundation at the University of Illinois for their friendship and support. Last but definitely not least I thank Jen for her friendship and love.

Table of Contents

Chapter I: Introduction

In 1934, Fermi proposed a model for beta-decay[1,2], which involves the weak interaction, that was analogous to the electromagnetic transition (Quantum Electrodynamics or QED). In his beta-decay model, the neutron is transformed into a proton by the emission of an electron-neutrino pair through a contact-like interaction. This model had two problems. First, the model conserved parity and beta decay was later found to be parity-violating. Second, the cross-section for such contact-like processes diverges linearly as the center-of-mass energy goes to infinity. Such a divergence (in a single partial-wave) violates unitarity.

The first attempt to fix the problems mentioned above introduced a propagator, the intermediate-vector-boson (IVB), to mediate the weak interaction. Unlike the photon, the propagator of the electromagnetic interaction, the IVB's or W's are charged and massive. Unfortunately, having a massive propagator naively leads to a violation of gauge invariance. The W's had longitudinal components which ultimately caused processes such as $\nu\bar{\nu} \rightarrow W^+W^-$ to go to infinity in the high energy limit, again violating unitarity. Because QED does not have these problems, due to its gauge invariance, a gauge invariant theory was needed for the weak interaction. Over the period of 1961 to 1968, Glashow[3], Weinberg[4], and Salam[5] (GWS) and others developed such a theory based on spontaneous symmetry breaking to describe weak interactions between leptons.

Attempts to include quarks in the GWS model (using the three light quarks) inevitably lead to the existence of strangeness-changing neutral currents. A strangeness-changing neutral current allows processes such as $K_L^0 \rightarrow \mu^+\mu^-$ to proceed at a rate orders of magnitude larger than that observed in experiment. In 1970 Glashow, Iliopoulos, & Maiani[6] proposed a theory, that included a fourth quark, which canceled the unobserved strangeness-changing neutral currents. This fourth quark, the charmed quark (c), can be used to construct a number of high mass charm resonances. In 1974, the lowest-lying J/ψ meson (or charmonium, $c\bar{c}$) resonance was discovered simultaneously by experimenters at SPEAR[7] and BNL[8]. Since then a series of charmonium states have been seen, and in 1976, the lowest lying non-zero charmed (or open-charmed) mesons, the D mesons ($c\bar{u}$, $c\bar{d}$ and their antiparticles), were detected at SPEAR[9,10].

Currently, several open-charmed states are well established[11]: the D and D* mesons, the D_s^+(or F^+) meson, and the Λ_c, Σ_c, Ξ_c baryons.

Most of the data on the properties of charmed particles was obtained from e^+e^- annihilation. When the center-of-mass energy is considerably above charm threshold, the ratio of charm to non-charm events is close to one; whereas this ratio is of the order of 10^{-3} in hadroproduction and 10^{-2} in photoproduction. However, fixed target experiments offer unique experimental advantages to the study of charm particles. Even though the level of charm to background is much higher in e^+e^- interactions, the absolute production rates of charm are orders of magnitude higher in hadronic collisions. Therefore photoproduction and hadroproduction experiments have the ability to get very large samples of heavy-flavor states such as charm and beauty. These two production mechanisms also offer several "detection" advantages. One example is the use of lifetime-tagging techniques to isolate high statistics, clean, photoproduced signals as evidenced by the recent publications by E691[12]. Such large samples enable studies such as the establishment of limits on D^o - $\overline{D}^o$ mixing and hold out possibly the only hope of seeing CP-violation in the beauty sector. This thesis in particular is concerned with the hadroproduction of heavy-flavor states, namely charm.

A theoretical motivation for hadronic studies is that strong interactions have a running coupling constant, α_s, which is given by:

$$\alpha_s = \frac{12\pi}{(33 - 2f)\ln(Q^2/\Lambda^2)} \tag{I.1}$$

where $Q^2 \approx m_{c\bar{c}}^2$, f is the number of flavors, and Λ is the QCD scale ($\simeq 0.1$ GeV). Because $m_{c\bar{c}}$ is large (over 3 GeV), α_s is small, $\simeq .25$, so one hopes that low order QCD perturbation theory should be valid and that only the order α_s^2 diagrams need be considered (see Figure I.1).

In the parton model, the total charm cross-section in hadroproduction is given by

$$\sigma_{c\bar{c}} = \sum_{\substack{\text{distinct} \\ \text{subprocesses}}} \iint dx_1\, dx_2\, f_1(x_1, Q^2) f_2(x_2, Q^2)\, \hat{\sigma}(1 + 2 \rightarrow 3 + 4) \tag{I.2}$$

where $\hat{\sigma}$ is a subprocess cross-section. The subprocesses being considered include flavor-creation interactions (i.e. light quark-antiquark annihilation: $q\bar{q} \rightarrow c\bar{c}$, and

gluon-gluon fusion: $gg \rightarrow c\bar{c}$) as well as flavor-excitation interactions (i.e. $qc \rightarrow qc$ and $gc \rightarrow gc$). The interacting partons from the initial hadrons are described by fractional momentum distributions f_1 and f_2 which depend on the parton momentum fractions x_1 and x_2 and weakly depend on the momentum transferred squared, Q^2. Little is known about the sea-parton momentum distribution, but notice that if flavor excitation subprocesses are significant in charm hadroproduction, then the form of this distribution could be directly measured. To summarize, charm hadroproduction can provide a test for QCD predictions as well as possibly reveal details about the sea-parton momentum distributions.

The production of closed-charmed states (i.e. $c\bar{c}$ states) can be distinguished from the production of open-charmed states (i.e. states consisting of non-zero charm). Experimental evidence indicates rather clearly that the production rates of closed-charm can be interpreted as primarily originating from flavor creation subprocesses, i.e. $q\bar{q}$-annihilation and gg-fusion. Calculations show that central production via gg-fusion is the dominating subprocess at high energies[13-16], and the x-dependence of the gluon momentum distribution function within baryons obtained in hadroproduction can be expressed as $(1 - x)^5/x$ which is the form derived from counting rules[17,18] and is compatible with results from charm photoproduction[19,20].

But hadroproduction of open-charmed states is not well understood. Total charm cross-sections are currently found to be in the following approximate ranges:

- at $\sqrt{s} \approx 25$, $\sigma = 10 - 30$ μbarns/Nucleon

- at $\sqrt{s} \approx 35$, $\sigma = 40 - 60$ μbarns/Nucleon

- at $\sqrt{s} \approx 60$, $\sigma = 200 - 800$ μbarns/Nucleon.

However, as seen in Figure I.2 which is representative of some recent calculations [16,21], these values are quite a bit higher than is predicted.

Note that the interpretation of results from various charm hadroproduction experiments must be done cautiously. Crucial input parameters from model-based calculations may change cross-section estimates by a factor of 2 or more. Typically the systematic errors on the quoted cross-sections are 50% or more, which is largely due to the large

uncertainties in the branching ratios of most charmed particle decays and to the strong model dependence of results from those experiments which must extrapolate beyond their kinematic range of acceptance.

Figure I.2 mentioned above is based on a representative example of some the current theoretical work on heavy-quark production by Ellis, Quigg, and Sexton[16,21]. The results of $q\bar{q}$-annihilation and gg-fusion are considered. Figure I.2 shows the variation of the cross-section as a function of beam energy or $\sqrt{s}$ and Figure I.3 shows the differential cross-section $\frac{d\sigma}{dx_F}(\bar{x}_F)$ as a function of x_F. $x_F = 2\frac{P_{\parallel}}{\sqrt{s}}$, where $P_{\parallel}$ is the momentum of the D^* parallel to the direction of the incident neutron in the center-of-mass frame and $\sqrt{s}$ is the center-of-mass energy.

The differential cross-section for the gg-fusion component, as described in references 16 and 21, was used in the Monte Carlo studies for this thesis. The differential cross-section can be expressed in dimensionless variables as:

$$\frac{d\hat{\sigma}}{dr} = \frac{\overline{M}^2}{16\pi\hat{s}} \qquad (I.3)$$

with

$$\overline{M}^2 = \frac{g^2}{2VN}\left(\frac{V}{r(1-r)} - 2N^2\right)\left(r^2 + (1-r)^2 + \gamma - \left(\frac{\gamma}{2}\right)^2 \frac{1}{r(1-r)}\right) \qquad (I.4)$$

where:

- $V = N^2 - 1$

- N is the number of flavors, 3

- $\gamma = \frac{2\mathcal{M}^2}{p_1 \cdot p_2}$ where $\mathcal{M}$ is the mass of the two gluons

- $r = \frac{p_1 \cdot p_3}{p_1 \cdot p_2} \equiv \frac{1 - \beta\cos\theta}{2}$

where p_1 and p_2 are the four-momentum of the incoming gluons and p_3 and p_4 are the four momentum of the outgoing c and $\bar{c}$. Figure I.2 shows that the mass of the c quark has to be very small (possibly unrealistic) to be able the match even the smallest of the experimental values. If one were to extrapolate up to the $\sqrt{s} = 60$ Gev range the disagreement between these predictions and the experimental value is large[22].

The Ellis, Quigg, and Sexton calculations make explicit predictions for the inclusive properties of hadronically produced charmed particles. It is interesting to note that the predicted $\frac{d\sigma}{dx_F}(\bar{x}_F)$ distribution shown in Figure I.3 for gg-fusion and $q\bar{q}$-annihilation can be adequately described by the simple form

$$\frac{d\sigma}{dx_F}(\bar{x}_F) \propto (1 - |x_F|)^N \tag{I.5}$$

with $N \approx 8$.

The general features of charm hadroproduction discussed above can be summarized as follows:

1. The ratio of charm to non-charm events in hadroproduction is a few orders of magnitude lower than the e^+e^- process but the absolute cross-section is much larger.

2. Charm hadroproduction rates should be calculable using lowest-order QCD perturbation theory. Information about the nature (and form) of the sea-parton momentum distribution function might be revealed in the context of QCD.

3. Within perturbative QCD theory, closed-charmed states can successfully be interpreted as the result of central production dominated by flavor-creation interactions (primarily gg-fusion); however, the observed production rate in open-charmed states is too large to be explained by fusion processes alone.

4. Two center-of-mass energy regions reveal dramatically different production characteristics. Near $\sqrt{s} \simeq 25$ GeV, observations indicate that charm is predominately produced in the central region (i.e., low x_F) with estimates of the total charm cross-section in the range of 10 μbarns to 80 μbarns. Near $\sqrt{s} \simeq 60$ GeV, some observations indicate that charm is predominately produced in the forward region (diffractively, high x_F) with total charm cross-sections at about 1 millibarn.

5. The tremendous rise in the charm cross-section as the center of mass energy jumps from 25 GeV to 60 GeV has not yet been satisfactorily resolved by either central or diffractive production models.

This thesis will concentrate on measuring the cross-section for the hadronic production of $D^* \to (K \pi) \pi$ at $\sqrt{s} \approx 35$ Gev and compare it with the results of another experiment.
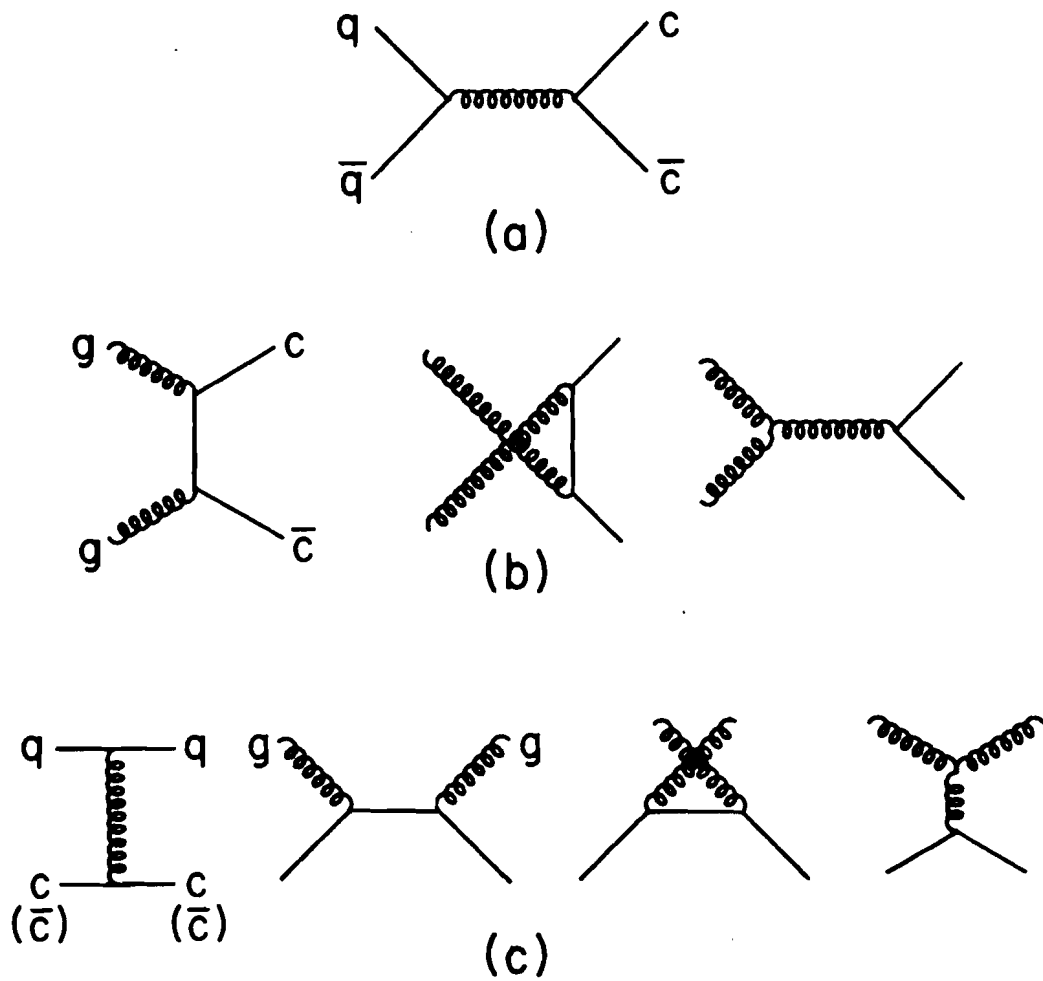
Figure I.1:   Lowest-ordered QCD diagrams:

(a) and (b) flavor-creation diagrams,

(c) flavor-excitation diagrams.

Charm Quark Production, Ellis & Quigg
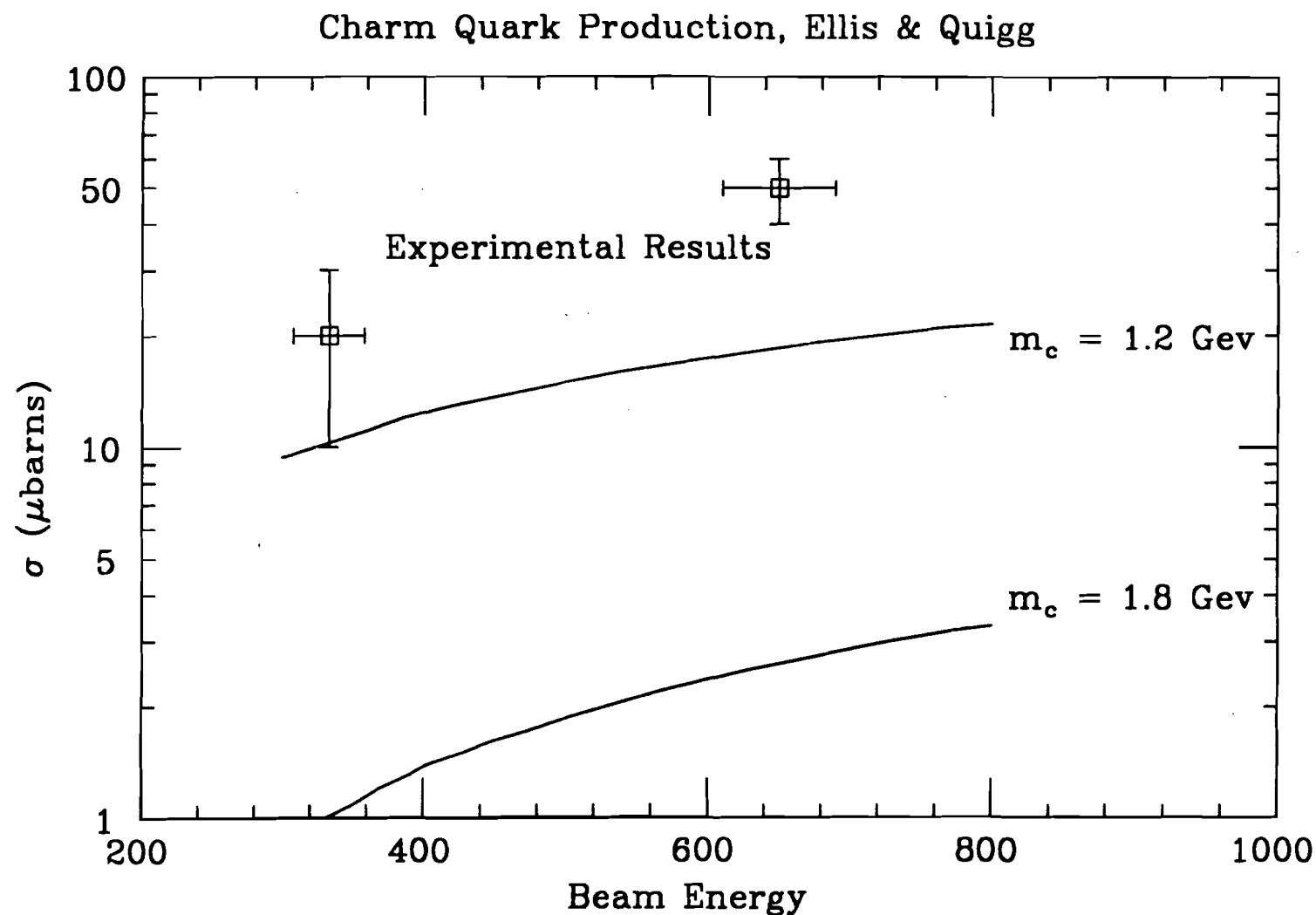
Figure I.2: Total cross-section (σ) for heavy-flavor production.
QCD calculations by Ellis and Quigg are shown by solid lines.
Representative experimental results are shown in by the plotted boxes.
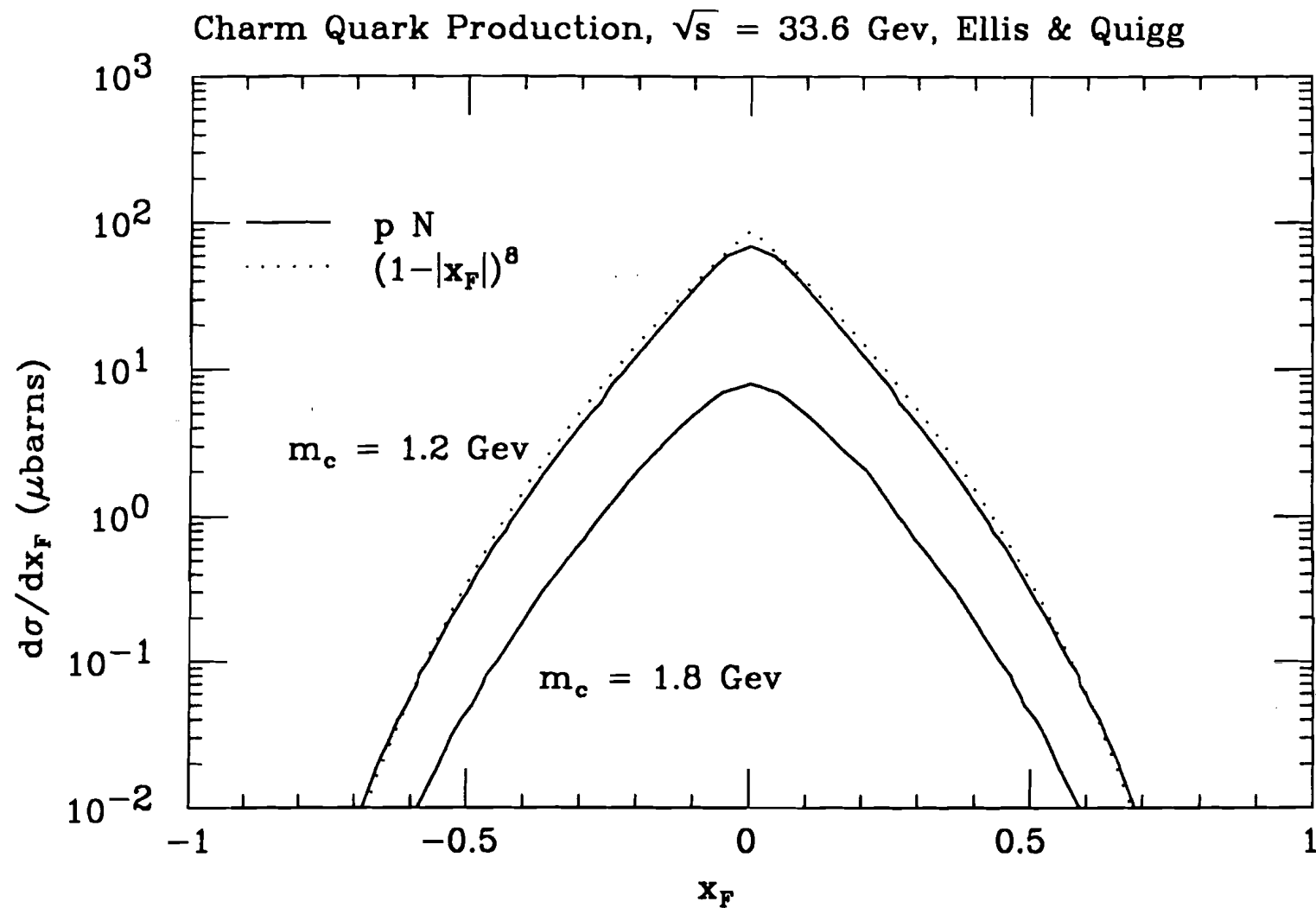
Figure I.3: Differential cross-section ($\frac{d\sigma}{dx_F}(\bar{x}_F)$) for heavy-flavor production.
QCD calculations by Ellis and Quigg are shown by solid lines.
$(1 - |x_F|)^8$ is shown by the dotted line.

Chapter II: Experimental Apparatus

Description of Physical Characteristics and Function

Experiment 400 was conducted at Fermilab in the Proton East beam line from October 1983 to June 1984. The experiment used a wide-band neutron beam with a mean energy of $\approx$ 640 Gev directed at 0° onto a multi-element target. The experiment used a multiparticle spectrometer of fairly standard design with angular acceptance of approximately $\pm$ 100 milliradians. The data aquisition system was capable of collecting 5000 events per accelerator spill which enabled us to take $\approx$ 60 $\times 10^6$ triggers from January to June 1984.

II.A. Beam and Production Target

In Experiment 400, 800 Gev protons from the accelerator were directed on a beryllium target located 120 meters upstream of the experimental area (see Figure II.1). The resulting secondary beam had a variety of particles with the hadronic component dominated by neutrons having the spectrum shown in Figure III.4. Charged particles were removed with sweeping magnets which directed them into a tungsten dump. The flipper magnet could insert varying amounts of lead into the beam to remove photons (we used 12 radiation lengths). These lead "flippers" were housed inside a magnet to quench the build-up of electromagnetic showers. Photons emerging from the flipper magnet typically had energies of less than 1 Mev and while the hadronic content of the beam was reduced by only 50%. Very kew K_L^0's generated at the production target could intersect the spectrometer as can be seen in Figure II.1 and were further reduced by the fixed collimators and the minimum transverse energy requirement of 300 Gev (see II.D.1.c below). Variable steel collimators produced a 0.6 cm $\times$ 0.6 cm beam of the remaining particles, now predominately neutrons, on the Experimental Target.

II.B. The Spectrometer

The E400 spectrometer was a standard fixed-target multiparticle spectrometer. The spectrometer included wire chambers for tracking, magnets for momentum measurement, Čerenkov detectors for particle identification, calorimeters for energy measurement, and muon identification. E400 employed a multi-element target and a high-resolution wire chamber to achieve the resolution required to do charm physics. Figure II.2 shows the positions and sizes of the various components. Table II.1 gives specifica-

tions for the target, trigger, and tracking components. Table II.2 gives specifications for the components devoted to particle identification and Table II.3 describes the calorimetry.

II.B.1. Experimental Target

In the hopes of being able to look at the A dependence of the charm cross-section, the Experimental Target was made of three different materials (see Figure II.3). These materials were tungsten, silicon, and beryllium. The materials were ordered with the high Z materials farthest upstream to minimize multiple scattering. The silicon area (Si) was made of 10 wafers, 200 μm thick separated by $\approx$ 200 μm each. The ionization of charged particles traversing the wafers was measured by separate ADC's which were recorded in the data stream. We hoped to use this ionization information to follow the multiplicity development as interaction products traversed the Si target. This information could potentially be used to pin down the position of the primary interaction to high precision as well as to help locate the position of secondary vertices resulting from the short but finite lifetime of charm decays. However, the breakup of a nucleus at 600 Gev is so messy that the capabilities of the active target was greatly exceeded. Downstream of these three elements were three more wafers of silicon. One of these, designated Si33, was used to determine that an event had occurred in the target fiducial region and to check that the event had a minimum multiplicity. The Si33 response was required in the Event Trigger (see II.D.1.c).

II.B.2. Trigger Counters

Two counters were used to determine that an event had occurred at the target and that products from the interaction had traversed the spectrometer.

II.B.2.a. T1

An 8×8 cm^2 piece of scintillator was placed directly in front of the magnetic shield plate of M1 as shown in Figures II.2 and II.5. An interaction in T1 was an indication that particles were coming from the target area. The use of T1 in the trigger is described in section II.D.1.a.

II.B.2.b. H×V

The H×V counters (Figure II.4) were located behind the last PWC and the last Čerenkov counter. Coincidences in the crossed H and V counters were used (sections II.C.2.a and II.D.1.a) to determine that more than one charged particle had traversed the entire spectrometer.

II.B.3. MWPC's

II.B.3.a. Main Chambers and TRM's

The experiment had 5 MWPC chambers (P0 - P4) in what was called the main spectrometer. Each chamber had 3 views, X, U, and V, for a total of 15. The X plane had vertical wires while the U and V planes had wires inclined from the horizontal at an angle of $\pm\tan^{-1}(.2)$. Three chambers, P0, P1, and P2, were between M1 and M2 and two chambers, P3 and P4 were downstream of M2. The wire spacing in all but one view was 2 mm. The X view of P4 had a 3 mm wire spacing. Each wire was read out to a latch. All the chambers but P0 had Time Recorder Modules (TRM's). The TRM's were Time to Digital Convertors (TDC's) that recorded the arrival times of the signals within groups of wires. The TRM band widths varied from 8 wires in the center where particle multiplicities were high, to 32 wires at the edges where particle multiplicities were low. This "poor man's" drift chamber gave TDC information from which the position a track could be determined to a resolution better than just the wire spacing. These TRM bands were also used in the trigger to a get crude multiplicity measurement and were used by the M7 for quick real-time momentum determination.

II.B.3.b. Vertex Chamber

Upstream of M1 and immediately downstream of the experimental target was another wire chamber, the Vertex Chamber (also known as the D5)[23]. The Vertex Chamber provided the position resolution necessary for the lifetime algorithm (see Appendix C). Nine planes of wires were wound with a pitch of 250 microns covering roughly a 2×2 in^2 region. Each wire was read out to a latch. Figure II.5 shows the position of the planes relative to the target and T1. Figure II.6 shows the distribution of the reconstructed vertices from the data. The RMS width at the tungsten target, the thinnest, is 1200 microns which small compared to our vertex resolution.

II.B.4. Magnets

Two analysis magnets provided momentum analysis in the experiment. The downstream one, M2, had a kick of .584 Gev. The change in the trajectory of a particle as that particle passed through M2 (which were called tracks) provided the information used to determine the momentum. The upstream magnet, M1, was used in determining the momentum of wide-angle or low-momentum particles that did not pass through M2 (which were called stubs). M1 had a kick of .401 Gev that was oriented in the opposite direction of M2. The spectrometer had no magnetic dispersion at a plane near the plane of the Lead Glass array. At the dispersionless plane, the intersection of a track with the dispersionless plane is independent of the track's momentum. Having the dispersionless plane near the end of the spectrometer increased the geometric acceptance of particles produced at the experimental target. Mylar bags of helium were placed inside the aperture of both magnets to reduce multiple scattering of particles in the spectrometer. Multiple scattering inside a magnet seriously degrades momentum resolution. The helium bags provided a 10% reduction in the total material in the spectrometer from Si33 through CB.

II.B.5. Čerenkov

Three Čerenkov counters provided particle identification. They were labeled CO (Orange), CY (Yellow), and CB (Blue, named after their color). CY and CB provided the minimum amount of information needed to identify pions, kaons, and protons. Figure II.8 shows the physical characteristics of CY and Figure III.10 shows the image of its light collection cells. CB was identical to CY but was only a third as long. CO provided particle identification for low momentum particles that did not pass through M2. Figure II.7. gives its physical characteristics and Figure II.9 shows its cell pattern. Table III.1 gives the threshold momenta and the regions of identification for the three counters. Behind CB was a scintillator hodoscope named CH2 with a segmentation that matched that of CB and CY. The CH2 hodoscope, combined with the Čerenkov response of CB and CY, provided the information used in forming a fast heavy-particle trigger (see section II.D.3).

II.B.6. Calorimetry

The calorimeters in the experiment measured the energy of interacting particles. The previous components of the spectrometer described above only measure charged particles whereas even neutral particles are included here. The neutron beam used in this experiment was a wide-band beam ranging in energy from 0 Gev to 800 Gev (see Fig III.4). Information from calorimetry was used in the experimental trigger to trigger only on that portion of the neutron spectrum above 300 Gev. The energy of the incident neutron can be reconstructed by summing the energy of all the particles in the event (excluding those that are outside the angular acceptance of the spectrometer which must be estimated, see section III.D). The electromagnetic calorimetry was intended to provide π^0 reconstruction. A 2×4 inch hole in the center of the Lead Glass Array and a 2 inch diameter hole in the center of the Hadron Calorimeter allowed non-interacting neutrons to pass through without striking these detectors. The response from these two calorimeters was summed to form the energy trigger (section II.D.1.c). The energy trigger thus required an energy deposition of minimum energy outside the extremely forward cone defined by the holes.

II.B.6.a. Lead Glass (Electromagnetic) Calorimeter

A .6 interaction length, 19 radiation length Lead Glass array (LG) was used to measure the energy of particles that interact with matter predominately via the electromagnetic interaction. This 144 element array (see Figure II.11.) had a high degree of segmentation in hopes of being able to reconstruct neutrals such as π^0's. However, having the dispersionless plane near the Lead Glass meant that the majority of charged particles struck the Lead Glass, interacted in the .6 interaction length of the array, and created large area hadronic showers. The resulting confusion in a typical high-multiplicity E400 event rendered the Lead Glass useless except as a contribution to the total event energy.

II.B.6.b. Hadron Calorimeter

To compliment the Lead Glass array, a 6.4 interaction length Hadron Calorimeter (HC, Figure II.12) was placed behind the Lead Glass Array. The Hadron Calorimeter was made of twenty-four 1.75" thick steel plates sandwiched between .25" thick scintillators. The scintillator detected the ionization from the hadronic debris produced

in the steel. The Hadron Calorimeter was segmented transversely to obtain position information for the showers.

II.B.6.c. Beam Dump Calorimeter

The Beam Dump Calorimeter (BDC, Figure II.13.) measured the energy which passed through the central hole in the previous two calorimeters. The data trigger was predicated on the assumption that a charm event was a hard enough process that it would produce a significant amount of energy transverse to the direction of the beam which would thus miss the central hole. To reconstruct as much of the total energy in the event as possible, the Beam Dump Calorimeter with 5 interaction lengths of tungsten was installed to measure the forward energy and flag the possible diffractive dissociation of the beam neutron. Information from the Beam Dump Calorimeter was not used in the trigger.

II.B.6.d. Outer Electrophotometer Counter

The Outer Electrophotometer (OE) counter (Figure II.14.) was another electromagnetic calorimeter which was constructed as a lead-scintillator sandwich instead of an array lead glass blocks. The OE measured wide-angle electrons and photons.

II.B.7. Muons

Muons were detected in the most downstream portion of the spectrometer. Large slabs of steel and concrete were used as a filter to absorb hadrons. The highly penetrating muons readily passed through this filter and could be detected in muon counters. Position information from the 4 muon detection systems was matched with tracks from the main spectrometer to identify specific spectrometer tracks as potential muons. The relative positions of the four components of the muon system are shown in Figure II.15.

II.B.7.a. μH and μV

The μH and μV counters were banks of horizontally and vertically oriented scintillation counters which detected muons emerging from the filter and provided course position information.

II.B.7.b. P-tubes

The P-tubes were two banks of proportional tubes that were used to give higher position resolution than the μH and μV. The P-tubes were oriented horizontally and so provided position information only in the y direction.

II.B.7.c. Outer Muon counters

A bank of scintillation counters ($O\mu$) that were to identify muon stubs were located on the downstream side of M2, opposite the OE counters. The steel of the magnet served as the filter for the low momentum stubs. The large area of the scintillator panels, $\approx$ 3' by 6', caused timing problems and so the information from the $O\mu$ was never used.

II.C. Electronics

This section gives a description of the function of each of the components. First, a brief overview of the data aquisition system is described. Section II.D describes in more detail how, together, they were used in the trigger to collect the data used in this thesis. Figure II.16. shows a schematic layout of the data aquisition system.

During an accelerator spill, signals from the individual parts of the spectrometer went to the Counter Electronics, which converted them to standard signals, such as NIM or digitized values. The Trigger Electronics determined whether an event was to be kept. The H×V , Master Gate, and Confusion Logic checked that an interaction occurred in the target fiducial region and that products from the interaction traversed the spectrometer and sent out the Trigger, the first level of the final trigger decision. The DC Logic was the second level of the trigger decision and included the Coincidence Registers (CR's), the Trigger Generator (Input, TGI, and Output, TGO), the Buslines, and the Pin Logic. Upon receipt of the Trigger, the TGI initiated an internal Strobe that passed through each of the components of the DC Logic. The various components in the DC Logic compared the information from some of the Counter Electronics with certain trigger requirements. If the requirements were not met, a Pin Logic blocked the passage of the Strobe. The information from the Counter Electronics was stored in the CR's and the Data Buffer while the second level trigger was being decided. If the Strobe passed all the way through the DC Logic, the TGO sent out the Event Trigger which initiated ADC's and started the storage of the event in the Fastbus memories by way of the Illinois Black Bins. The Event Trigger also initiated the M7 trigger processor which

made the third and final level decision for acceptance of an event. When the 20 second spill was over, the computer read the events from the Fastbus memories and wrote them to tape during the interspill time of 40 - 60 seconds.

II.C.1. Counter Electronics

II.C.1.a. ADC's

The signals from the Čerenkov counters (CO, CY, CB), the four calorimeters (HC, LG, OE, BDC), and the silicon target (SI) were sent to ADC's. Digitization started when they received the Event Trigger. The digitized values were read by the Illinois Black Bins.

II.C.1.b. PAD's

Signals from the Hadron Calorimeter and the Lead Glass Array were summed and sent to the Pulse Area Digitizers (PAD's). The PAD's provided a crude (4 bits) measurement of the energy in the event that was outside the central hole. This information was produced fast enough to be used in forming some of the Buslines to form the Event Trigger.

II.C.1.c. Discriminators

The signals from most phototube detectors (T1, H, V, $O\mu$, μH, μV, Si, CH2, CO, CB, CY) went to discriminators. The threshold of each was set so that the discriminator would generate an output if a single particle interacted in the counter. The output pulses were sent to the Coincidence Registers (CR's). The raw signals were delayed so they would reach the CR's in time for the Gate from the TGI.

II.C.1.d. MWPC Registers and Encoders

The MWPC registers recorded the wire hits in latches. The latches were set when the Gate from the Confusion Logic was received. They were then quickly cleared by a delayed signal from the Confusion Logic unless this clear was blocked by the TGI. The encoders read which wires were hit and sent their addresses to the Black Bins. Encoding started once the Event Trigger was received.

II.C.2. Trigger Electronics

II.C.2.a. H×V

The discriminated output of the H and V counters also went to the H×V module. The signals from the individual counters were separated corresponding to four quadrants in the physical array. If the hits were consistent with at least one particle in each of two quadrants or two particles in one quadrant, an output signal was sent to the Master Gate module.

II.C.2.b. Master Gate

The Master Gate generated the signal that indicated that an interaction had taken place. Its inputs were the discriminated pulse from T1, designated "T", and the output from the H×V module, designated "A". The Master Gate generated two outputs. One was A and the other was the and of A and T (A · T). The two signals enabled studying the Master Gate efficiency. These signals were passed to the Confusion Logic module.

II.C.2.c. Confusion Logic

The Confusion Logic started the chain that formed the Event Trigger. It received the A and the A·T signals and generated the Gates for the CR's and the wire chamber electronics. Its output went to the Trigger Generator in the DC Logic rack. The output of the Confusion Logic was called the Trigger or Master Gate signal.

II.C.2.d. DC Logic

In order to minimize the need for precise timing of the signals from each counter, many of the trigger decisions were made on the basis of DC levels formed from counter signals that were stored in latches. These levels were them held and were available for use by the various components of the DC Logic until they were cleared.

II.C.2.d.i. Coincidence Registers (CR's)

The Coincidence Registers were D-type flip-flops, or latches, that were clocked in by the Gate from the TGI. Once a signal came, in time with the Gate, then the output, a DC voltage, was available for as long as it took to determine whether or not to send out a trigger. The CR's were cleared a short time before the Master Gate reached them.

II.C.2.d.ii. Trigger Generator

The trigger generator was the entry and exit point of the DC logic chain.

II.C.2.d.ii.(a). Input Module (TGI)

The input module received the Trigger from the Confusion Logic. The TGI also had busy circuitry to prevent starting new triggers while a previous one was being decided. The TGI sent the Clear and Gate signals to the CR's and sent the Strobe to the Pin Logic.

II.C.2.d.ii.(b). Output Module (TGO)

The output module sent out the Event Trigger. If the Strobe passed all the way from the TGI to the TGO, the TGO passed it on to the the Data Buffer and sent out the Event Trigger.

II.C.2.d.iii. PAD, Sum, PWC Logic

These were logic modules that provided the information to form the Buslines. The PAD Logic used information from the PAD's to determine if a minimum amount of energy had been deposited in the calorimetry. The PWC Logic provided multiplicity information. The Sum Logic provided logical combinations of the CR's.(see II.D.1.c.)

II.C.2.d.iv. Buslines

The results of the above three logic modules went to the Busline driver. Each of the 16 Buslines had different requirements for it to be set. Once the Buslines had been decided, all of the Pin Logic modules could look at the Buslines simultaneously.

II.C.2.d.v. Pin Logic

Each Pin Logic module could be set to require various Buslines to be satisfied. Each had the choice of on, off, or don't care for each Busline. When the Strobe came from the TGI, a Pin Logic module passed it on if the module's requirements had been met. If desired, the Strobe could be required to pass a prescaler after leaving the Pin Logic. Since some pin requirements were naturally met more frequently than others, the prescalers allowed flexible adjustment of the ratio of these requirements.

II.C.2.d.vi. Trigger Store

The Trigger Store recorded which Buslines and which Pins had been set. It sent that information to the Data Buffer to become part of the data record. The Trigger Store also passed the Strobe from the Pin Logic to the TGO.

II.C.2.e. M7

The M7 was a programmable trigger processor that was built at Fermilab [24,25]. After the Event Trigger had been sent out, the M7 made the final decision (based on the heavy-particle content of the event) to store the event in the Fastbus memories.

II.C.3. Data Buffering

The accelerator at Fermilab originally had a spill time on the order of 1 second with anywhere from 20 to 60 seconds between spills. E400 and its predecessors used various forms of data buffering to store events selected by simple but fast triggers and so were not limited by the long time it took to write an event on tape. Large numbers of events could be stored during each spill and then read between spills, in essence providing a more continuous beam and greatly increasing the accepted luminosity. As spill times were increased and the duty cycle of the accelerator increased, the buffer sizes were increased to maintain the same effective data rate.

II.C.3.a. Data Buffer

Upon receipt of the Strobe, the Data Buffer stored the contents of the CR's until the Black Bins were done transferring the information to the Fastbus Memories. The CR's and the DC Logic chain were free to monitor interaction rates for the computation of deadtime.

II.C.3.b. Illinois Black Bins-Multiport/UMP

In earlier versions of E400, the Black Bins provided the path for the data to be entered in the computer and for instructions to be sent out from the computer. The Black Bins were similar to CAMAC in function but were physically smaller and were simpler and faster. In E400, they were addressed by the Trace for the transfer of the data from the Data Buffer and various encoders to the Fastbus memories. The Multiport was a port multiplexer to allow the computer to to address each of the Black Bins. The UMP was the interface between the computer and the Multiport. In E400 the

Black Bins were addressed by the Trace for data transfer, by the Multiport for passage of instruction lists from the computer, or by another computer, such as an LSI-11 for diagnostic purposes.

II.C.3.c. Trace-memory-UPI[26]

In the earliest version of E400, the readout of the event went through the ACE (Automatic Control Entry) system which used the Black Bins and Multiport/UMP for data transfer to the computer. Later the RACE (Revised ACE) system used Fastbus components to transfer the data from the Black Bins to Fastbus memories leaving the Multiport/UMP for transferring instructions. Finally with the inauguration of the Tevatron, the TRACE (Tevatron Revised ACE) was incorporated featuring larger Fastbus memory capacity to handle the longer duty cycle of the Tevatron. The original Fastbus memories were 1/4 Mbyte each and there were four of them each with a separate RACE controller so that the readout into the memory could be done in parallel. The new memories were 2 Mbytes each and had new TRACE controllers. Assuming that the amount of data in each of the four Black Bins was well matched, the readout could be completed in a quarter of the time as a serial readout since each Trace controller could handle the transfer individually. The UPI was the interface between the computer and the Trace system.

II.C.3.d. CAMAC

The experiment also included a CAMAC branch highway (not shown in Figure II.16.). The CAMAC system enabled the computer to read the scalers, communicate with the M7, and communicate with the silicon target ADC's for calibration. The analysis program that the M7 used for its trigger decision was loaded through CAMAC once per run.

II.C.3.e. Scalers

A number of signals were sent to scalers (not shown in Figure II.16.). These counted over the time to write a whole data tape. The signals included Master Gate signals, number of events sent to the Fastbus memory, and the number of protons incident on our target and were used to monitor the luminosity. The scalers were read by the CAMAC system at the end of each run and their data were stored on the magnetic tape containing that run.

II.C.4. Data Storage

During the spill from the accelerator, the trigger decisions were made by the Master Gate, the DC Logic, and the M7. The data was transferred to the Fastbus memories for fast storage. Then between spills, control was given to the computer which read the events from the Fastbus memories and transferred them to magnetic tape.

II.C.4.a. Computers

The experiment used a PDP-11/45 for the data acquisition which also allowed (in theory) online monitoring of each event. Since the data acquisition code almost completely filled the 11/45's memory and the writing to tape took most of the available time, a second computer, a PDP-11/34, was linked through a DR-11W to transfer events to the second computer. The 11/34 then processed diagnostic and monitoring programs for the spectrometer.

II.C.4.b. Bison Box

The Bison Box was an interrupt device built by Fermilab. The Bison Box provided interrupts to the trigger logic and to the computer at the beginning of the spill and end of spill. The computer could then initialize the data aquisition system for the spill and start reading the Fastbus memories at the end of the spill.

II.D. Trigger and Data Aquisition

Modern day High Energy Physics is an attempt the optimize the need to quickly select likely candidates of rare processes with the desire to not bias the selected data based on the incomplete knowledge of the processes involved. E400 tried to get the best of both by using a loose three stage trigger and designing the data aquisition system to be able to take data at high rates. More restrictive decisions about the nature of the events were done in the off-line analysis. Due to these high rates and long interspill times, a memory buffer was used to store the information during the spill. Then between the spills, the data could be transferred to magnetic tape. Approximately 1500 magnetic tapes (2400', 6250 bpi) containing nearly 60 million triggers were written of which approximately 500 tapes were written under consistent, stable running conditions and are analysed in this thesis.

When a spill started, the computer received a signal from the accelerator through the Bison interrupt box. The computer loaded instruction lists to the Race system, the Black Bins, and the M7, and then released control until the spill was over or the memories were full. When the accelerator signaled that the event was over or when the memories were full, the computer transferred the data from the buffer memories, through the Trace/UPI, to magnetic tape and recorded the scaler information. There was also the provision for online monitoring of the events to check on the status and well being of the experiment.

As individual events occurred, the Master Gate looked at two of the detectors, T1 and H×V , to determine if at least two particles have traveled from the target area through the rest of the spectrometer. Then the DC Logic made a determination of the quality of the event based on things like multiplicity and energy deposited in the calorimeters. Finally the M7 used crude chamber tracking to make a crude momentum determination and used the particle identification from the Čerenkov counters to preferentially select events with kaons in them. About 52% of all D decays contain a kaon. Events that were passed by the M7 were stored. (Again, see Figure II.16 for a layout of the data aquisition system.)

II.D.1. Trigger

II.D.1.a. Master Gate

The first level of the trigger was the Master Gate. In taking most of our data, the Master Gate was based on the following. We required that a particle pass through the T1 counter and that there be hits in the H×V hodoscope that were consistent with two charged tracks traversing the spectrometer. The signals from the H×V array went into the H×V logic module. The module looked at the four quadrants of the array and generated a trigger pulse if there were hits in at least two quadrants or at least two hits in one quadrant (Figure II.17).

The signal from the T1 counter and the $H \times V_{2-body}$ signal were sent to the Master Gate logic module. In this experiment, the Master Gate gave two output signals. One was the $H \times V_{2-body}$ signal and the other was the "and" of the H×V and the T1 signal. These signals were sent to the Confusion Logic (CL).

II.D.1.b. Confusion Logic (CL)

Up to this point all the electronic components were free-running, limited only by the intrinsic recovery times of the spectrometer components. The Confusion Logic was the first element to introduce deadtime into the data selection.

A schematic of the Confusion Logic is shown in Figure II.18. When signals came to the CL, it counted the number of times that either input was on (> 0). If an internal busy line was not already asserted, the CL asserted the busy line and then waited 100 nsec to let the signals settle. The following conditions could set the busy line and inhibit the trigger:

1) A previous > 0 signal within 100 nsec, which let the electronics and chambers recover,

2) DC Logic deadtime, 250 nsec, which let the trigger decision on a previous event continue or if a previous event had been rejected, let everything be cleared,

3) A external busy which could be:

A) the extra 50 ns needed by the TGO to start the readout (see below) or,

B) a readout was in progress (computer busy) which included:

    i) Spill gate not asserted; no spill in progress

    ii) Trace readout in progress

    iii) Fastbus memory full.

The 100 nsec delay also rejected abnormally high interaction rates if portions of the spill were too intense. After the delay, the CL checked to see if both the A and the A·T inputs were on (> 1) and if true a Trigger was sent out. A Trigger was also sent out for 1 of every 1024 of the > 0 inputs in order to collect an unbiased sample of background events for monitoring deadtime. The Trigger latched the MWPC's and the D5 latches, gated the PAD's, and set off the Trigger Generator Input (TGI). After 200 nsec, a clear was sent to the MWPC's but this clear could be blocked by the DC Logic if it had decided to keep the event. The CL kept count of four quantities, the > 0 and the > 1 for all times (No Deadtime) and the > 0 and the > 1 for when the busy was not set (Deadtime). The > 1 No Deadtime was one of the values used in calculating the livetime of the experiment. As can be seen in Figure II.18 the > 1 No Deadtime signal counted all possible triggers to the experiment.

II.D.1.c. DC Logic

Upon receiving the Trigger from the CL, the TGI sent a clear signal to the Coincidence Registers (CR's) and then sent them a delayed Gate. The inputs to the CR's were the NIM signals from the discriminators that were timed to arrive at approximately the same time as the Gate. Any signal that was present when the Gate arrived was latched in. The latched bits could then be combined to form more detailed general information. There were two types of CR's:

    1) provided the analog sum of four inputs,

    2) provided an analog output for each input.

Some of the data on the CR latches went to Sum Logic modules (Figure II.19) which could look at more than one CR and produce $=0$, >0, > 1, etc. digital outputs. The output of the Sum Logic and the CR's were DC voltages. Combinations of these Sum Logics and individual CR's went to a Busline driver which placed them on a bus in the CR crate.

After waiting for 200 nsec for the CR logic to be determined, the TGI sent a signal called a STROBE to the Busline driver and sent a delayed busy to the Pin Logic. The STROBE blocked further reception of Triggers for 200 nsec.

The combinations of CR's mentioned above, of which there were 16, were called "Buslines". They provided an intermediate level of complexity based on signals latched by the Master Gate. They could be:

1) single bits from the hodoscope latches (the CR's)

2) combinations of bits from the CR's (the Sum Logic)

3) multiplicity conditions from the MWPC's

4) threshold conditions in pulse area from the PAD's

The relevant Buslines used in E400 were:

$B1$: Minimum Multiplicity – The median number of TRM band hits taken from the individual band hit totals in P0, P1, and P2 had to be at least 4. Similarly the minimum number of band hits in P3 and P4 had to be at least 2. When both these conditions were true, the busline was set.

$B2$: Si33 – This Busline required that there be a minimum amount of energy in the Si33 element of the target, which ensured that the Master Gate signal came from an interaction in the target and not from sources such as halo particles which were produced in the upstream components of the beamline.

$B7$: Total Transverse Energy – This required that the PAD from the Hadron Calorimeter and Lead Glass be $\geq$ 4, which corresponded to a minimum transverse energy of $\approx$ 265 Gev which roughly translated to a minimum neutron energy of 300 Gev.

$B16$: Master Gate – Any event that passed the requirements listed in section II.D.1.a. and b. set this Busline. As mentioned below Busline 16 was the only requirement for Pin 2 and constituted the minimum bias trigger for online monitoring of deadtime and offline trigger studies.

Each of several Pin Logic modules (Figure II.20) looked at all the Buslines and would pass the STROBE if the Buslines matched the requirements of the Pin Logic module. The Pin module could require that each Busline be on, off, or it could ignore the state of that Busline. The requirements were set by jumpers on the modules so requirements could be changed.

After the STROBE passed through a Pin, it might also be required to go through a prescaler which would pass 1 of every 2^N STROBES. The prescalers allowed us to enhance the ratio of rare triggers to more common ones on the data tapes. Between 6% and 10% of the data was taken under Pin 2 and the rest was Pin 4.

The two Pin Logics that were used for the trigger were:

- Pin 2 = $\overline{B16}$ with a prescale of 1/128 (approx 15% of the data had a Pin 2 prescale of 1/64)

- Pin 4 = $B1 \cdot B2 \cdot B7 \cdot \overline{B16}$ with no prescale.

The results of the Pins (more than one could be satisfied by a single event) went to the Trigger Store Module which placed the results in the Data Buffer allowing the Bus and Pin Logic to be released sooner to return to monitoring deadtime. The Pin Logic modules also generated a signal for measuring deadtime, the SD output, which did not count while the Computer Busy was asserted.

If a STROBE passed through one or more of the Pin Logics, it continued on to the Trigger Generator Output (TGO). The TGO blocked the clear of the MWPC's and sent a HOLD signal to the TGI for another 50 nsec to let the Computer Busy line be formed. The TGO also strobed the CR's so that the data, along with the Trigger Store and Buslines, could be transferred into the second buffer, the Data Buffer. Finally, the TGO sent out the Event Trigger to the rest of the experiment to start ADC digitization, MWPC encoding, transfer of data to the FASTBUS memories, and set the Computer Busy line.

The deadtime was monitored by counting scalers which were read out at the end of each spill. As mentioned the Pin 2 SD scaler counted only "live" master gates. The Computer Busy signal, which blocked counts from entering the Pin 2 SD scaler, was generated by any source of deadtime: the M7 decision time (to be described below), the

TRACE busy time (read-out time), the memory full time, the off-spill time, the ADC digitization recover time, and the clear time after an aborted event. There were 4 Illinois Black Bins which were read out in parallel to 4 Trace memories. The largest readout deadtime of about 300 μsec per event was set by the largest block of data in any of the four readout paths which included 256 ADC's plus a few flag words. Digitization gave an additional deadtime of 100 μsec. These deadtimes were identical for all events (Pin 2 or Pin 4). Additional deadtime from the M7 was minimized by overlapping the M7 "thinking" time with the readout. Occasionally the M7 was slower than the readout as Pin 4 events (with higher multiplicities than Pin 2) slowed down the trigger processor more than Pin 2 events. The livetime was the ratio of the number of counts satisfying the master gate when "live" (Pin 2 SD) to the total number of counts satisfying the master gate (MG > 1, No Dead Time). This livetime is used with the measurement of the total number of inelastic events in the target to get the number of events that the experiment actually was sensitive to.

II.D.3. The M7[24,25]

While digitizing was going on, the final decision was made by the M7 on whether to keep the event. Since CY, CB, and CH2 had the same segmentation (see II.B.5), the M7 could look for combinations where CY was off, CB was on, and CH2 fired as an indication of the presence of a final-state heavy particle. To suppress triggers from sub-threshold pions, the M7 then used the TRM information to search for a track with momentum greater than 22 Gev coming from the target area:

$$M7_{trigger} = \overline{CY} \cdot CH2 \cdot CB \cdot (P > 22 \text{ Gev})$$

II.D.4. Trace Readout

While the M7 was working, the same Event Trigger that initiated the M7, initiated the Trace controllers to transfer data from the Black Bins to the Trace memories. When the transfer was complete, the TRACE sent a release to the M7 which then cleared the Computer Busy line. If the M7 rejected an event, the pointers to the next event were not advanced and the event was overwritten by the next event. A rejection also cleared the MWPC's and cleared the Computer Busy line.

II.D.5. Data Storage

The time between RF buckets in the accelerator spill was approximately 18 nsec. Since E400 only received between 1 and 10% of the total accelerator spill, the interaction frequency in the experiment was much less. The time required to read an event into the computer and onto tape was on the order of 10 msec. The desire to take events at a higher rate necessitated the storage of the data in the Fastbus memories during the spill.

When the spill was over, an end of spill signal (EOS) was generated which dropped the spill gate. The EOS or a memory full signal raised the Computer Busy line, which stopped all event processing, and told the computer that it could start transferring the data from the Fastbus memory to tape. During the transfer, the computer also read the CAMAC crates and stored information from the blind scalers which had been counting things on a per spill basis.

Some of the events being written to tape were also transferred from the PDP-11/45 to the PDP-11/34 for on-line monitoring of the experiment.

(a) BEAM LINE PLAN VIEW

Fixed Collimators   Variable Collimators   Spectrometer

Target Box   Flipper Magnet

-100   -50   0

Z (METERS)
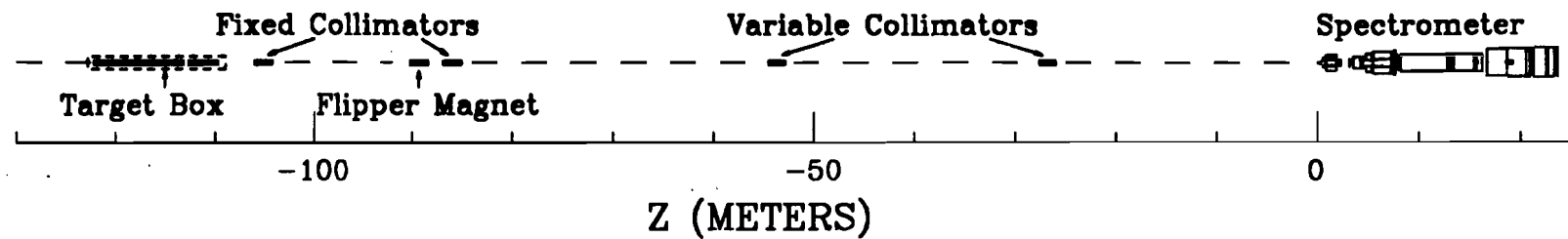
TARGET BOX
(b) EAST ELEVATION

Lambertson Magnets

#1   #2   #3   Magnetized Steel Dump

Protons   Neutral Beam

Be   Tungsten Beam Dump

-125   -120   -115   -110   -10!

Z (METERS)
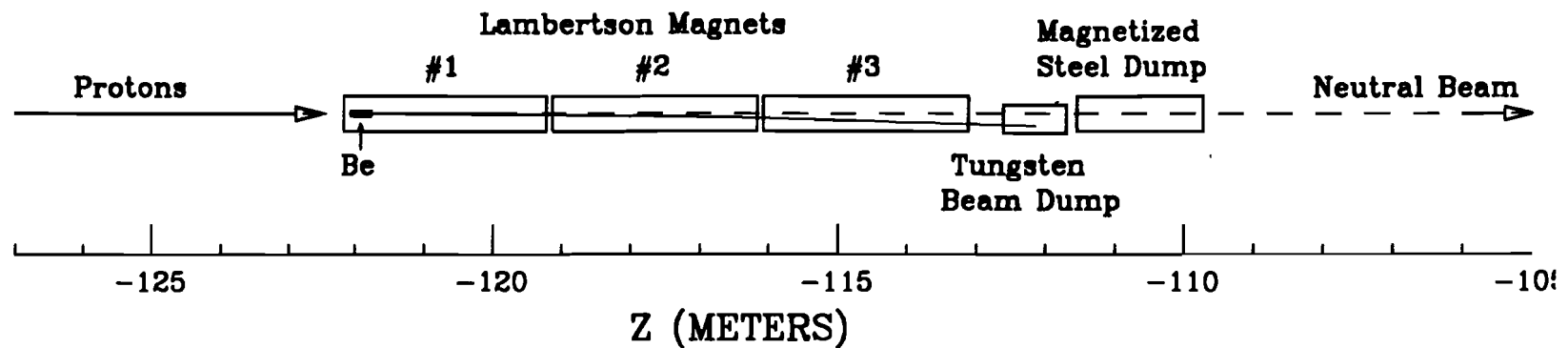
Figure II.1:   E400 Beamline

Figure II.2:   E400 Spectrometer
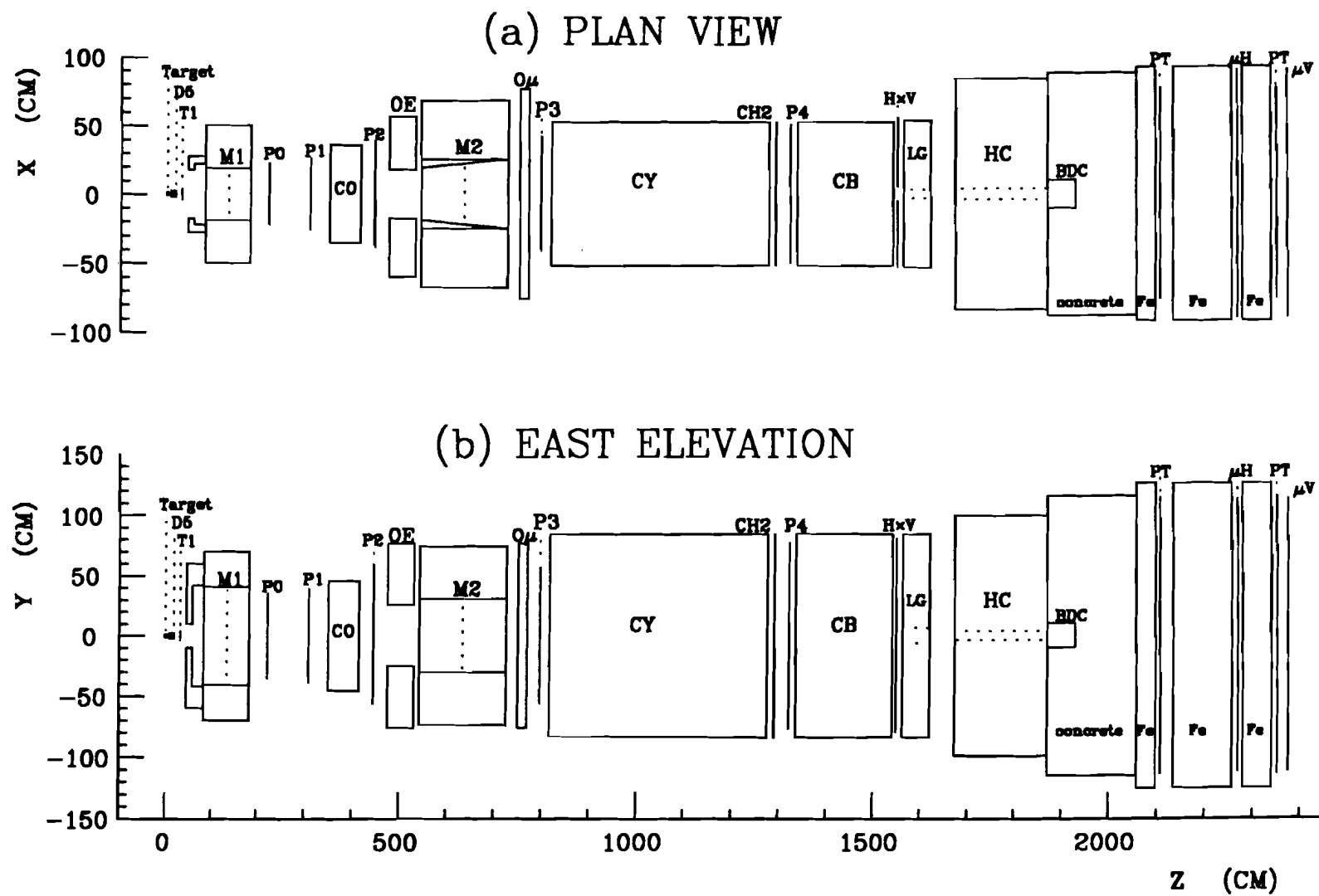
TARGET REGION
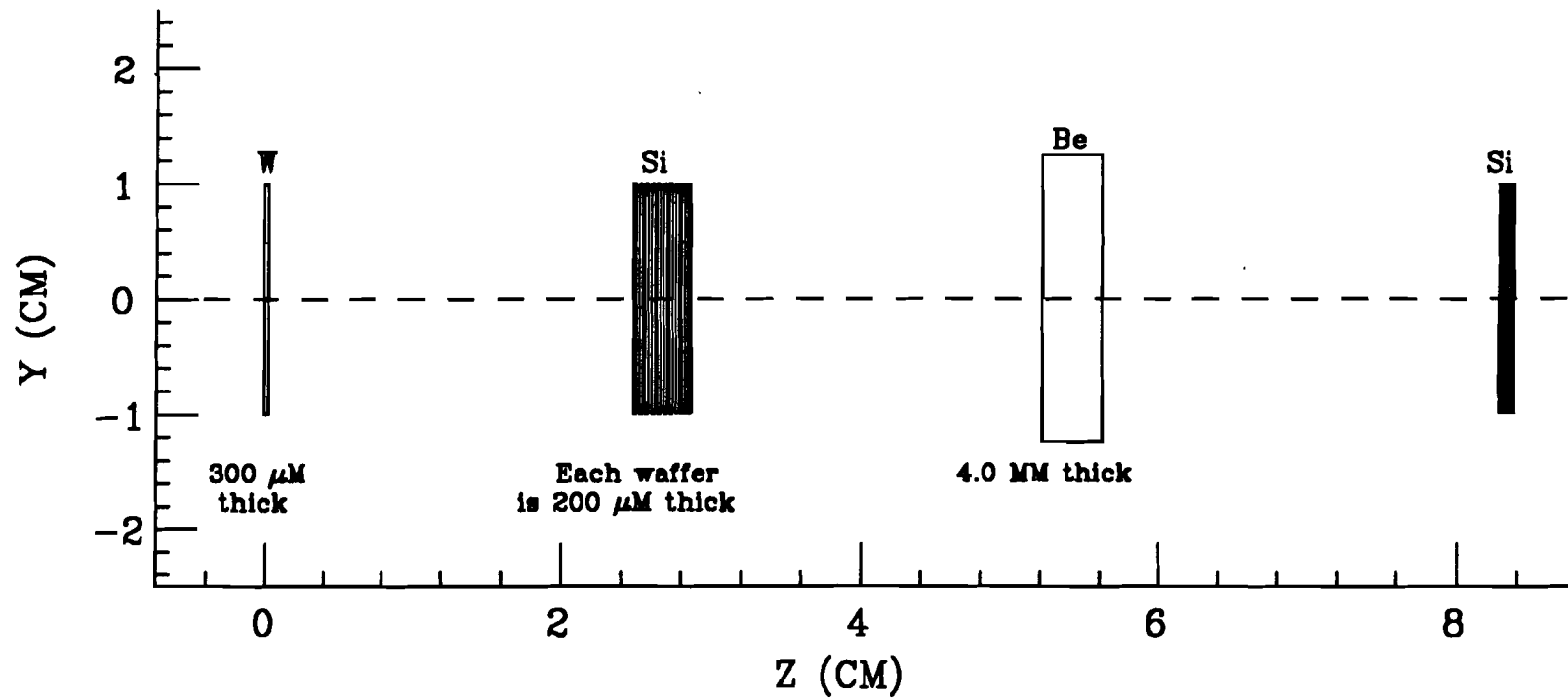
Figure II.3:   Target Layout
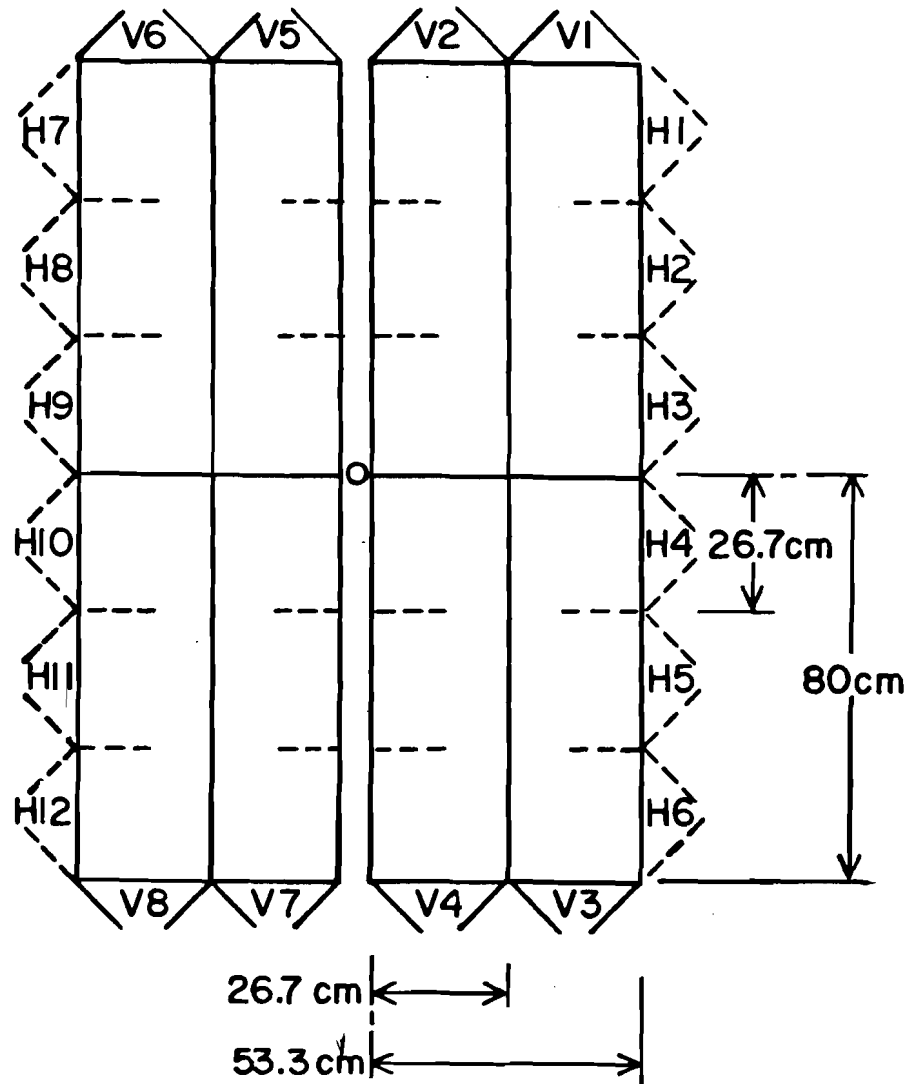
Figure II.4:   H×V Array

Vertex Chamber (D5)
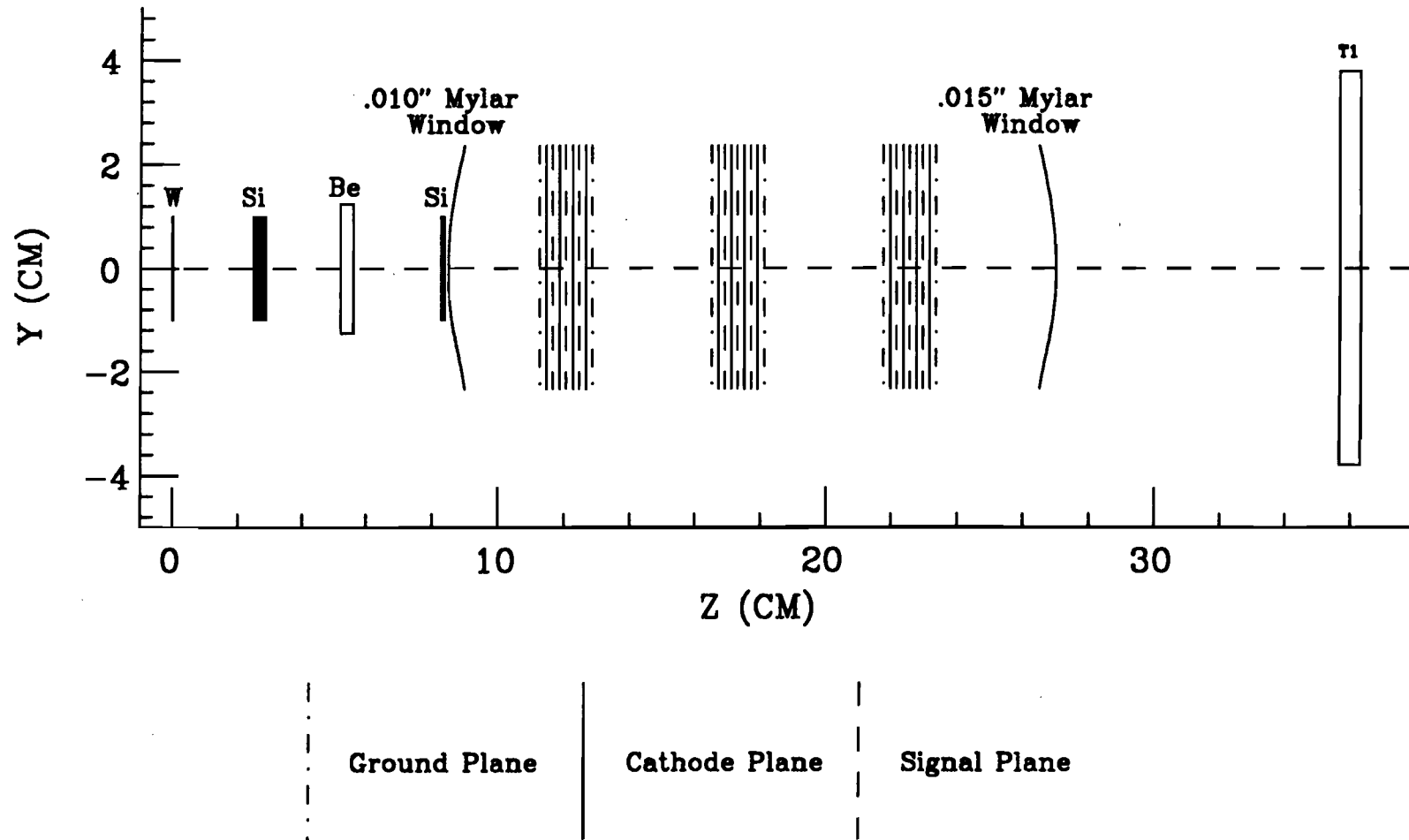
Figure II.5:   Vertex Chamber Area shown in relation to the target and trigger counter T1.
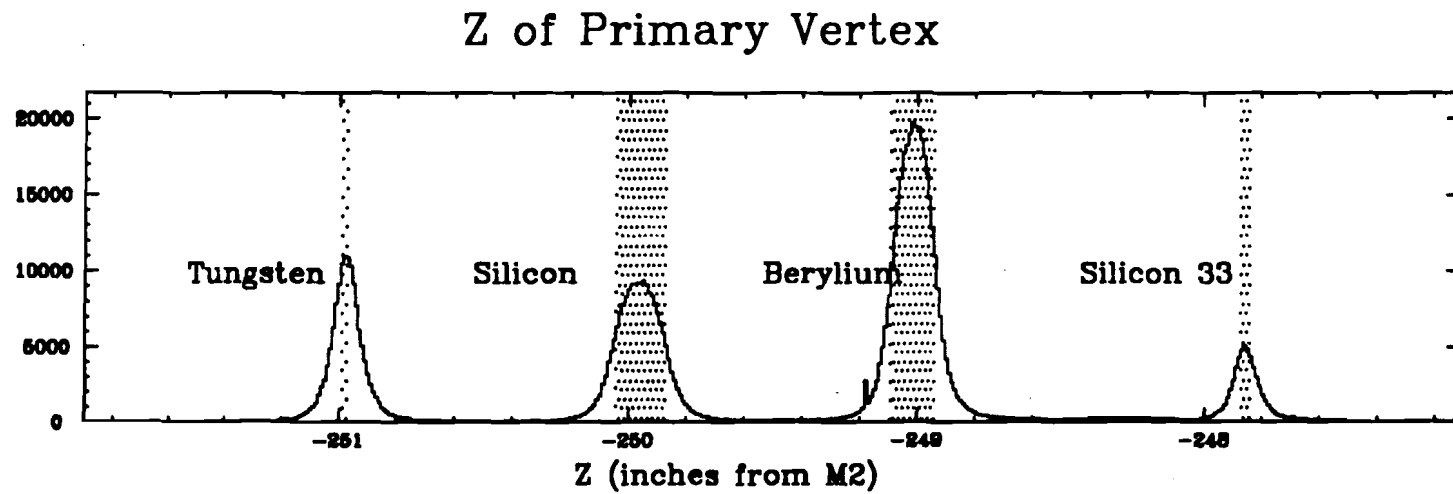
Z of Primary Vertex

Figure II.6: Primary Vertex Distribution

The dotted areas show the actual physical positions of the target elements.

The histograms show the vertices reconstructed from the data.
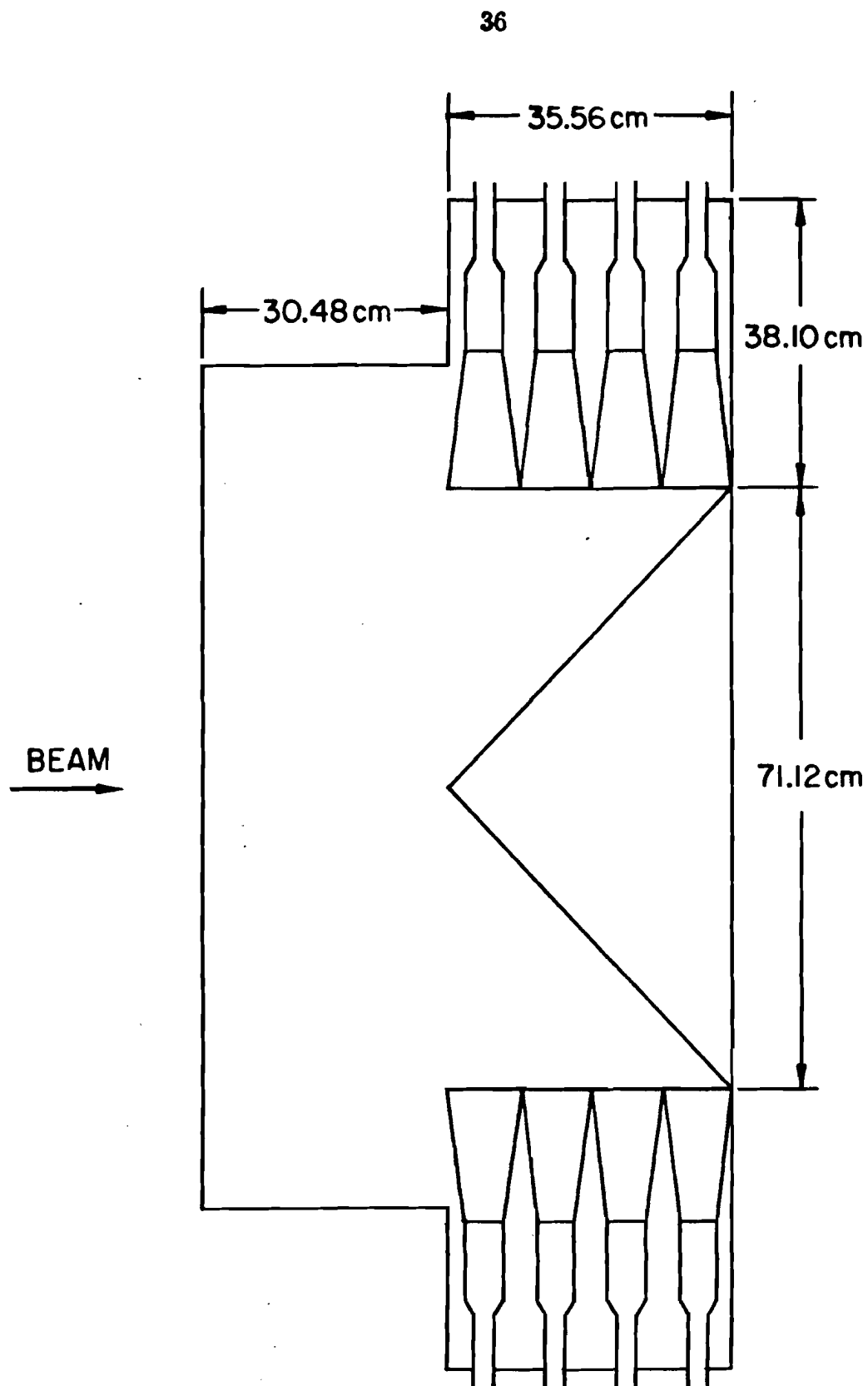
Figure II.7: CO Physical Layout

37

BENDING VIEW
C2

1 m

BEAM

NON-BENDING
VIEW
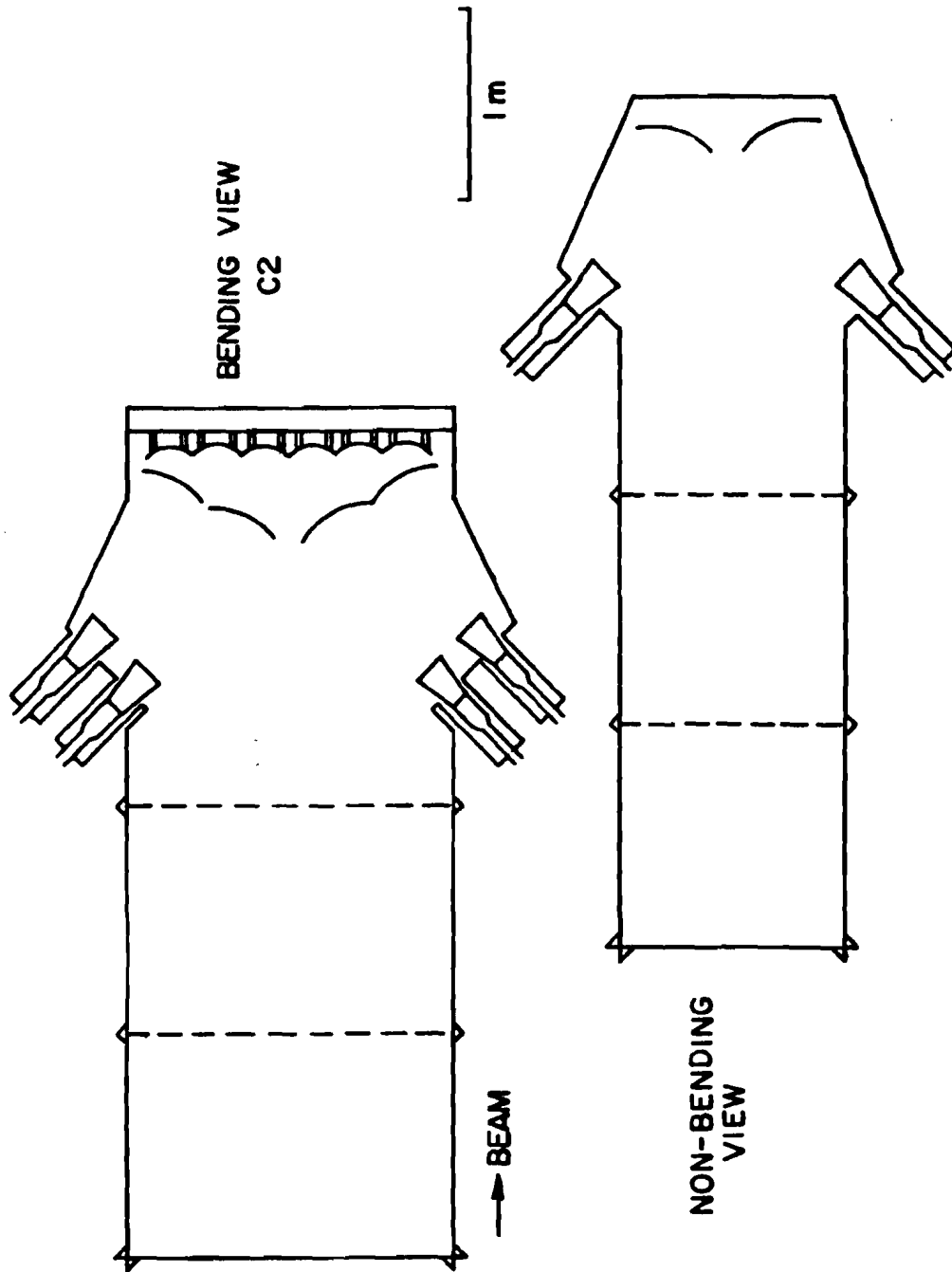
Figure II.8: CY (and CB) Physical Layout
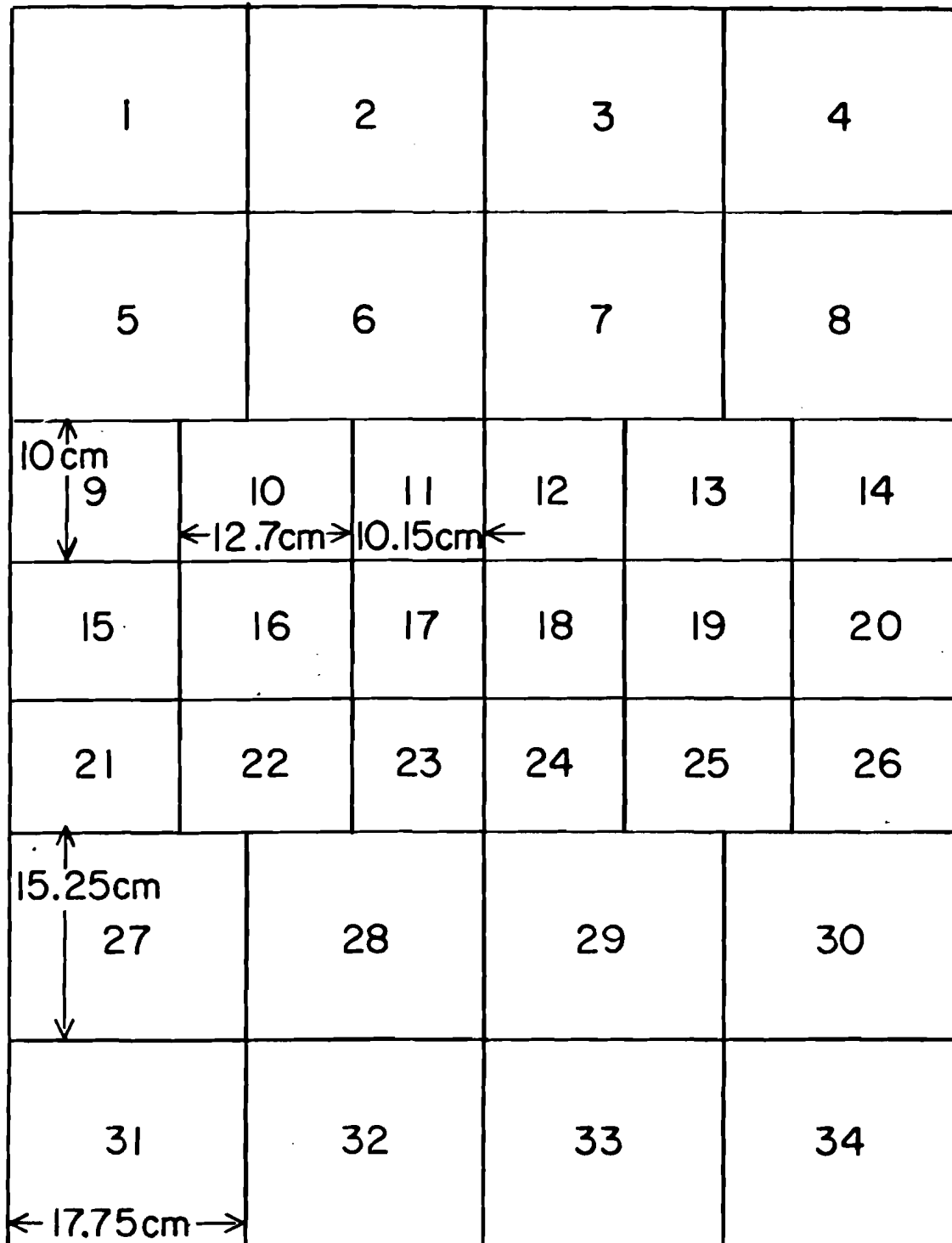
Figure II.9: CO Cell Image
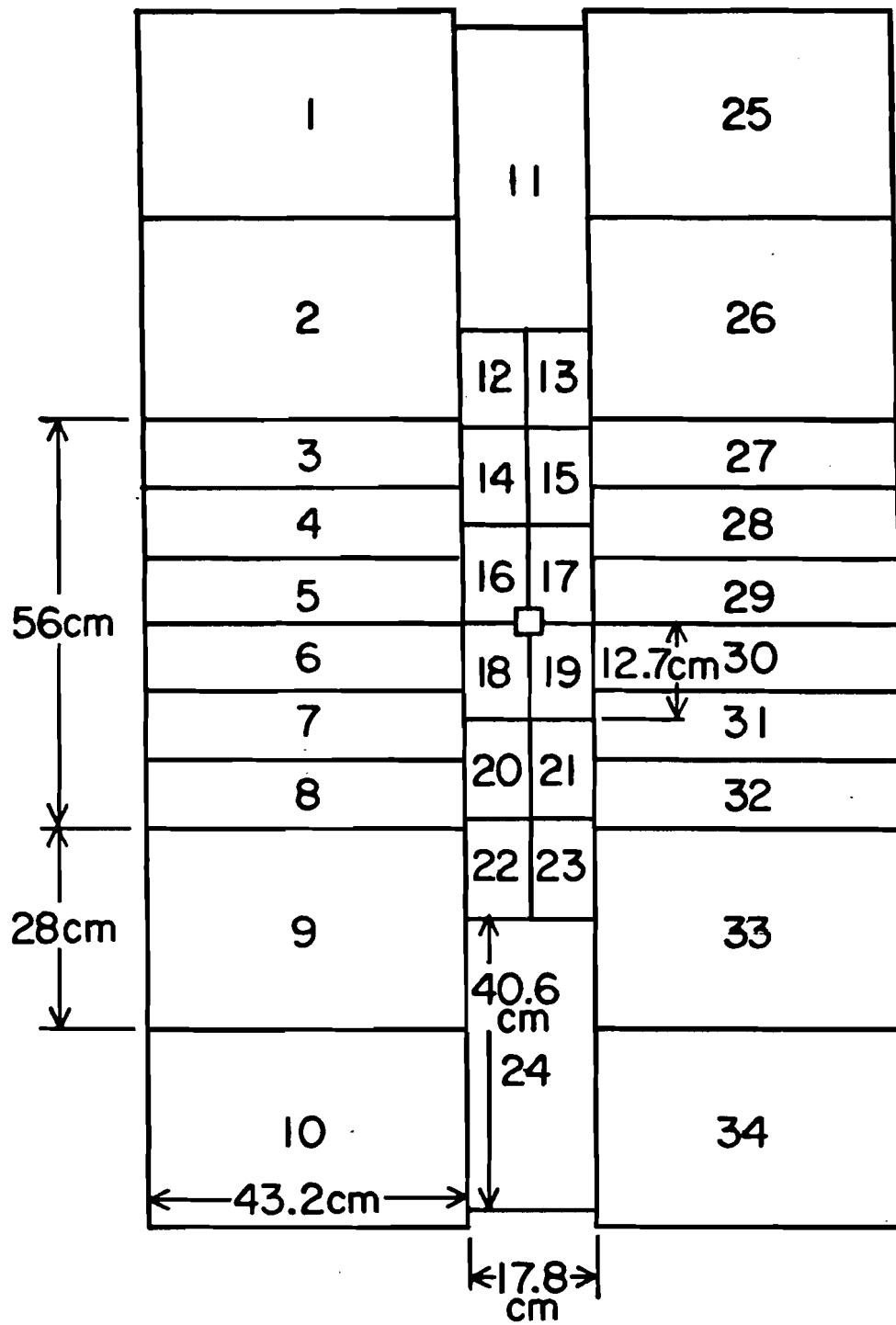
Figure II.10:   CY and CB Cell Image
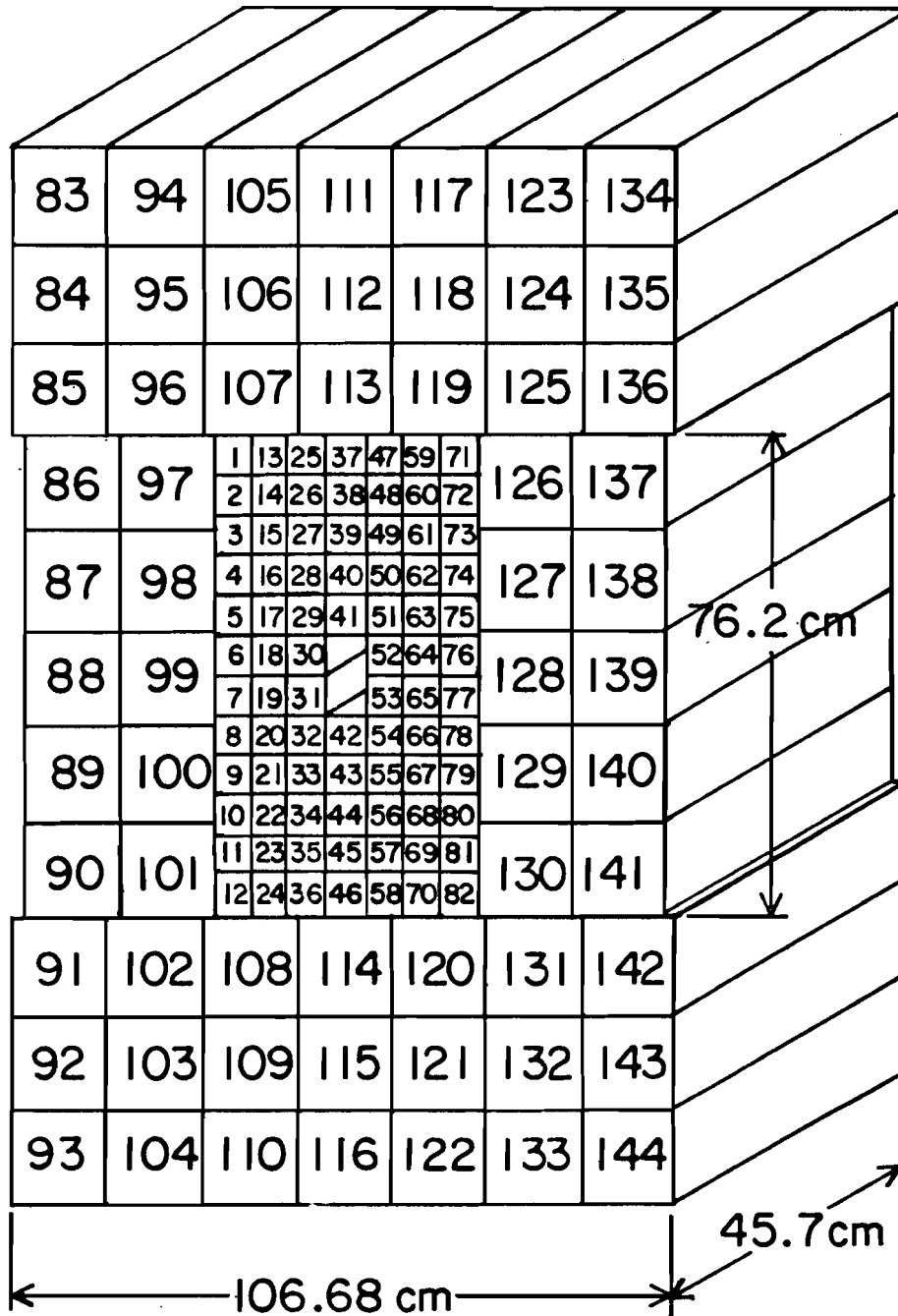
Figure II.11:   Lead Glass Array

TOP VIEW

157cm

4.45cm

STEEL
PLATE

BEAM VIEW OF HADRON CALORIMETER
WITH DETECTOR ARRANGEMENT SHOWN

HC6   HC1

7   2

8   7.62 cm
Hole   15.25cm   3

9   45.7 cm   4

10   5

84cm

TOP

RIGHT
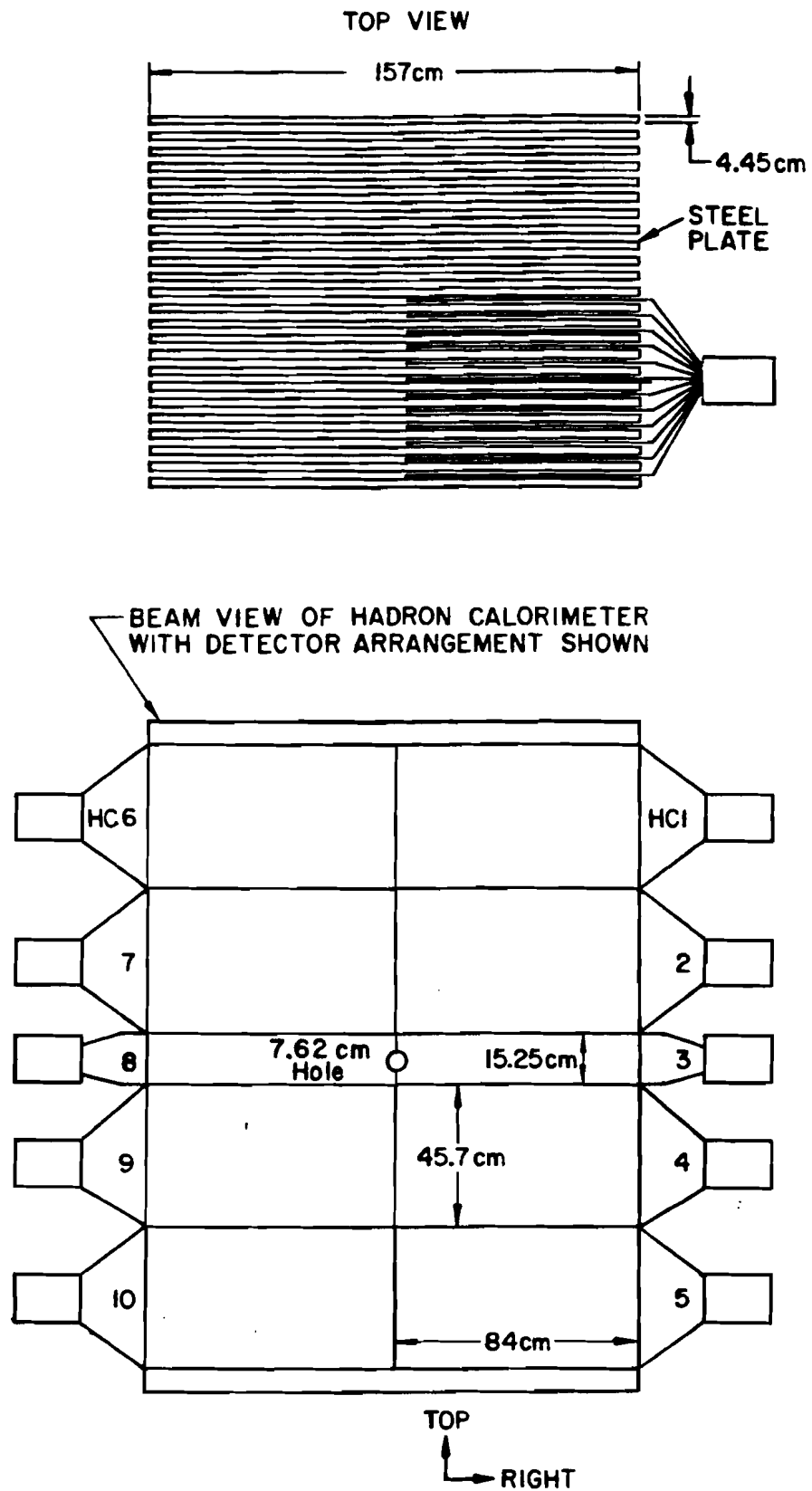
Figure II.12:   Hadron Calorimeter

TOP VIEW

BEAM →

15.2 cm

20.3 cm

0.635 cm
SCINTILLATOR

2.54 cm
W PLATE

BEAM VIEW

20.3 cm

15.2 cm

20.3 cm
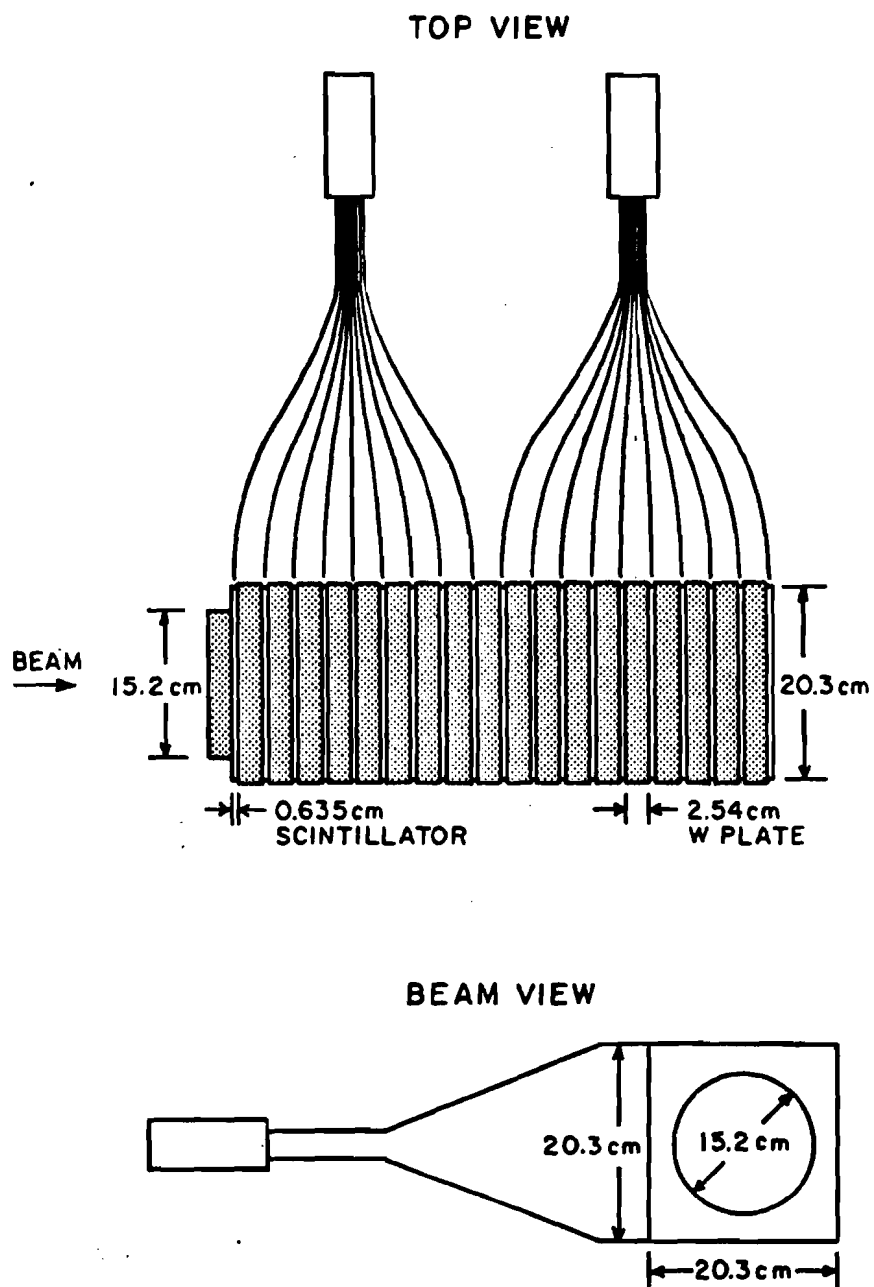
Figure II.13:   Beam Dump Calorimeter

36			I
35		2
34		3
33		4
32		5
31		6
30		7
29		8
28	50.8cm	9
27		10
26		11
25	35.56cm	12
24		13
23		14
22		15
21		16
20		17
19		18

142cm

112cm
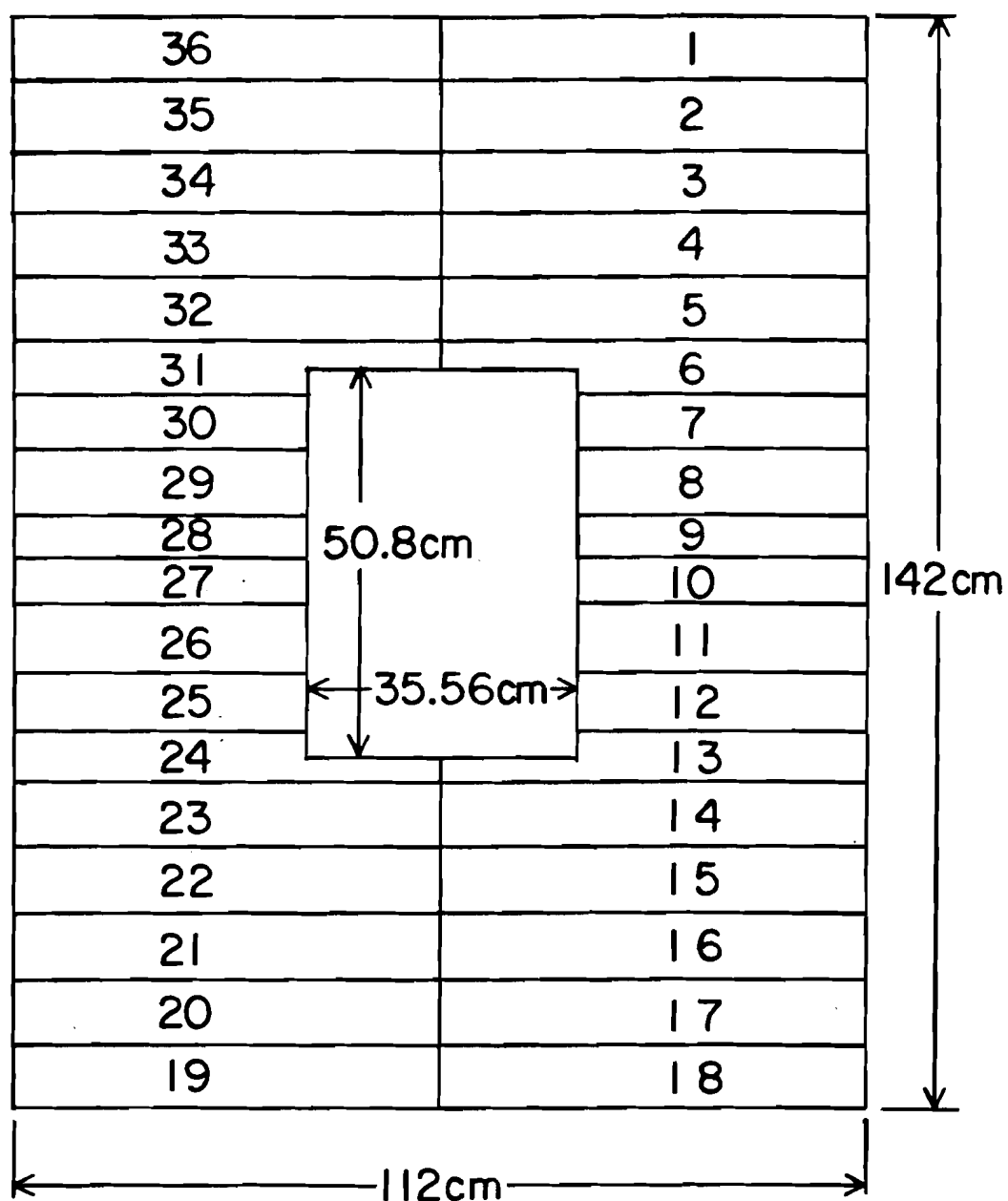
Figure II.14:   Outer Electrophotometer
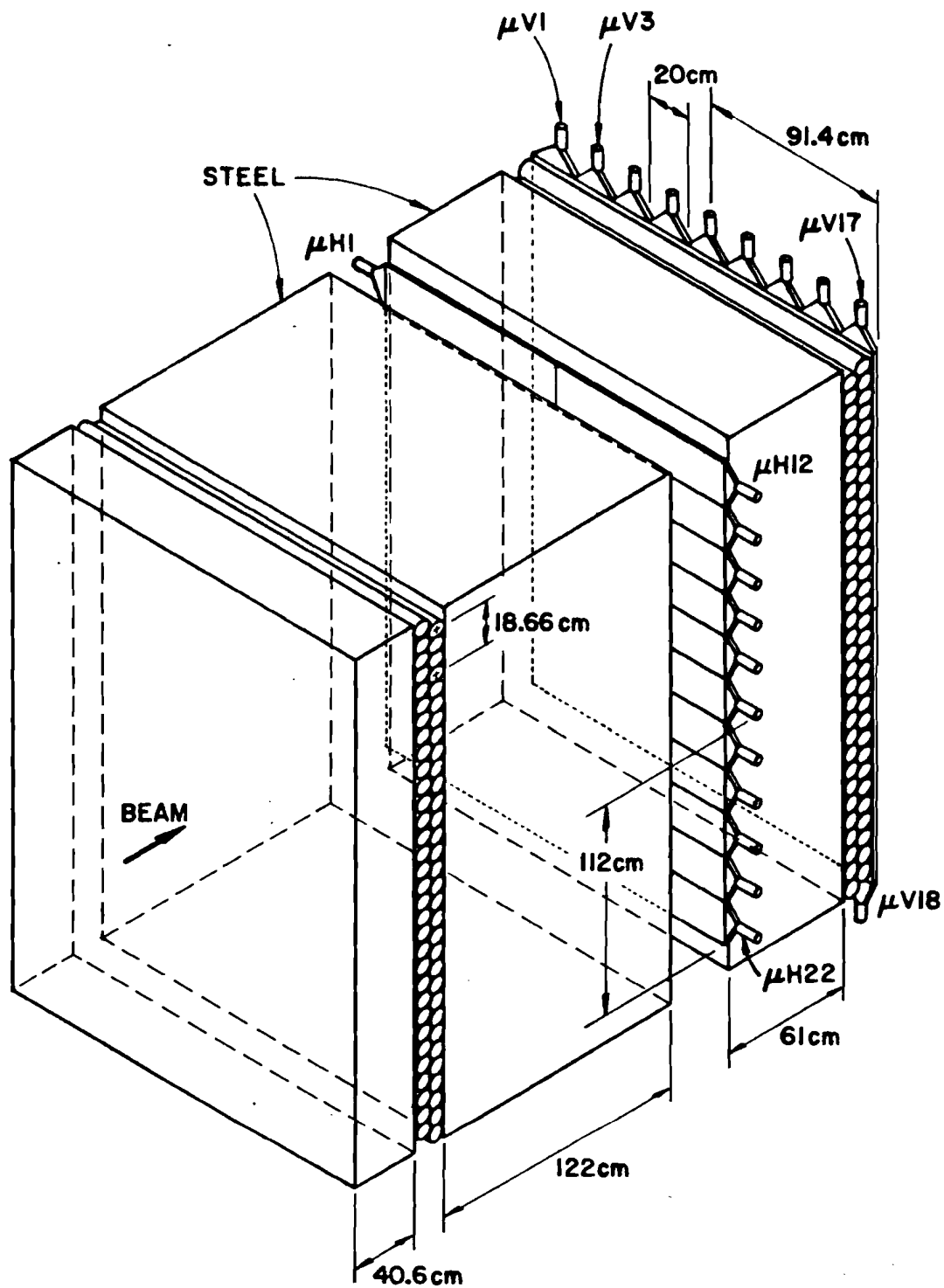
Figure II.15:   P-tubes, μH, and μV

E400 Data Aquisition System
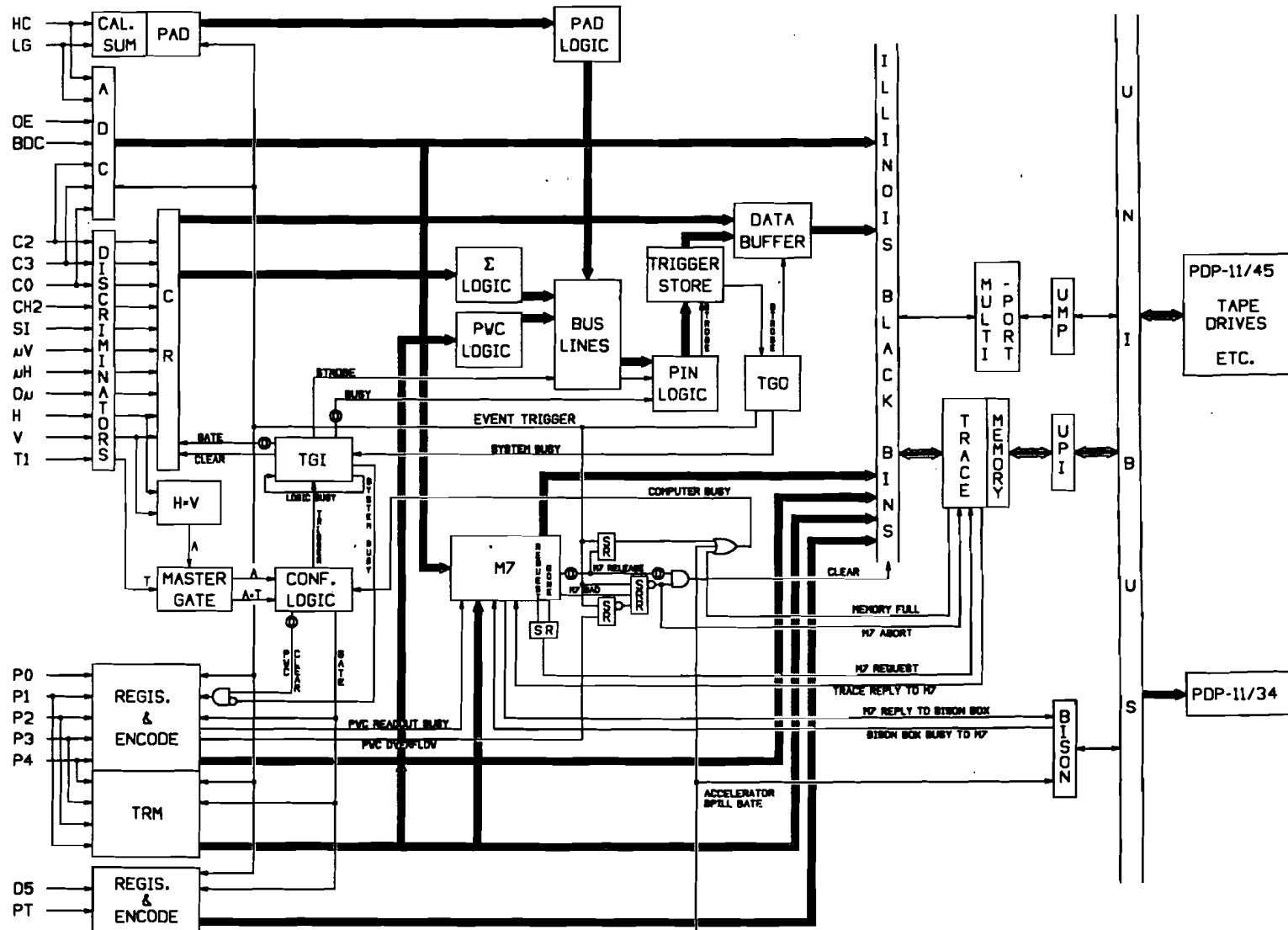
Figure II.16:   Data Aquisition Schematic
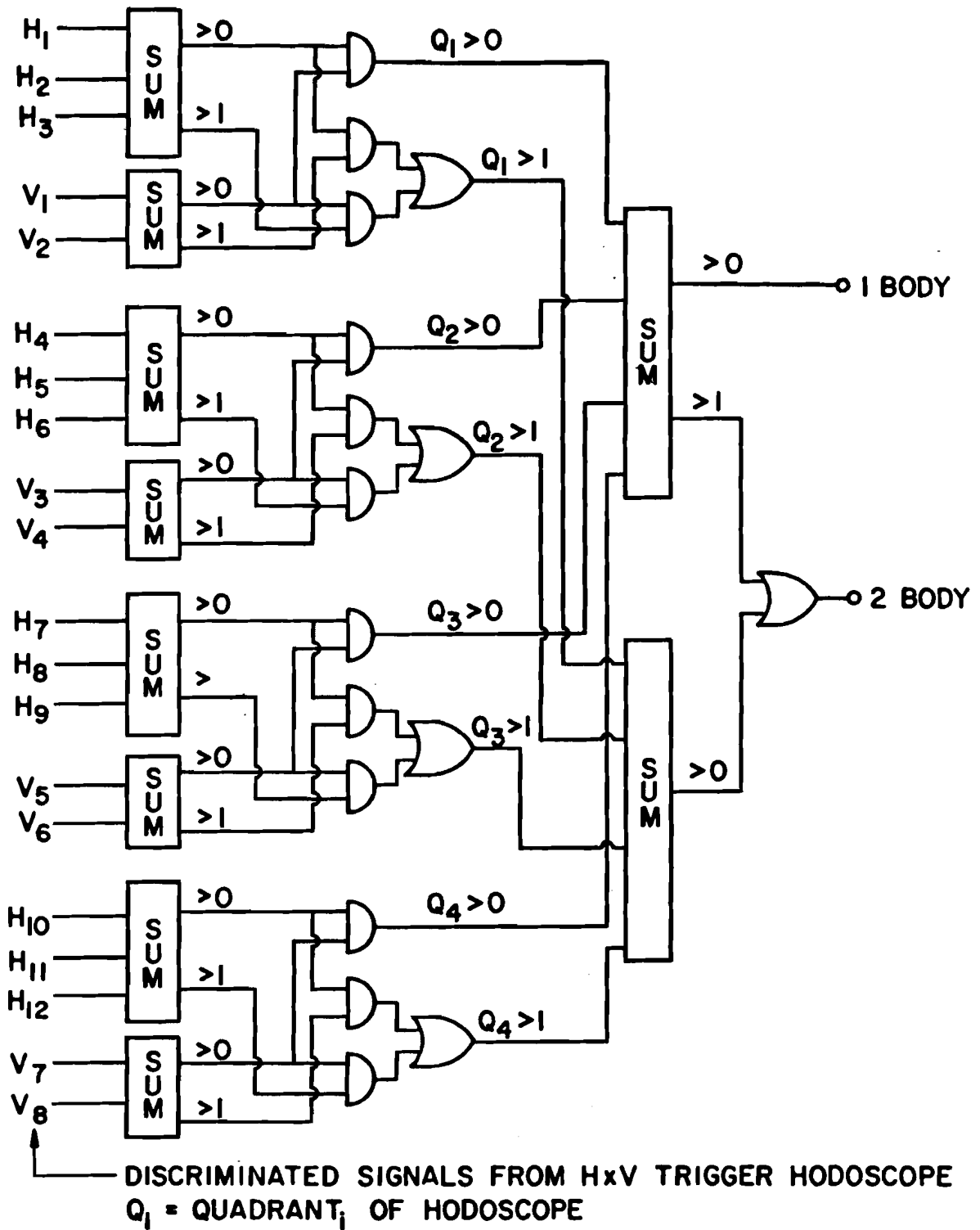
Figure II.17:   H×V Logic

CONFUSION LOGIC SCHEMATIC
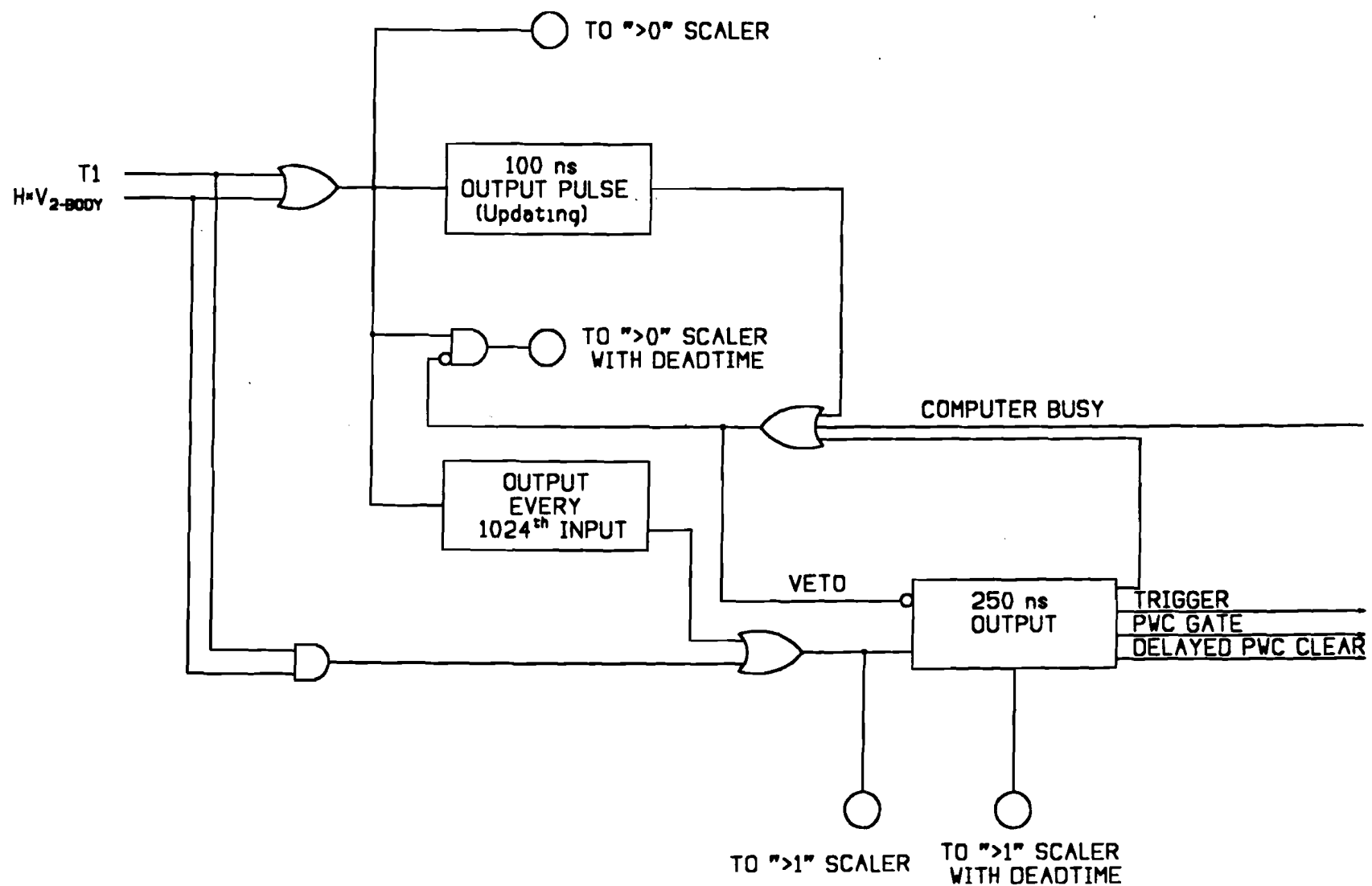
Figure II.18: Confusion Logic
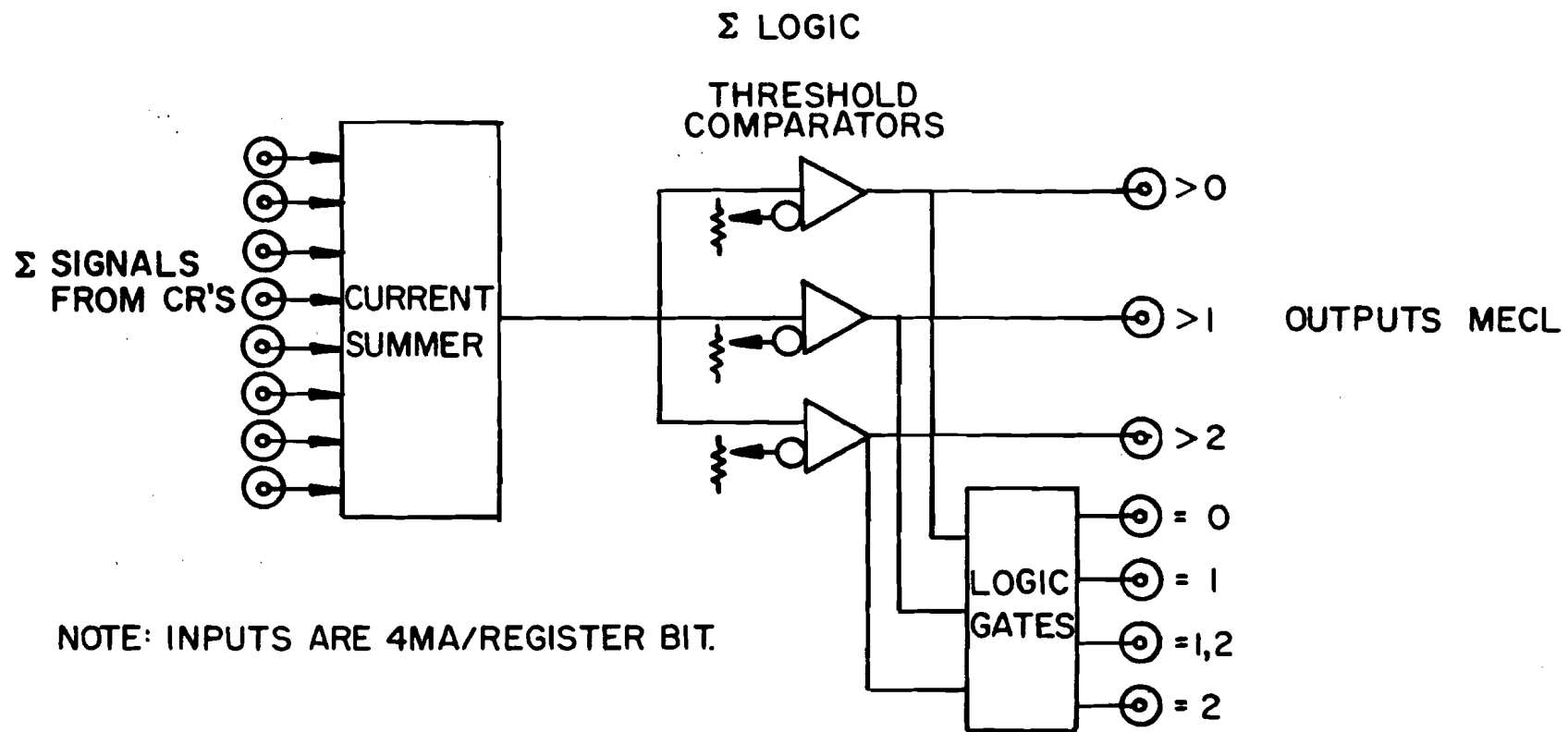
Figure II.19:   Sum Logic for CR's
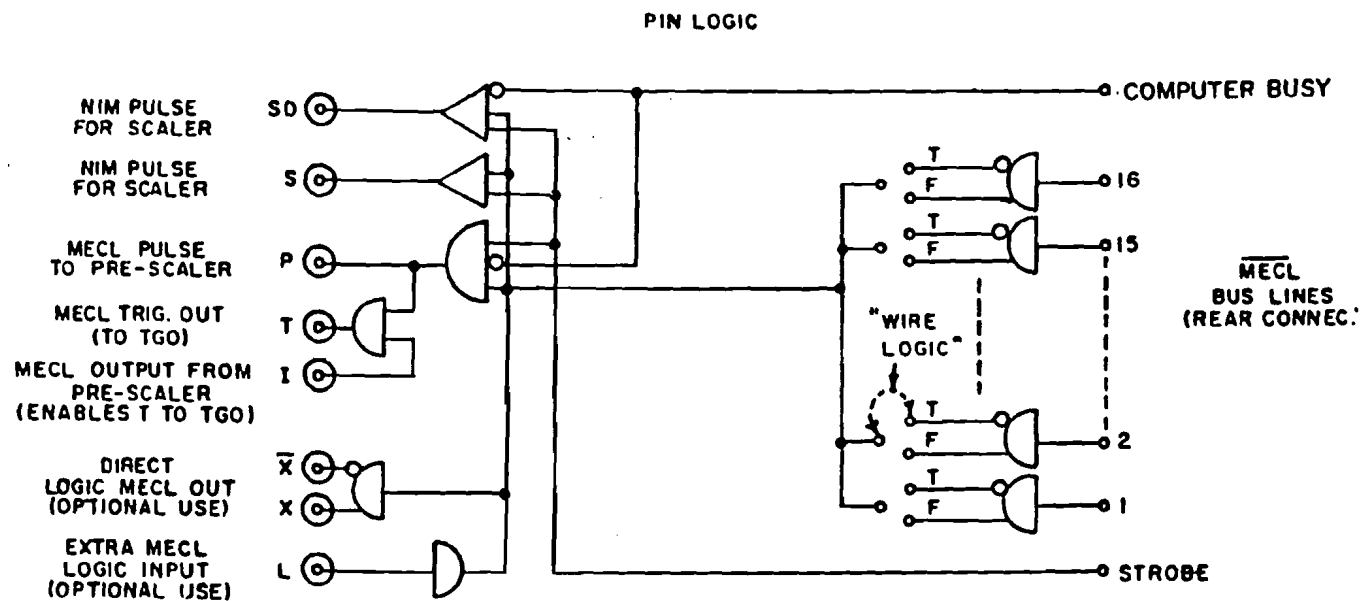
PIN LOGIC

Schematic logic diagram of Pin Logic Module

Figure II.20: Pin Logic

Table II.1
Target, Tracking, & Trigger

	Z (cm)	Length (cm)	Active Area (cm²)	Wire Spacing (cm)	Total # of Components	Interaction Length	Radiation Length
Target						.0192	.128
W	0.0	.03	2.×2.		1	.0031	.086
Si	2.67	.425	2.×2.		30	.0063	.024
Be	5.41	.4	2.5×2.5		1	.0098	.011
Si	8.33	.11	2.×2.		3	.0016	.006
D5		12.0	4.7×4.7				.006
Triplet 1	12.08	.82		.025	600		
Triplet 2	17.32	.82		.025	600		
Triplet 3	22.57	.82		.025	600		
T 1	35.99	.64	7.6×7.6		1		.0055
M 1	137.7	101.6	35.6×20.3				.0015 (He)
P0	226.9		44.7×70.4				.002
X				.1999	224		
V				.2000	352		
U				.2000	352		
P1	313.2		49.0×78.2				.002
X				.2037	256		
V				.2037	384		
U				.2037	384		
P2	448.9		76.7×112.8				.002
X				.2001	384		
V				.2003	576		
U				.2003	576		
M2	637.9	182.9	50.8×61.0				.0018 (He)
P3	800.4		83.3×112.8				.002
X				.2001	416		
V				.2000	576		
U				.2000	576		
P4	1326.2		100.6×153.6				.002
X				.3002	336		
V				.2000	768		
U				.2000	768		
H×V	1554.4	1.28	106.6×160.0		20		.011

Table II.1:   Target, Tracking, & Trigger Specifications

Table II.2

Particle Identification

	Z (cm)	Length (cm)	Active Area (cm²)	Total # of Components	Radiation Length
CO	386.4	66.1	71.1×91.5	34	.013
Oμ	764.2	1.28	152.4×185.4	18	
CY	1051.1	460.0	104.0×168.0	34	.03
CH2	1297.0	.64	104.0×168.0	34	.018
CB	1442.4	203.0	104.0×168.0	34	.02
PT	2113.4	10.2	152.0×227.0	72	
μH	2275.4	.64	180.0×220.0	22	
PT	2358.4	10.2	152.0×227.0	72	
μV	2381.4	.64	180.0×224.0	18	

Table II.3

Calorimetry

	Z (cm)	Length (cm)	Active Area (cm²)	Total # of Components	Interaction Length	Radiation Length
OE	510.1	55.9	112.0×142.0	60	.52	16
LG inner	1597.4	58.4	31.7×76.2	82	.63	20.8
LG outer	1591.0	45.7	91.7×165.0	62	.55	18.1
HC	1777.4	198.7	157.0×198.0	20	6.4	60.6
BDC	1906.4	54.3	20.3×20.3	2	5.	54.

Tables II.2 & II.3:   Particle Identification and Calorimetry

Chapter III: Data Processing

III.A. History

The data that are analysed here were taken from April 27 to May 17, 1984. These are
the data that were taken under a stable set of triggering conditions after the experiment
was turned on and all components were adjusted and calibrated. These data are a
subset of the total amount mentioned in section II.D and consisted of 21 million triggers
contained on approximately 500 magnetic tapes. The analysis of these data took place
in various stages.

III.A.1. Reconstruction

Pass 1 or the Reconstruction[27,28,29] (7/84-2/85) performed tracking in the five wire
chambers of the main spectrometer. E400 was different from many experiments in
that it had only 5 high efficiency PWC's. Many other experiments have a large array
of PWC's and drift chambers which results in very slow track-finding reconstruction
programs. The Reconstruction program took the hits in the chambers, performed a χ^2
minimization, and converted them into trajectories which were parameterized by the
χ^2, the number of degrees of freedom, the intercept in x, the slope in x, the intercept
in y, the slope in y (these last four at the center of M2), and the change in the slope of
y through M2. To find these trajectories, straight lines were found in the X, U, and V
projections from the hits in P0, P1, and P2 and were extrapolated to the center of M2.
These points in M2 were then used to continue the trajectories by matching with hits
in P3 and P4. Then consistency between the three projections was checked. These full
spectrometer trajectories were called "tracks". The bend in the trajectory in M2 could
be used to determine the particle's momentum. (Appendix A describes improvements
on this tracking procedure)

Chamber hits in the P0, P1, and P2 that were not used to form full five chamber
tracks could then be used to form line segments called "stubs". Hits that still were not
used could be used to form reconstruction vee's which were V^0's, Λ's and K_s's, that
decayed between P0 and P2 (see section III.C).

III.A.2. Pass 2

Pass 2 (4/85-2/86) refined a number of the parameters found in Pass 1. Once the momentum had been determined to some degree in Pass 1, some of the momentum corrections described in Appendix A were applied. The corrections that were used in Pass 2 were the P0 correction and primitive forms of the weak focusing and B_y corrections. The momentum was then refined by refitting the tracks. Also the stubs were extrapolated back through M1 to the center of the target. The bend through M1 provided a first approximation to the stub momentum. Using track and stub information, vertices could be found. The magnetic corrections just described for the tracks were then applied to the stubs. More V^0's were found using combinations of tracks and stubs which gave vee's that decayed between the target and P0. Also in Pass 2, the Čerenkov identification was done. Finally the energy sum of the Lead Glass, Hadron Calorimeter, and Beam Dump Calorimeter was computed. The V^0 finding, particle identification, and energy sum are described later in this chapter.

III.A.3. Physics Skim

The first Physics Skim (1/86-3/86) reduced the number of data tapes from 500 to approximately 100. Approximately 10 promising and interesting states including: clean V^0, $D^* \rightarrow (K \pi) \pi$, $D^+ \rightarrow K \pi \pi$, Λ_c, ϕ, μ, Σ kinks, and Ξ kinks were collected and flagged. These tapes could then be quickly run to pull off a specific state to be intimately analysed.

The candidates for the signal for this thesis were selected in the Physics Skim. For $D^* \rightarrow (K \pi) \pi$ the mass of the $K \pi$ combination was required to be 1.864 Gev $\pm$ 150 Mev. The mass difference between the $(K \pi) \pi$ mass and the $K \pi$ mass was required to be less than 160 Mev. The K was required to be identified by either of the Čerenkov algorithms as a definite kaon (K_{def}) or as ambiguous between kaon and proton (K/P_{amb}) and was required to be oppositely charged from the π from the D^0 as both D^0 and $\overline{D}^0$ were collected.

III.A.4. Pass 3

The final general analysis program, Pass 3, was performed on the 100 skim tapes (1/86-6/86). Pass 3 incorporated the Vertex Chamber and the TRM's into the tracking. The hits in the Vertex Chamber were converted into track segments and were linked

with the tracks and stubs in the main spectrometer. The TRM information could give a track location between wires instead of just the nearest wire. Position resolution at the target was then defined by the superior resolution of the Vertex Chamber. Momentum and angular resolution were then limited by the main spectrometer due to its long lever arms (see Appendix D). Momenta and vertices were recalculated.

III.A.5. Revised Pass 3

It was decided that some of the criteria used in the Physics Skim was too restrictive, so a revised Pass 3 was performed (6/87-8/87). For instance, the $\pm$ .150 Gev cut on the D^0 had barely enough data outside the signal region to enable a determination of the background. Also the selection of the D^* signal for the Physics Skim included Čerenkov cuts. It was decided to analyse the D^* signal without the Čerenkov cut so Pass 3 was run on all 500 of the data tapes using the enhanced computing power of Fermilab's Advanced Computer Project (ACP) to cut down on running time.

III.A.6. Revised Physics Skim

A second Physics Skim (revised) (10/87-11/87) was done on the Revised Pass 3 tapes to address the limitations listed above. These tapes were skimmed for $D^* \rightarrow$ (K π) π according to the criterion described above but without the Čerenkov requirement and with the mass cut on the D^0 expanded to ± 250 Mev.

The specific analysis for the decay $D^* \rightarrow$ (K π) π is described in detail in chapter IV.

III.B. Čerenkov[30,31]

As described above, the experiment had 3 Čerenkov counters. The information from them was used in the Pass 2 to identify each of the tracks in an event. Two different (but not completely independent algorithms) were used. Both algorithms compared the detected amount of light with the amount predicted for each track but the actual assignment of identity was different. The algorithm LOGIC was an extension of the approach used by E400's predecessors and was quite fast. The other, CERAL, was slower and more elaborate. CERAL was developed for this experiment and the two were used together because each had different strengths and weaknesses (for a more detailed description see references 30 and 31).

III.B.1. LOGIC

LOGIC took the position of a trajectory at the cell image plane for each of the detectors and searched the incident cell and any adjacent ones within the Čerenkov ring to see if any were "on". A cell was declared "on" if the ADC reading was 10 or more counts above pedestal, which suppressed noise with only a slight loss of efficiency as one photon produced 120 counts above pedestal. Next, the track was assumed to be a pion and a prediction was made of the amount of light the track should have produced based on its momentum. If the cell was "on" and the prediction was for more than .2 photons, then the track was flagged as "on". The track was flagged as "off" if the cells were off and more than 2.5 photons were expected. If neither of these criteria were satisfied then the track was "confused". Then, the momentum of the particle was compared with the thresholds for the counter (listed Table III.1) and the following status word was set:

No bits "on": Indeterminate.

Bit 1 is "on": Consistent with being an electron.

Bit 2 is "on": Consistent with being a pion.

Bit 3 is "on": Consistent with being a kaon.

Bit 4 is "on": Consistent with being a proton.

The final identification was done by taking the status word for the track from each counter and "anding" them together. Each bit retained the above meaning while 0 now meant that the information was inconsistent and 15 meant that the system was totally confused. Confusion could occur if the particle passed through a crack between mirrors, had a momentum close to the counter thresholds, or clustered too close to other tracks. About 80% of the tracks were identified as pions by LOGIC. Figure III.1 shows the momentum regions of the different identities and Table III.1 shows the identification matrix for LOGIC.

III.B.2. CERAL

CERAL used status words similarly to LOGIC, but "on-ness" was determined differently. CERAL considered all possible identities to calculate the predicted light. Whereas LOGIC only used the ADC counts as thresholds, CERAL tried to calculate the actual number of photons detected and compare that number to the predicted amount.

CERAL grouped tracks into clusters (usually 4 or less) and tried all possible identifications for each track to set the bits on or off. The final determination was again done by "anding" the three words together. The identification matrix of CERAL is similar to that of LOGIC. However, the transition momentums are not distinct in CERAL because CERAL tried all identities and compared actual light to predicted light instead of thresholds as in LOGIC. Therefore CERAL identifications could extend beyond the threshold values of LOGIC.

Studies of Λ's and K_s^0's have shown considerable disagreement (on the order of 50%) between the two algorithms when identifying "definite" particle identity. For example, LOGIC has been shown to identify more protons from Λ decays as a definite proton (P_{def}) than K/P_{amb} as compared to CERAL. Generally the "or" of LOGIC and CERAL was used for particle selection in any analysis.

III.C. V^0 Identification

The Reconstruction program identified V^0's which originated between P0 and P2 (called Reconstruction V^0's), but a great many decays of K^0's and Λ's occurred upstream of P0. The Pass 2 program attempted to isolate these tracks, remove them from the determination of the primary vertex, and assign them to a V^0 when appropriate to do so. The identification algorithm for the main category of V^0's, "0- and 1-attached", is described here followed by a brief description of other types of V^0's.

The distance of closest approach (DCA), of each track, to the primary vertex was calculated. If a track's DCA was less than 0.1 inches, then the track was said to be "attached" to the primary vertex. If a stub's DCA was less than 0.08 inches (using only the non-bend component), then the stub was attached to the primary vertex.

V^0 candidates were constructed from pairs of oppositely signed tracks which met (using the non-bend intersection) at least 3 inches downstream from the primary vertex. These pairs were flagged as V^0 tracks only after passing certain conditions:

1) Both tracks in the pair were not attached to the primary vertex which was done primarily to avoid the large level of background obtained from considering doubly-attached pairs.

2) One track in the pair must be a full track to give momentum information.

3) Both tracks from a given pair must not be associated with other V^0 candidates.

A complicated arbitration scheme evolved which selected those pairs which appeared to be associated with real neutral-particle decays.

The pairs under consideration in this arbitration scheme were classified as a track-track pairs or track-stub pairs and then they were further classified as singly-attached or unattached (to the primary vertex) for a total of four classifications. In the following description, DCA_Z refers to the separation distance between the 2 tracks at the Z of the decay and $P_\perp$ balance refers to how well the V^0 momentum (as computed from the charged track pair) extrapolated back to the primary vertex. The arbitration scheme then proceeded as follows:

1. Arbitration between track-track pairs.

   1.a. Pairs were chosen which had significantly smaller DCA_Z or significantly better $P_\perp$ balance.

   1.b. If this arbitration failed to make a decision, then unattached pairs were selected over singly-attached.

   1.c. Finally, if these tests failed, then the track-track pair with the best DCA_Z was kept.

2. Then, arbitration involving only track-stub pairs was done.

   2.a. The selection favored pairs which "originated" significantly further downstream or pairs with significantly better $P_\perp$ balance.

   2.b. If these tests failed to select a pair, then unattached was favored over singly-attached.

   2.c. The final step selected the pair that originated furthest downstream.

3. Arbitration between a track-track pair and a track-stub pair was done in an manner identical to part 2 above except the final step of arbitration kept the pair giving the best $P_\perp$ balance.

Distributions of the invariant masses (π-π and P-π) for those pairs which survived the arbitration and for those which failed are shown in Figures III.2 and III.3. Losses primarily occurred in the singly-attached category where large background levels existed.

Searches for "unconventional" V^0's included efforts to identify Reconstruction V^0's from unused wire hits allowing for a missing hit in any one wire chamber (acting on the belief that chamber inefficiencies may have accounted for a missing hit). Also, stub-stub V^0's and V^0's which opened up in M2 (called P34 V^0's since only chambers P3 and P4 could have given hits for these tracks) were isolated with the help of a constrained-vertex fitter which demanded $P_\perp$ balance.

III.D. Event Energy[32]

The total event energy used in the analysis was determined by the expression:

$$E_{TOT} = 1.05 \times E_{HC} + E_{LG} + E_{BDC} + 1.5 \times E_{STUB} + 10 \qquad \text{(in Gev).} \qquad \text{(III.1)}$$

where E_{HC}, E_{LG}, E_{BDC} represent the energy collected in the Hadron Calorimeter, the Lead Glass, and the Beam Dump Calorimeter respectively. E_{STUB} is the total energy of the particles that did not pass through M2 and had momentum less than 25 Gev. The multiplier of 1.5 assumes that there were half as many π^0's as charged π's and that the positions were correlated with the charged π's. This stub term represents only 10% of the total event energy. The materials in the Lead Glass are chosen to favor electromagnetic interactions over hadronic interactions. However since the Lead Glass is about .6 interaction lengths, hadronic events will occur. The multiplier of 1.05 corrects for the hadronic energy deposited in the Lead Glass but not properly measured. The last term of 10 Gev accounts for the very wide angle trajectories that do not pass through M1. Figure III.4 shows the total reconstructed energy for Pin 2 and Pin 4 events. The curve in the figure represents a ramped spectrum with peak energy of 690 Gev with a 14 % energy resolution. This distribution was compared to a direct measurement of the output from the ADC's of a special run where the beam interacted directly with the Beam Dump Calorimeter and was found to be in agreement.

III.E. Monte Carlo

The acceptance of the spectrometer and analysis programs must be determined from Monte Carlo studies in order to calculate a cross-section. The analysis presented in this thesis uses an acceptance calculation that is designed to be relatively free of the production model used in the Monte Carlo. It relies on parameterizing the acceptance

as a function of the energy or x_F of the state and therefore should not depend greatly on the method by which a particle attained that energy or x_F (this concept is described in detail in section IV.C).

The simulation was conducted in three stages. Events were generated and all short-lived particles were decayed to stable decay products. Then the Monte Carlo itself simulated the passage of the particles through the E400 spectrometer. Simulated data tapes were written and were processed through the same analysis programs as the data.

The first part of the simulation was the "event generator". Generation of charm particles was done in the context of the gluon-gluon fusion model. In this model counting rule distributions were picked for x_1 and x_2 (the momentum fractions of the two gluons in the center-of-mass of the colliding nucleons) of the gluons. The gluons then interacted according to the formulas given in Ellis and Sexton[21] (in the parameterizations given in equations I.3 and I.4). The resulting $c\bar{c}$ pair from the interaction turns into a charm and an anti-charm particle dressed in the center-of-mass of the $c\bar{c}$ pair. The particles are given a fraction Z (a flat distribution from 0 to 1) of the charm quark's momentum in the $c\bar{c}$ system.

One charm particle from the $c\bar{c}$ pair was generated to simulate the specific state desired (in this thesis $D^* \rightarrow (K \pi) \pi$). The recoiling particle was generated generically into any possible charm particle. The energy of the original gluons was subtracted from the s of the interaction. The remaining energy was divided evenly between a forward and backward hadronic jet. These jets were hadronized by the Feynman-Field prescription[33].

After all the primary particles had been determined, short-lived particles were decayed to stable descendents. The decay of the recoil charm particle and the hadronic debris was done randomly according to decay chains and rates from experimental measurements and statistical models. The inclusion of the recoil charm particle was important because of our heavy-particle (kaon) trigger. While we are relatively insensitive to any bias, the kaons from the recoil particle could affect the acceptance calculations. After the stable particles had been determined, their momentum vectors, particle identities, and decay positions were given to the Monte Carlo program.

This Monte Carlo was the CERN program GEANT which had been customized to simulate the E400 spectrometer. GEANT computed the trajectories and any decays downstream of M1. GEANT simulated particle interactions in the various detector components and produced signals from these components in the same form as the real detectors.

The simulated data from GEANT was then passed to the same analysis chain as was used for the data. Along with the data, the values that were given to GEANT from the event generator were passed through the analysis chain to enable comparisons between the generated and reconstructed values.

The event generator also produced energy and x_F distributions of the generated states. Comparing the energy and x_F distributions for the reconstructed states with these generated distributions gave the reconstruction efficiency. This efficiency, the ratio of the reconstructed to the generated distributions, can be used to weight the observed signal to calculate the total signal produced. Actual acceptance curves and further discussion of how the acceptance was determined is presented in Chapter IV.

Figure III.1: Čerenkov Identification Ranges, LOGIC

The shaded areas show the momentum ranges where π_{def}, K_{def}, K/P_{amb}, and P_{def} identifications are possible using the algorithm, LOGIC.

(a) K_S Arbitrated IN
(b) K_S Arbitrated OUT

Figure III.2: K_s^0 Arbitration Results

(a) shows the events that pass the arbitration cuts. (b) shows the events that are rejected.

(a) Λ Arbitrated IN   (b) Λ Arbitrated OUT

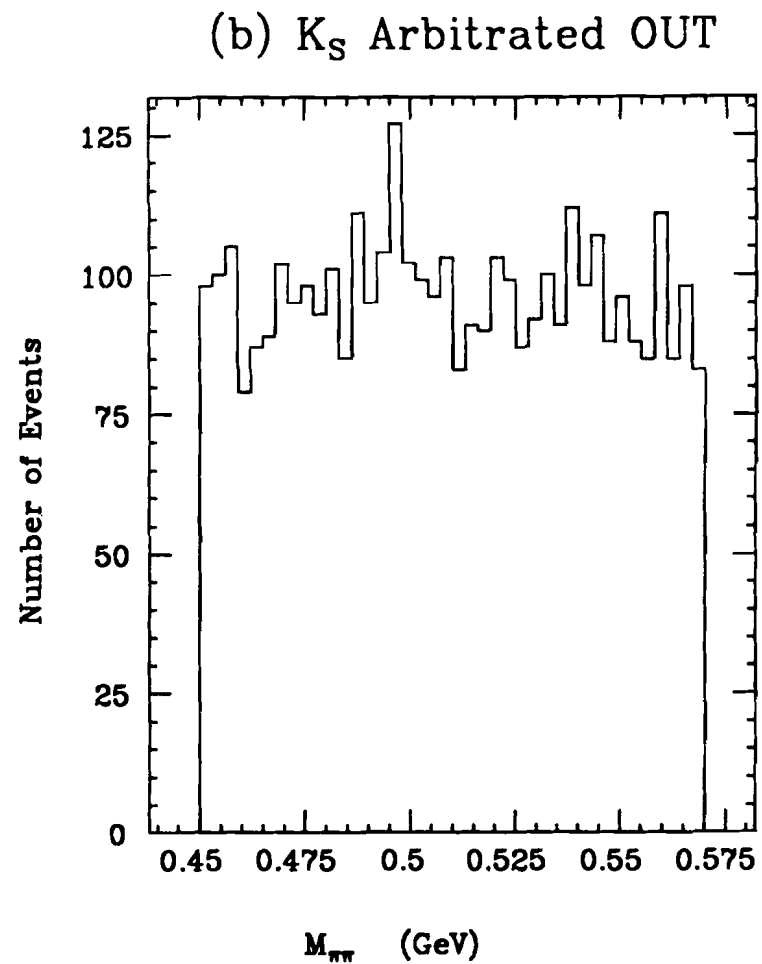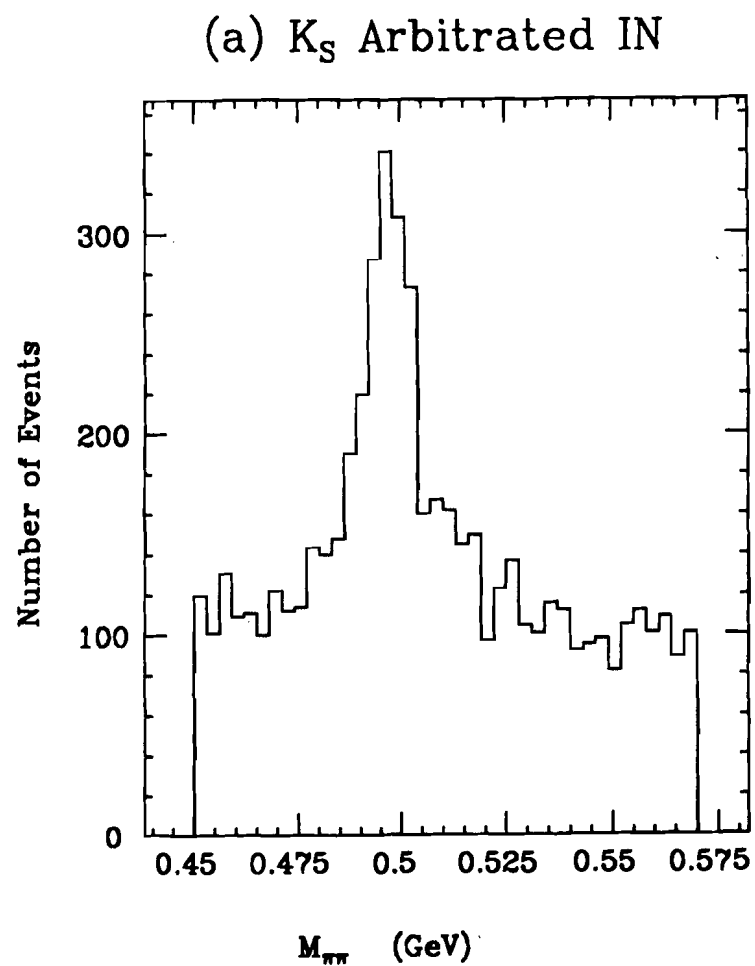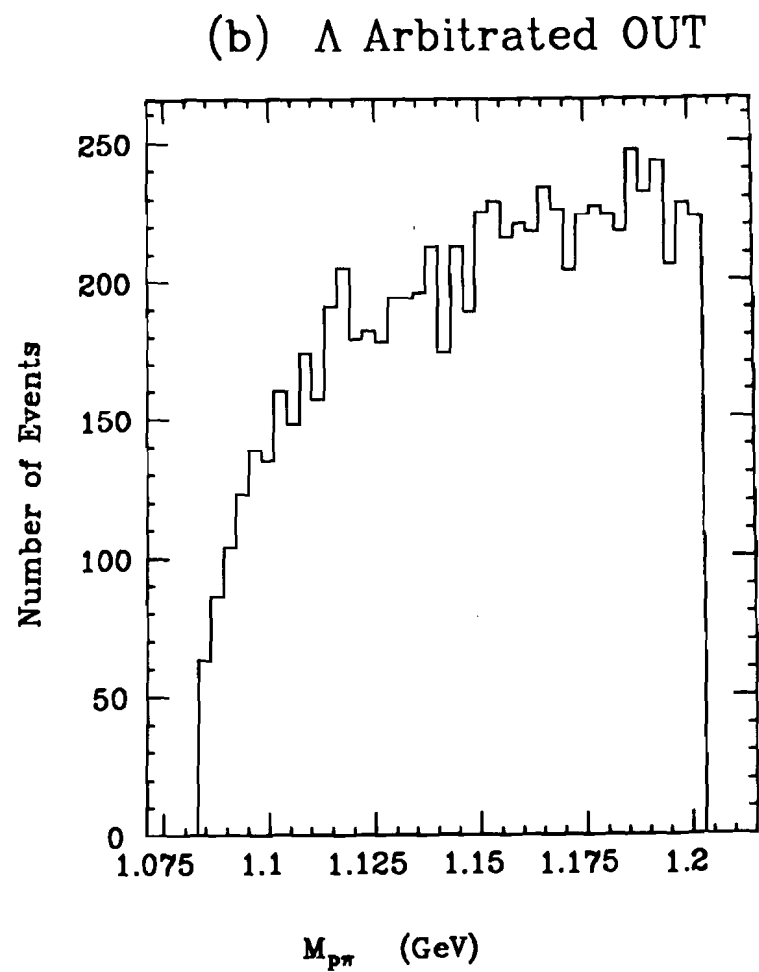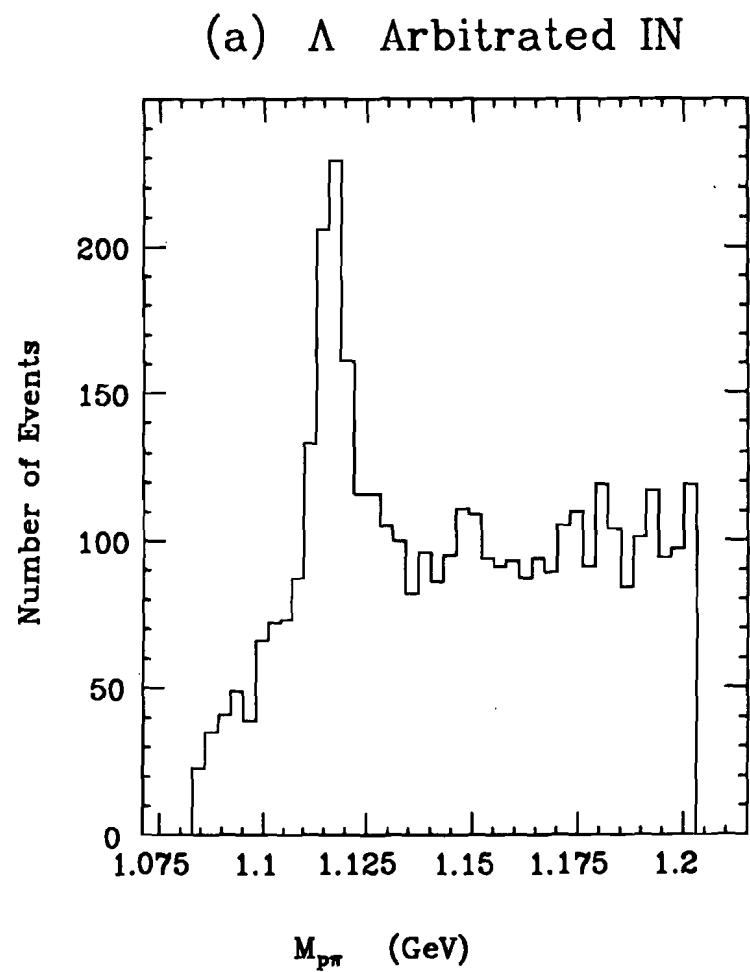Figure III.3:   Λ Arbitration Results

(a) shows the events that pass the arbitration cuts. (b) shows the events that are rejected.
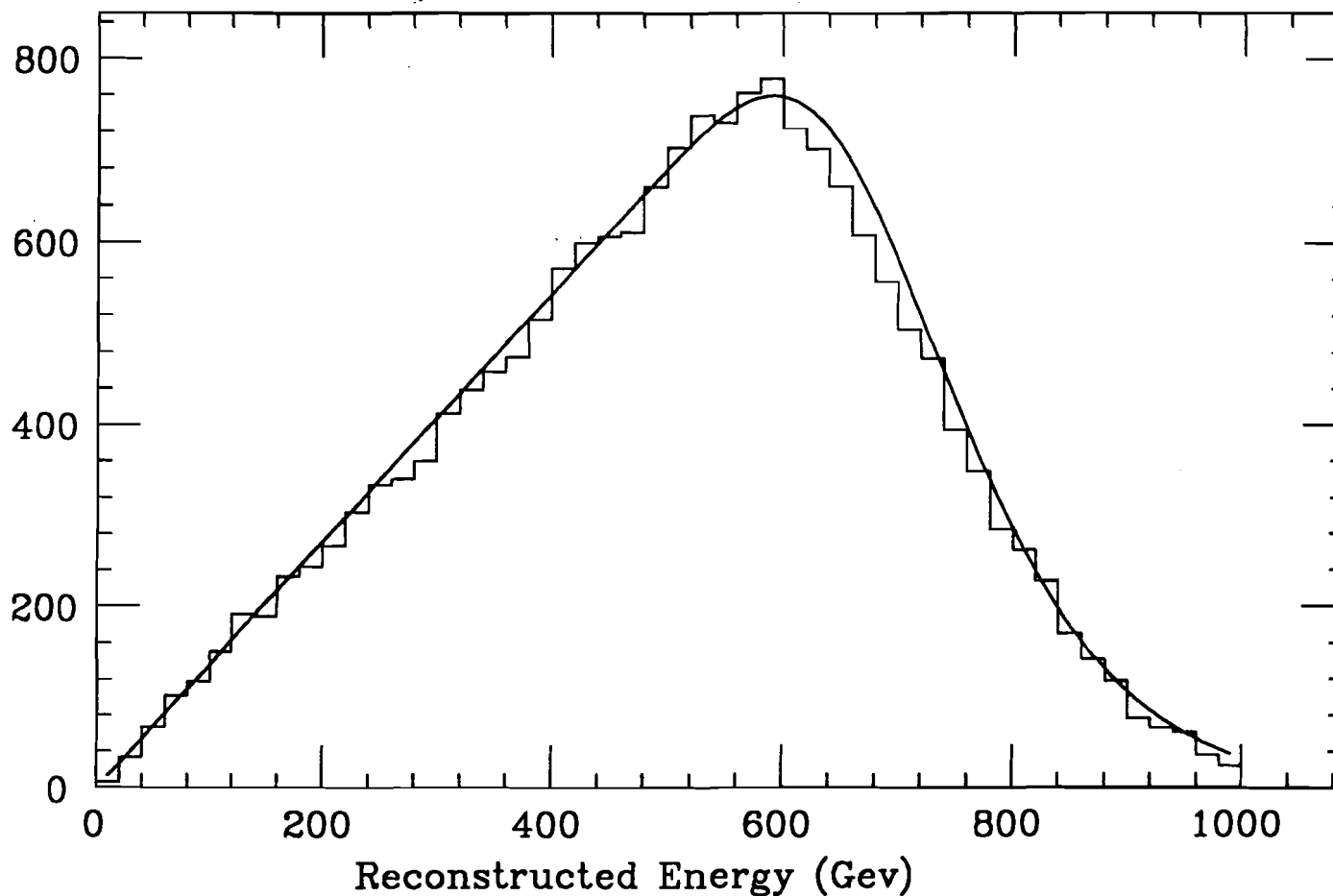
Peak Energy = 690 Gev, σ_E/E = 14%

Figure III.4:   Reconstructed Incident Neutron Spectrum

The histogram shows the spectrum of reconstructed event energy from data.

The curve is a ramped spectrum with a peak energy of 690 Gev convoluted with a 14% resolution.

Table III.1

Čerenkov Matrix

CY		OFF									ON									DON'T KNOW								
CB		OFF			ON			DON'T KNOW			OFF			ON			DON'T KNOW			OFF			ON			DON'T KNOW		
CO		OFF	ON	DK	OFF	ON	DK	OFF	ON	DK	OFF	ON	DK	OFF	ON	DK	OFF	ON	DK	OFF	ON	DK	OFF	ON	DK	OFF	ON	DK
0.0 Gev		πKP	?	πKP	?	?	?	πKP	?	πKP	?	?	?	?	e	e	?	e	e	πKP	?	πKP	?	e	e	?	e	?
2.93 Gev CO π		KP	π	πKP	?	?	?	KP	π	πKP	?	?	?	?	e	e	?	e	e	KP	π	πKP	?	e	e	KP	π	?
6.20 Gev CB π		KP	π	KP	π	π	π	KP	π	πKP	?	?	?	π	e	e	?	e	e	KP	π	KP	π	π	π	KP	π	?
10.36 Gev CO K		P	K	KP	π	π	π	P	πK	πKP	?	?	?	π	e	e	?	e	e	P	K	KP	π	π	π	P	πK	?
11.64 Gev CY π		P	K	KP	π	π	π	P	K	KP	π	π	π	π	π	π	π	π	π	P	K	KP	π	π	π	P	πK	?
19.68 Gev CO P		P	KP	KP	π	π	π	P	KP	KP	π	π	π	π	π	π	π	π	π	P	KP	KP	π	π	π	?	πKP	?
21.93 Gev CB K		P	P	P	πK	K	K	P	KP	P	π	π	π	πK	π	π	π	π	π	P	P	P	πK	πK	πK	?	πKP	?
41.16 Gev CY K		P	P	P	πK	K	K	P	P	P	πK	πK	πK	πK	πK	πK	πK	πK	πK	P	P	P	πK	πK	πK	?	πKP	?
41.70 Gev CB P		P	P	P	πKP	P	P	P	P	P	πK	πK	πK	πK	πK	πK	πK	πK	πK	P	P	P	πK	πK	πKP	?	πKP	?
78.24 Gev CY P																												

* all three counters do not agree

Table III.1:   Čerenkov Identification Matrix

The matrix shows the decision of the Čerenkov algorithms
based on a particle's momentum and the status of the three Čerenkov counters.

Chapter IV: Results

IV.A. Introduction

Because D^0 's live for less than a pico-second (less than 1.5 cm at 80 Gev), their presence must be deduced from their decay products. For this chapter, we look at the decay $D^{*+} \to D^0 \pi^+$, with the $D^0 \to K^- \pi^+$ (throughout this analysis, references to a particle state will imply the charge-conjugate state as well). Figure IV.1 shows mass plots of the D^* and the D^0 and the $D^* - D^0$ mass difference from the Physics Skim. As with most high-energy physics experiments, the signal is not observable in a raw mass plot. With the neutron beam of E400 and its subsequently large hadronic background (primarily pions), the high combinatoric background requires a number of cuts based on known physical properties of the interactions.

IV.B. Analysis Cuts

The basic cuts used in this analysis are as follows:

1) mass difference

2) lifetime

3) Čerenkov identification

4) distance of closest approach to the primary vertex

5) primary vertex in a target element.

Figure IV.2 shows the progression of the signal as these cuts are applied.

The mass-difference cut is a basic cut of all D^* searches. Figure IV.3 shows the energy levels of the D family. The decay D^{*+} to D^0 has a Q value of only 5.7 Mev. In calculating the quantity $D^* - D^0$, any measurement errors in the mass of the D^0 also appear in the mass of the D^* and thus cancel in the mass-difference. Hence the measurement of the pion from the decay of the D^* dominates the resolution of the $D^* - D^0$ mass-difference. This pion is generally a low-energy stub which is well measured in our spectrometer. Therefore, the mass-difference is well resolved and a cut on this value can be very tight (± 2 Mev in this analysis). Since the Q value is so low, the $D^* - D^0$ mass-difference appears just above threshold, at the low edge of a sharply rising combinatoric background. The large background rejection from the tight mass cut and

the relatively high signal to noise in the signal region can bee seen in comparing Figure IV.2.b with IV.2.a.

The signal begins to be developed after the application of a lifetime cut, explained in detail in Appendix C. The two important parameters from the lifetime algorithm are $\frac{L}{\sigma_L}$ and χ^2_*. χ^2_* is the χ^2 for the hypothesis that two tracks make up a secondary vertex. $\frac{L}{\sigma_L}$ is the detachment of this secondary D^0 vertex from the primary event vertex divided by the measurement resolution. As shown in Appendix C we expect a resolution, in proper time, of $\sigma_\tau = .18$ ps. Figure IV.2.c shows a very weak signal after the mass-difference and $\chi^2_* < 40$ cuts have been applied. The χ^2_* cut eliminates poorly-resolved and false combinations from this group of detached vertices. Figure IV.2.d finally shows some hint of a signal when we require that the $\frac{L}{\sigma_L}$ be greater than 6. This $\frac{L}{\sigma_L}$ cut requires that the secondary vertex be at least 6 standard deviations away from the primary vertex. At this point the signal is at most a two standard deviation effect as seen in Table IV.1.

As described in section III.A.3, the Physics Skim was done with the requirement that the K be identified by the Čerenkov algorithms. Applying the stronger requirement that the π's not be identified as K_{def}, K/P_{ambig}, or P_{def}, (or "heavies"), and further restrict the K to be identified as K_{def} or K/P_{ambig} under LOGIC, we get the result shown in Figure IV.2.e.

The fourth cut listed above required that the two tracks comprising the D^0 come to within .05" of the primary vertex. The fifth cut required that the primary vertex occurred within a target element (in z, refer to Figure II.5 for the position resolution possible in z). These two cuts further removed combinations made of poorly-resolved tracks or those that were clearly not associated with a D^* decay. These two cuts reveal a signal of about 3.3 standard deviations as seen in Figure IV.2.f and g and Table IV.1.

Figure IV.4 lends credibility to this signal by showing the development of the signal as the $\frac{L}{\sigma_L}$ requirement is increased from 0 to 10 (Figure IV.4.a has the $\chi^2_* > 40$ cut and all the other analysis cuts on it). While the significance of the signal starts to degrade above $\frac{L}{\sigma_L} > 6$, the ratio of the signal to background continues to increase. All of this is quantified in Table IV.A.2.

Finally, Figures IV.5 and IV.6 show cut- and lifetime-development plots respectively for the mass-difference. The shape of the background was fixed to conform to the shape found from plots of the D^0 sidebands, 1.72 - 1.80 and 1.94 - 2.02 Gev. The normalization was adjusted so that the curve passed through the average of the bins between .15 and .155 Mev. The fit gives a mean for the $D^* - D^0$ mass-difference at 143.2 Mev with a standard deviation of 1.35 Mev for Figure IV.5.g. There are 14.4 ± 8.5 events in the peak which is statistically consistent with the number found in the D^0 plot but is lower. The fact that the peak is so close to threshold and the cut-off of the data at 160 Mev makes it difficult to set the level of the background.

IV.C. Acceptance

In order to obtain a cross-section for hadronic D^* production, it is necessary to measure the luminosity, compute the acceptance of the spectrometer, and compute the efficiency of the analysis cuts used to uncover the D^* signal. These acceptance calculations were made with the Monte Carlo program described in section III.E. The simplest method for correcting the raw event yield for the acceptance would be to divide the total observed yield by one average acceptance value. This acceptance could be obtained by dividing the number of accepted Monte Carlo events by the number of generated Monte Carlo events, which were generated according to a specified production model (such as gluon-gluon fusion). The problem with this simple approach is that the acceptance in typical fixed target experiments such as E400 is generally a strong function of the momentum of the state being considered. If the assumed production model was, in fact, incorrect and the generated charm particles did not have the momentum distribution of charm particles produced in nature, the average acceptance value may be vastly different from the true value. The model dependence of a single average acceptance is particularly acute for the signal considered here. As described in Chapter I (Figure I.3), the differential cross-section ($\frac{d\sigma}{dx_F}(\bar{x}_F)$) for charm hadroproduction is expected to exhibit a relatively sharp peak near $x_F = 0$ which is the very region where the E400 acceptance undergoes rapid variation (falling rapidly as $x_F \rightarrow 0$). Since the D^* signal shown in Figure IV.2.g has such limited statistics, we would always lack the data to confirm whether or not $\frac{d\sigma}{dx_F}(\bar{x}_F)$ varies in x_F, near $x_F = 0$, in the same way that was assumed in the Monte Carlo. Thus systematic errors would be huge.

Rather than rely on an acceptance obtained from a specific Monte Carlo model, we chose to parameterize the acceptance as a function of kinematic properties of the D^*. Care went into both the parameterization of this acceptance as well as in the choice of analysis cuts employed in order to try to eliminate as much model uncertainty as possible. We then used a weighting technique to extract a background-subtracted, efficiency-corrected event yield. D^* candidates which passed the cuts described in section IV.B incremented a histogram with a weight proportional to the reciprocal of the parameterized acceptance. The resulting weighted histogram (with errors reflecting both the Poisson statistics on the number of entries as well as weight fluctuations within a given bin) was then fit to a Gaussian signal over a smoothly parameterized background. The area under this Gaussian signal peak in the acceptance-weighted histogram provided our acceptance-corrected, background-subtracted estimate of the yield. Multiplication by the luminosity factors discussed in section IV.C.2. and Appendix B converted this corrected yield to an actual partial cross-section.

IV.C.1. Acceptance Parameterization

The principle issue in the parameterization of the acceptance involves deciding which variables to explicitly include in the parameterization and which variables to average over. It is clearly reasonable to average over variables with known distributions such as the decay angles describing the isotropic decays, $D^{*+} \rightarrow (K^- \pi^+) \pi^+$. One can quite sensibly average over variables that only weakly affect the acceptance of the state. Monte Carlo simulations show a very mild dependence of the overall acceptance on the $P_\perp$ of the D^* except at unreasonably large $P_\perp$ ($P_\perp > 3$ GeV for example). Often the various acceptance factors are correlated in a manner to reduce model dependence and thus permit more variables to be safely averaged over.

For example, in E400 if one detects all the decay products of a $D^{*+} \rightarrow (K^- \pi^+) \pi^+$ decay, the probability of satisfying the minimum-multiplicity buslines described in section II.D.1.c is quite high. Little room is left for significant variation in the acceptance, thus the total generated-event multiplicity can be safely averaged. One can say in this instance that the $(K^- \pi^+) \pi^+$ final state is highly "self-triggering" as regards to the multiplicity busline.

The self-triggering essentially eliminates all variables from the acceptance parameterization but the lab energy of the D^* , the total event energy (owing to Busline 7), and the heavy-particle content of the entire event (owing to the M7, heavy-particle trigger).

We have chosen to parameterize the D^* acceptance into two basic factors. One factor describes the efficiency of the M7 trigger as a function of the number of heavy particles observed in the event. The other factor includes all other acceptance contributions such as the geometrical acceptance of the spectrometer, the efficiency of all analysis cuts, and the energy and multiplicity requirements of the experimental trigger. We have parameterized this factor in terms of the observed energy of a D^* , or alternatively in terms of the measured x_F of the D^* , which is deduced from the D^* energy and the reconstructed event energy (see Equation IV.2). We begin with a discussion of the M7 factor.

An efficiency correction for the M7 is required since our Monte Carlo studies indicate that the $(K^- \pi^+) \pi^+$ final state typically triggers the M7 about 60 % of the time. Thus despite the fact that the final state discussed here includes a kaon and the M7 trigger is designed to trigger on kaons, the $(K^- \pi^+) \pi^+$ final state is not really self-triggering. We believe this M7 inefficiency reflects the fact that the trigger only involves CB and CY and is thus only sensitive to kaons above 22 GeV, and that the momentum cut used by the M7 processor in order to reject subthreshold pions is based only on information from the crudely segmented TRM bands. Hence the momentum information used in the trigger has much poorer resolution than that available from the full analysis and the necessarily crude trigger-tracking algorithms of the M7 can be easily confused in high-multiplicity events. We have chosen to study the efficiency of the M7 on unbiased data events as a function of the of the number of heavy particles observed using the much more efficient complete off-line analysis. The M7 parameterization function is described in Appendix B and compared to unbiased data in Figure B.2. The M7 correction was made by using the observed total heavy-particle content of events containing a D^* candidate as an input to the parameterized M7 efficiency. The M7 efficiency was then multiplied by the x_F- or E_{D^*}-dependent efficiency to obtain a net efficiency for the purpose of constructing the acceptance-weighted histogram.

We believe that the largest source of residual model dependence is involved with the interplay between acceptance factors which depend nearly exclusively on the D^* energy, and those factors which depend on the energy of the beam neutron. The factors that depend nearly entirely on the D^* energy (once the D^* decay angles and $P_\perp$ are averaged over) include the geometrical acceptance, the Čerenkov identification efficiency, the mass and mass-difference, and lifetime cuts. If the acceptance is parameterized as a function of E_{D^*}, the effect of these requirements will be properly modeled independent of the production model assumed in generating these efficiencies.

Unfortunately, Busline 7, which requires a minimum-transverse-energy deposition of roughly 265 GeV, brings in a dependance on the energy of the incident neutron as well. One immediate consequence of the Busline 7 requirement will be that the over-all acceptance will depend on the assumed s dependence of the D^* inclusive cross-section used in the Monte Carlo since we averaged over the neutron spectrum in parameterizing our acceptance. As indicated in Chapter I, the s dependence of the hadronic-charm cross-section is a matter of considerable experimental controversy. One can argue that once the Busline 7 requirement is applied, the resulting accepted neutron spectrum is characterized as having a most probable energy of 640 GeV with an RMS spread of $\pm$ 20% . It is difficult to imagine the s dependence of the hadronic-charm cross-section changing appreciably over a 20% range in neutron energy. Our Monte Carlo calculations were performed assuming a total cross-section which is independent of s over the range of our triggerable neutron spectrum.

The interplay between the E_{D^*}- and s-dependant efficiency factors gives rise to a more subtle and insidious source of model dependence for the acceptance. Consider the problem of determining the Busline 7 efficiency for a D^* produced with a relatively large lab energy (Say an energy corresponding to x_F of approximately .2). Let us assume that the Monte Carlo produces D^* 's according to distributions of the form:

$$\frac{d\sigma}{dx_F}(\bar{x}_F) \propto (1 - |x|)^N .$$

(IV.1)

Different models are thus differentiated on the basis of different N values. As one increases the softness of the x_F distribution (by raising the value of N), the D* 's of a given lab energy will by necessity be produced by large s neutrons which have a large efficiency for firing the energy busline (Busline 7). Conversely, as N → 0 the cross-section becomes nearly independent of x_F, and relatively soft neutrons can readily produce a D* at the given fixed energy. Thus the average Busline 7 efficiency will be lower as N → 0 . Our Monte Carlo simulations indicate a roughly ± 20 % variation in the Busline 7 efficiency as N is varied from 1 to 8 owing to this interplay effect.

In order to insure that the model dependance described above really is minimal, we check the consistency of our results with an independent acceptance parameterization based on the x_F of the D* which is computed from the measured D* energy as well as the total event energy derived from calorimetry according to the algorithm described in section III.D. If the assumptions about the x_F and s dependence of the cross-section inherent to the production model chosen for the Monte Carlo do not reasonably match nature's "production model", then events with a measured x_F would have a D* energy different than the D* energy assumed in determining the acceptance. Therefore, cross-sections determined by weights based on the x_F of each event will not agree with cross-sections based on the energy of the D* .

To couple the two weighting schemes, the correlation between the x_F, E_{D*}, and the neutron energy must be determined. Figure IV.7 shows a plot, based on Monte Carlo events, of the x_F of the D* versus the energy of the D* . Also shown in the plot are curves for various effective neutron energies that relate the state energy with x_F according to the relation:

$$ x_F = \frac{E_{D*}}{E_{neutron}^{eff}} - \frac{M_\perp^2}{2 \times M_{neutron} \times E_{D*}} \tag{IV.2} $$

where $M_\perp^2 = M_{D*}^2 + P_\perp^2$ and $P_\perp$ is .75 Gev. The plotted points do not match the curves exactly because of the very features that have been discussed, the finite width of the neutron spectrum and the response of Busline 7, but choosing an effective neutron energy of 600 Gev appears to agree to within 50 Gev over the range $50 < E_{D*} < 200$ Gev, which is our area of interest.

We now have the bridge, between the energy of the D^* and the x_F, through which we can compare the cross-sections determined by the two methods. The x_F of each event can be determined in order to calculate its acceptance and the energy limits, E_{low} and E_{high}, corresponding to the limits of reasonable acceptance in x_F, x_{Flow} and x_{Fhigh}, can be calculated. If the production model in the Monte Carlo is incorrect, the acceptance for each event under the energy and x_F schemes will not match nor will the sampled ranges of energy and x_F. Therefore, if the cross-sections from each method agree then we have reasonable confidence that the production model is a good representation of reality.

IV.C.2. Application of Acceptance Parameterization

To calculate the number of events passing all trigger, acceptance, and analysis cuts, the number of accepted events was divided by the number generated in separate bins of x_F and energy to provide the acceptance plots shown in Figure IV.8. These acceptances were parameterized by the following form:

$$\frac{A}{2\sqrt{2\pi}} e^{-\frac{1}{2}\left(\frac{(x-x_0)}{\sigma}\right)^2} \quad \text{for } x < x_0 \tag{IV.3}$$

$$\frac{A}{2\sqrt{2\pi}} e^{-\frac{1}{2}\left(\frac{(x-x_0)}{\sigma}\right)^2} (1 - e^{-B(x-x_0)}) + e^{-B(x-x_0)}(A + C(x - x_0)) \quad \text{for } x > x_0 \tag{IV.4}$$

where x_0, σ, A, B, and C are determined by a fitter and x is either E_{D^*} or x_F. The mass plots were then produced again with each entry weighted by the inverse of its acceptance.

The mass plots weighted by the above acceptances (designated ϵ_{MC} in equation IV.5 below and Appendix B) should give the number of D^* 's and background events produced in the absence of acceptance effects. These mass distributions were then fit to a Gaussian over a polynomial background to get an actual yield of charm signal events. The resulting yields can be combined with luminosity effects to produce a partial cross-section times the branching ratio, $\Delta\sigma \cdot Br$, over a specific x_F range. The luminosity factors (described in detail in Appendix B) include:

$$\Delta\sigma_{ch} \cdot Br = \frac{1}{2} \frac{\sigma_{eff} \cdot Y_{ch} \cdot \epsilon_{MG}}{Y_{MG} \cdot \epsilon_{lt} \cdot \epsilon_{M7} \cdot \epsilon_{MC} \cdot \epsilon_{Si33} \cdot \epsilon_{ns}} \tag{IV.5}$$

where:

- Br is the branching ratio of the $D^{*+} \to D^0 \pi^+$ (.49) times the branching ratio of $D^0 \to K^- \pi^+$ (.042)

- $\frac{1}{2}$ averages the particle and anti-particle cross-section.

- σ_{eff} is an effective inelastic cross-section (13500 μbarns) that reflects the elemental composition of the experimental target

- Y_{ch} is the number of observed charm events

- ϵ_{MG} is the Master Gate efficiency (.85)

- Y_{MG} is the yield of inelastic events that fired the trigger (2.0368×10^8)

- ϵ_{lt} is the livetime of the data aquisition system (.41233)

- ϵ_{M7} is the M7 efficiency, applied on an event-by-event basis

- ϵ_{MC} is the geometric and analysis efficiency as determined by the Monte Carlo, also applied on an event-by-event basis

- ϵ_{Si33} is the Si33 busline efficiency (.654)

- ϵ_{ns} is the fraction of the neutron spectrum that was triggered on in Busline 7 (.82).

Figure IV.9 shows the histogram in Figure IV.2.g weighted by the two methods. The energy weighting gives $\Delta\sigma \cdot$ Br of 2.57 $\pm$ 0.76 μbarns/Nucleon and the x_F weighting gives 2.14 $\pm$ 0.68, so the agreement is within one standard deviation. The consistency between these two $\Delta\sigma \cdot$ Br determinations supports our assumptions concerning the s and x_F dependence of the charm hadronic cross-section.

A check can be done by removing the Čerenkov requirement on the kaon. (see Figure IV.10 for the severe restrictions on the acceptance when Čerenkov cuts are applied.) Figure IV.11 shows the raw histogram and the x_F weighted one. The $\Delta\sigma \cdot$ Br for this sample is 2.13 $\pm$ 1.14 which again agrees well with the other results.

IV.D. Cross-Section

Because E400 had a limited acceptance range in x_F, we prefer to express our results as a differential cross section $\frac{d\sigma}{dx_F}(\bar{x}_F)$, where $\bar{x}_F$ is in the middle of the acceptance range. The state $D^{*+} \to (K^- \pi^+) \pi^+$ could be detected with reasonable acceptance over the range $-.02 < x_F < .3$ or $33 < P_{D^*} < 195$. The simplest way to convert $\Delta\sigma \cdot Br$ to $\frac{d\sigma}{dx_F}(\bar{x}_F)$ would be to divide $\Delta\sigma \cdot Br$ by Δx_F. However, the x_F range is sufficiently large that the curvature implied by the form $\frac{d\sigma}{dx_F}(\bar{x}_F) \propto (1 - |\bar{x}_F|)^N$ would introduce substantial errors for expected values of N. Therefore we have adopted the following method based on this parameterization. The form:

$$\frac{d\sigma}{dx_F}(\bar{x}_F) = \sigma_{\text{Tot}}\left(\frac{N+1}{2}\right)(1 - |\bar{x}|)^N \qquad \text{(IV.6)}$$

implies a partial cross section:

$$\Delta\sigma(x_1 \to x_2) = \left(\frac{\sigma_{\text{Tot}}}{2}\right)\left[\text{Sgn}(x_2)(1 - (1 - |\bar{x}_2|)^{N+1}) - \text{Sgn}(x_1)(1 - (1 - |\bar{x}_1|)^{N+1})\right]. \qquad \text{(IV.7)}$$

The measured cross-section can be used to evaluate σ_{Tot} using Equation IV.7. σ_{Tot} can be used in Equation IV.6 to give $\frac{d\sigma}{dx_F}(\bar{x}_F)$ over any x_F range. The result is fairly insensitive to the choice of N as long as $\bar{x}_F$ lies close to the mean of x_{F1} and x_{F2}. For the values shown in Table IV.3, N = 4 was assumed.

The x_F range can be restricted to $0. < x_F < .14$ to compare with the results of $D^* \to (K^+ K^-) \pi$ [31,34]. Table IV.3 shows the results for $D^{*+} \to (K^- \pi^+) \pi^+$ for both the energy and x_F weighting with and without the Čerenkov identification. The agreement among these values is quite good. The entries that follow are the results for $D^* \to (K^+ K^-) \pi$, as determined by another researcher[31,34]. These $K^+ K^-$ values are a bit higher, but are only about one standard deviation away and should be considered consistent. At the bottom of the table are values for $D^{*+} \to (K^- \pi^+) \pi^+$ over the full range $-.02 < x_F < .3$. The differential cross-section, $\frac{d\sigma}{dx_F}(\bar{x}_F = .14)$, is smaller relative to $\frac{d\sigma}{dx_F}(\bar{x}_F = .07)$ by a factor of 2, consistent with N = 6 or 7 in Equation IV.6.

Another check on the consistency of the data can be performed as shown in Table IV.4. Various ranges in x_F were looked at while maintaining $\bar{x}_F$ for the two ranges used above, .07 and .14. The stability of $\frac{d\sigma}{dx_F}(\bar{x}_F)$ as the range is varied shows remarkable consistency.

IV.E. Systematic Errors

Table IV.5 shows $\frac{d\sigma}{dx_F}(\bar{x}_F = .14)$ for several lifetime cuts from up to $\frac{L}{\sigma_L} > 10$. The corrected cross-sections rise as the minimum $\frac{L}{\sigma_L}$ is increased, which indicates that there may be a systematic error in the lifetime algorithm. Two possible contributions to this rise are uncertainties in the lifetime of the D^0 and the transverse position resolution (Appendix D). In the Monte Carlo, a lifetime of .434 psec was used. While the Tagged Photon Group claims to have measured the lifetime to 2 % (.422 ± .008 psec)[12], a more recent ARGUS measurement differs by almost 14 % (.48 ± .04 psec)[35]. Monte Carlo studies show that a 1 % difference in the lifetime produces a 3 % difference in the cross-section at $\frac{L}{\sigma_L} > 6$ (and 5% at $\frac{L}{\sigma_L} > 10$). A 15 % change in the transverse position resolution (which is a reasonable uncertainty for this experiment) results in a 30 % change in the cross-section at $\frac{L}{\sigma_L} > 6$ (and 60% at $\frac{L}{\sigma_L} > 10$).

Other systematic errors in the above calculations reflect uncertainties in the efficiency of the energy busline, the signal rejection of the Δ M cut, and the Master Gate efficiency. Monte Carlo studies show that the efficiency of the energy busline varies by as much as ± 20%, depending on the x_F spectrum used in producing D^* 's. As discussed in Appendix B, the efficiency of the Master Gate is known to approximately ± 20%. We estimate that the tight (± 2 Mev) mass-difference cut introduces another ± 30% uncertainty in the cross-section. Both the Monte Carlo simulation and the data of Figure IV.5.g. suggest a D^* - D^0 mass-difference resolution of 1.35 Mev. We would thus expect roughly 10% of legitimate D^* events to lie outside the ± 2 Mev mass-difference cut employed in this thesis. To make matters worse the mass-difference range use, 142 - 146 Mev, is roughly 1.5 Mev lower than the world average for the D^* - D^0 mass-difference of 145.5[11]. A 1.5 Mev mis-centered mass-difference cut would cause 40% of the D^* 's to miss the cut used in this thesis. Section V.B describes a mechanism whereby the mass scale of the experiment could be off by 1.5 Mev so the cut would actually be centered for the data. In this case the true efficiency of the mass-difference cut would be larger than that assumed in the Monte Carlo by approximately 30%. Adding the results of these four systematic errors in quadrature gives an estimated systematic error of ± 50%. To conclude, averaging the results of the two weighting methods in section IV.C.3, we get $\Delta\sigma \cdot$ Br = 2.36 ± .72 (statistical) ± 1.18 (systematic) μbarns/Nucleon over the range $-.02 < x_F < .3$.

Edit Cuts Only

(a)

(b)

(c)
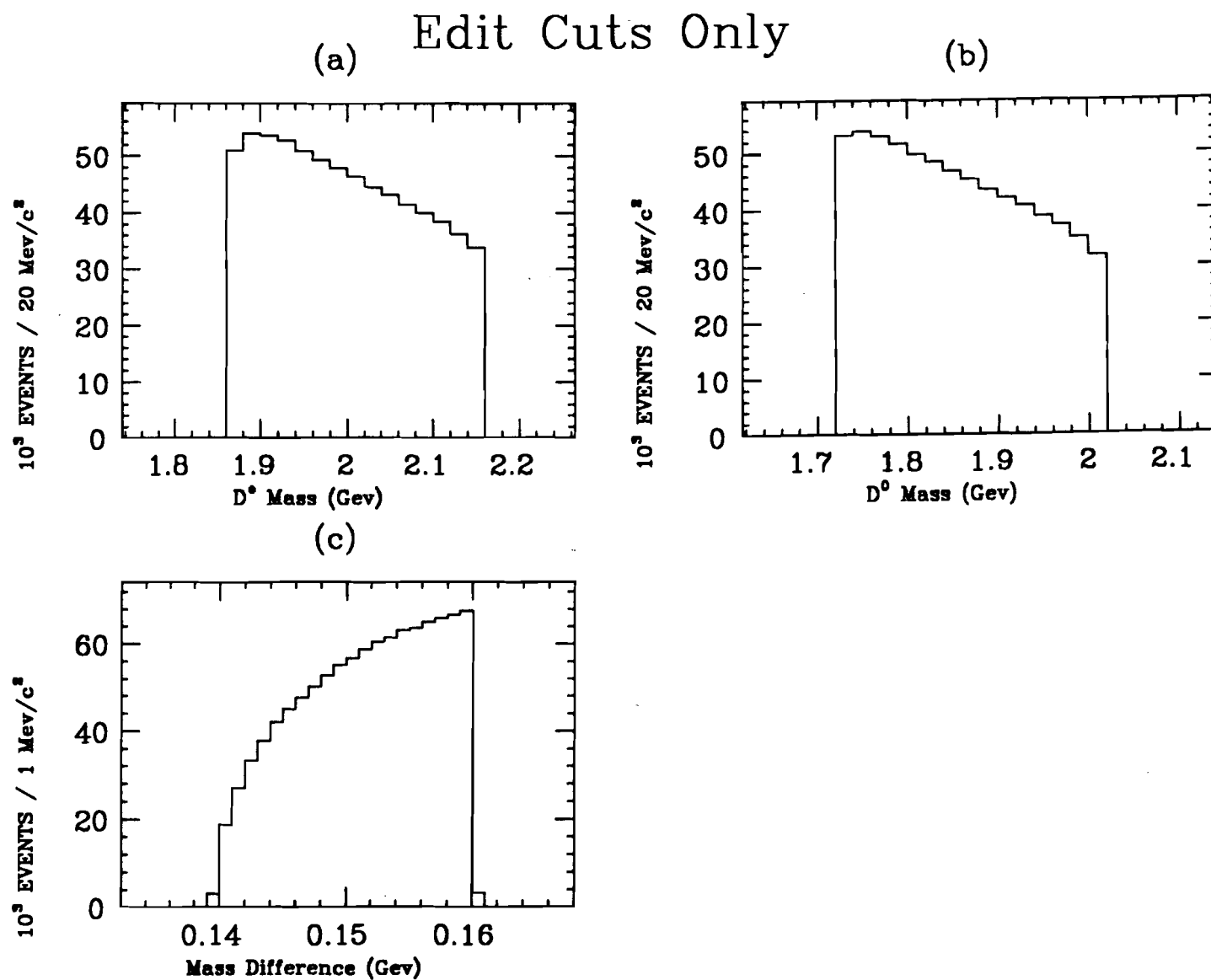
Figure IV.1:   D* , D⁰ , Δ M Mass Plots, Edit Cuts Only

Figure IV.2: D° Mass, Cut Progression

The curve is the result of a fit to a Gaussian over a linear background.

Figure IV.3:   Energy Level Diagram, D Family

(a) All but L/σ_L

(b) $L/\sigma_L > 0$

(c) $L/\sigma_L > 2$

(d) $L/\sigma_L > 4$

(e) $L/\sigma_L > 6$

(f) $L/\sigma_L > 8$

(g) $L/\sigma_L > 10$

Cuts

Mass Difference $= 142 - 146$ Mev/c^2

Cerenkov $=$ Restricted K/P, π's not heavy

$\chi^* < 40$

DCA to Primary Vertex $< .05''$

Primary Vertex in a Target Element
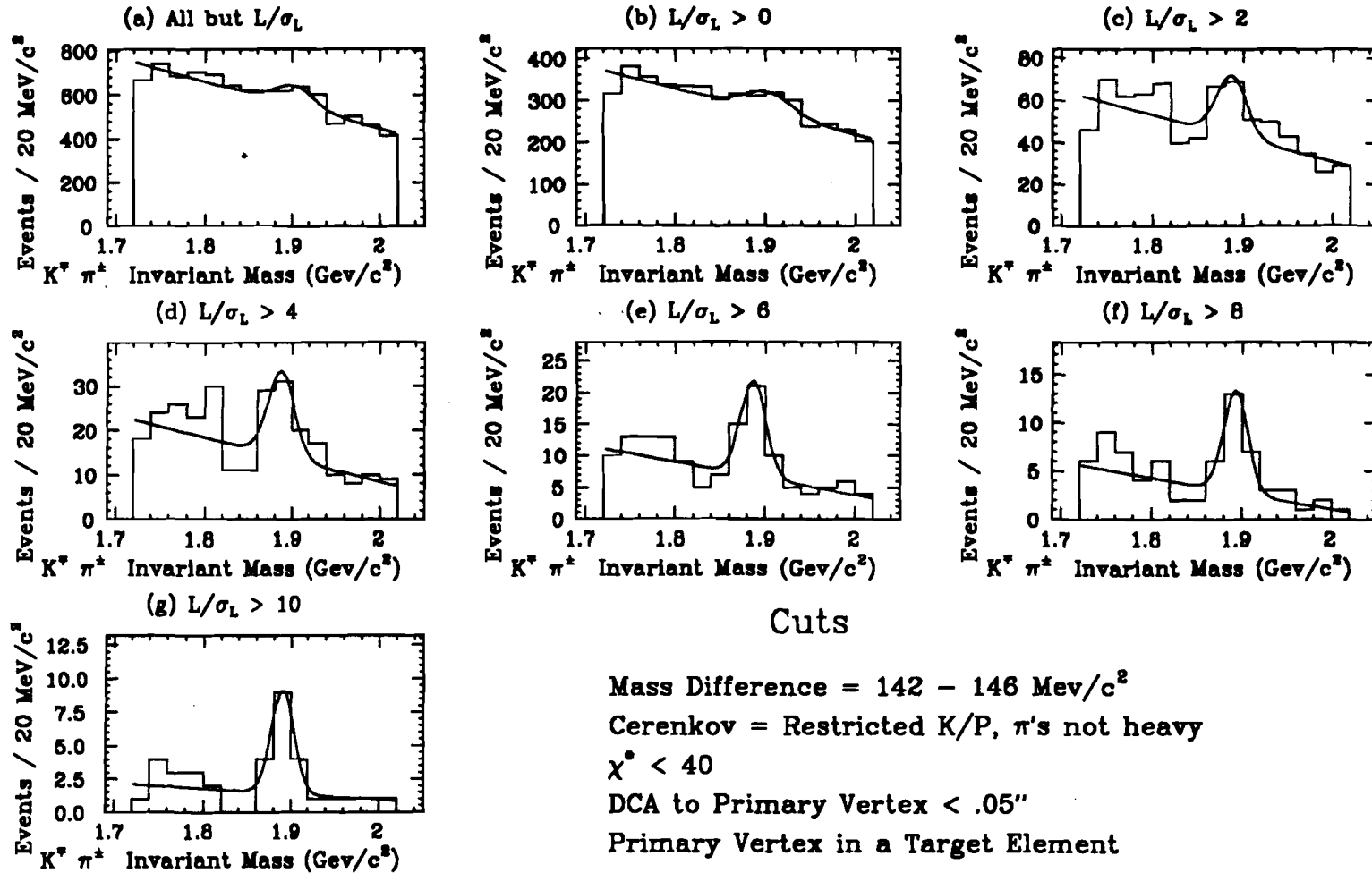
Figure IV.4: D^0 Mass, Lifetime progression

The curve is the result of a fit to a Gaussian over a linear background.

(a) Edit Cuts only

(b) D^0 Mass 1.85 – 1.93 Gev/c²

(c) $\chi^0 < 40$

(d) $L/\sigma_L > 6$

(e) Cerenkov

(f) DCA

(g) Primary Vertex in Target

Edit Cuts

Cerenkov = K/P under either algorithm
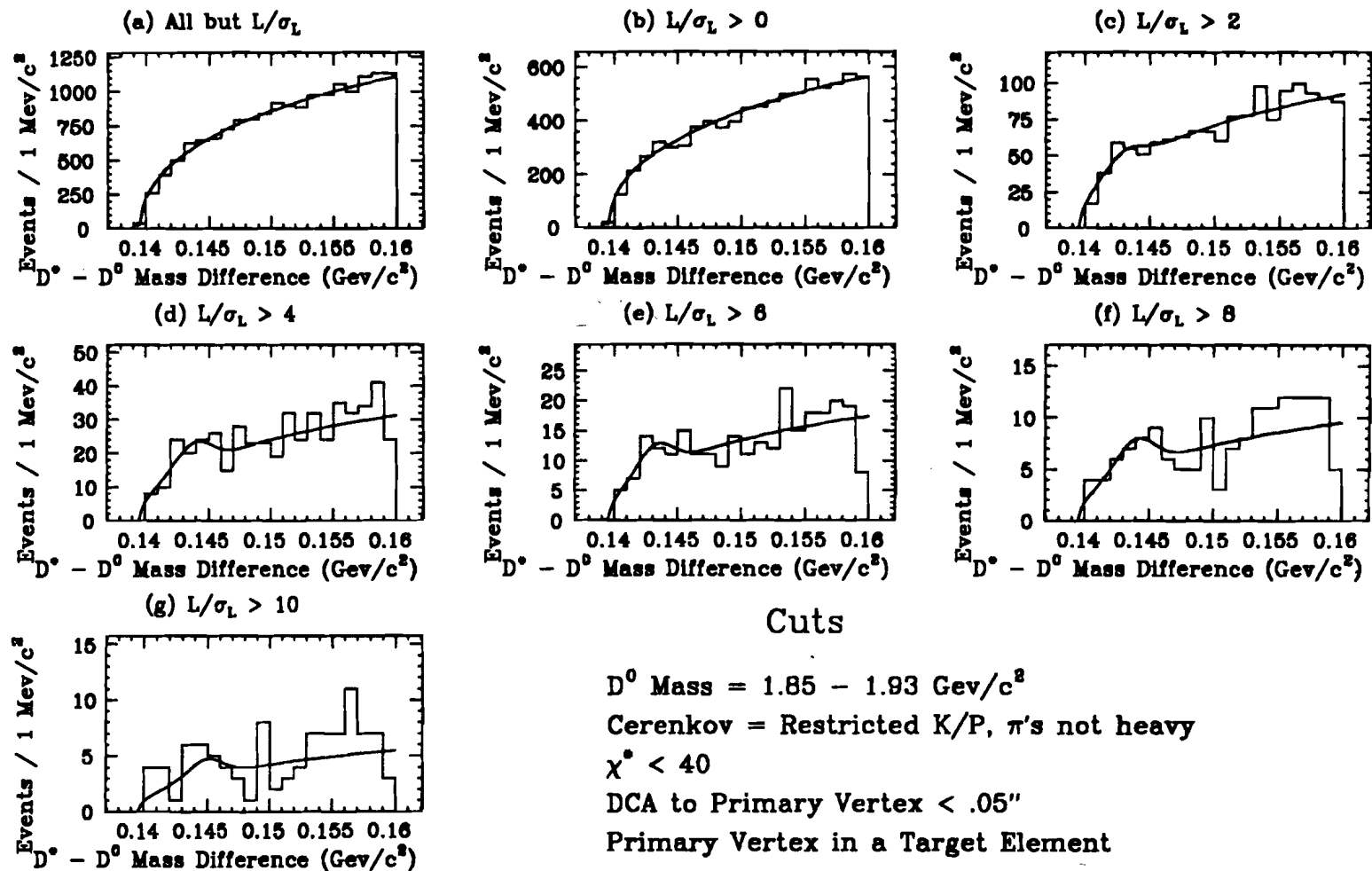
Mass Difference < 165 Mev/c²

D^0 Mass ± 150 Mev/c²

Figure IV.5: D^* - D^0 Mass-Difference, Cut Progression

The curve is the result of a fit to a Gaussian over a threshold background determined from D^0 sidebands.

(a) All but L/σ_L

(b) $L/\sigma_L > 0$

(c) $L/\sigma_L > 2$

Events / 1 Mev/c²

$D^* - D^0$ Mass Difference (Gev/c²)

(d) $L/\sigma_L > 4$

(e) $L/\sigma_L > 6$

(f) $L/\sigma_L > 8$

(g) $L/\sigma_L > 10$

Cuts

D^0 Mass $= 1.85 - 1.93$ Gev/c²

Cerenkov $=$ Restricted K/P, π's not heavy

$\chi^* < 40$

DCA to Primary Vertex $< .05''$

Primary Vertex in a Target Element

Figure IV.6: $D^* - D^0$ Mass-Difference, Lifetime Progression

The curve is the result of a fit to a Gaussian over a threshold background determined from D^0 sidebands.

Effective Neutron Energy

$E_n = 400$ Gev
$E_n = 500$ Gev
$E_n = 600$ Gev
$E_n = 700$ Gev
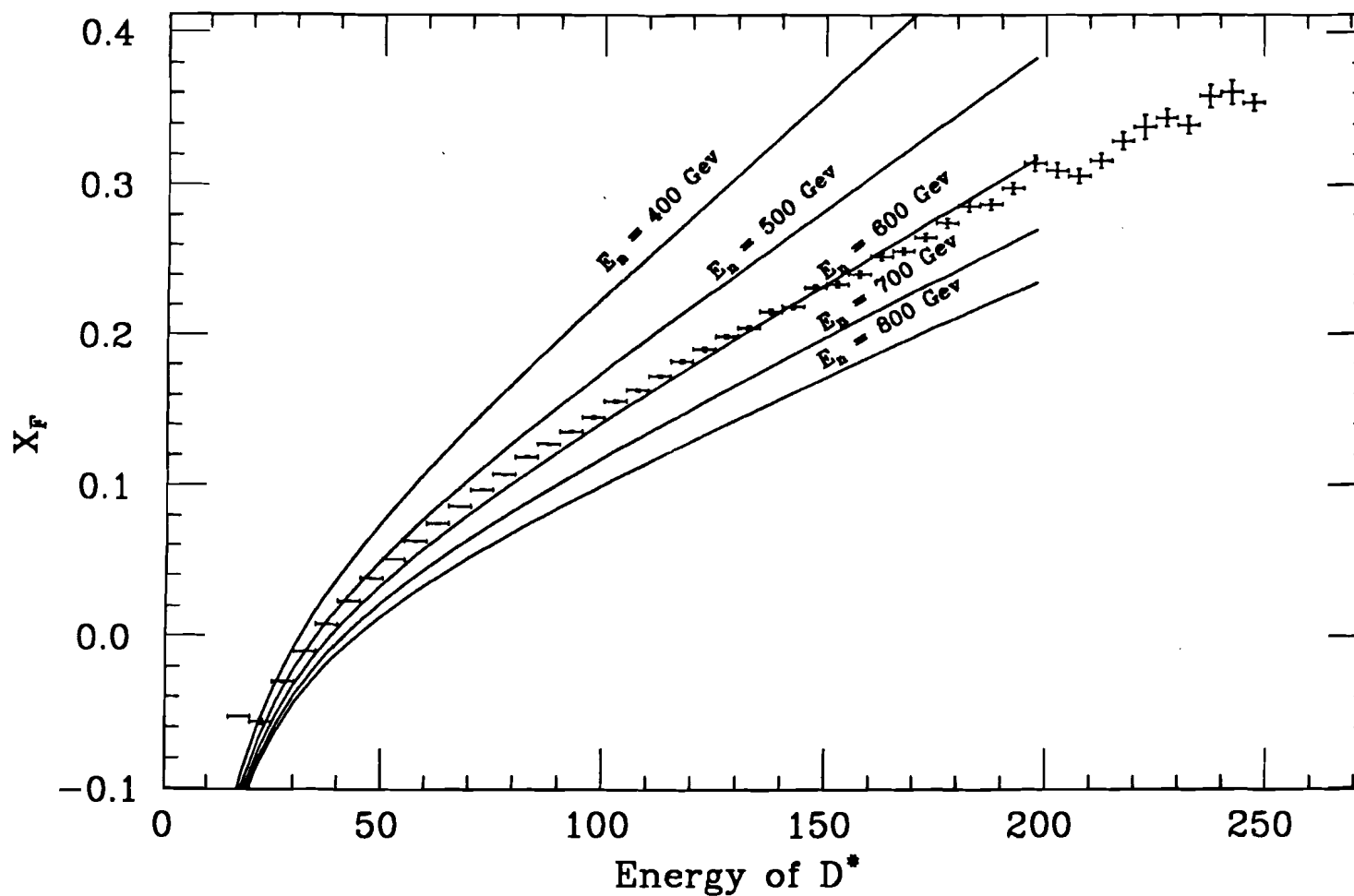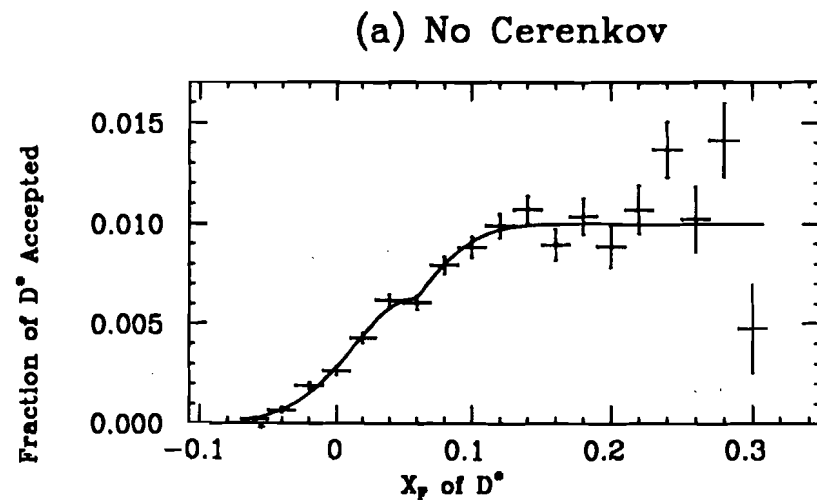$E_n = 800$ Gev

X_F

Energy of D^*

Figure IV.7:   Effective Neutron Energy

The plotted points are Monte Carlo data.

The curves are the results of Equation IV.2 with various "effective" neutron energies.

(a) No Cerenkov

Cuts

Mass Difference = 142 − 146 Mev/c^2

$\chi^* < 40$

$L/\sigma_L > 6$

DCA to Primary Vertex < .05"

Primary Vertex in a Target Element

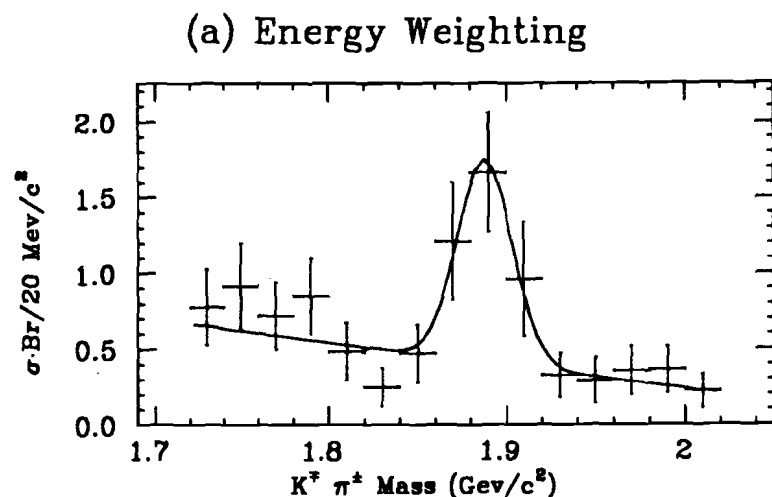## (b) All Cuts

Cuts

Mass Difference = 142 − 146 Mev/c^2

Cerenkov = Restricted K/P, π's not heavy

$\chi^* < 40$

$L/\sigma_L > 6$
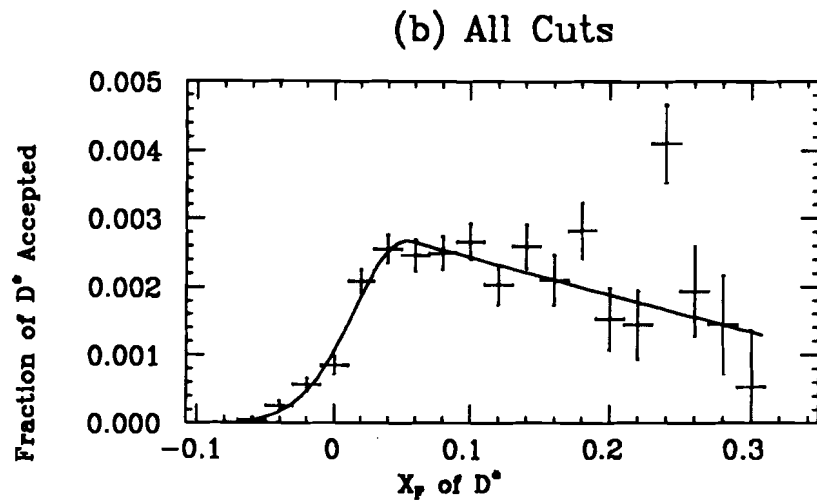
DCA to Primary Vertex < .05"

Primary Vertex in a Target Element

Figure IV.8: Acceptance Curves

The plotted points are the acceptance determined from the Monte Carlo in bins of Feynman X.
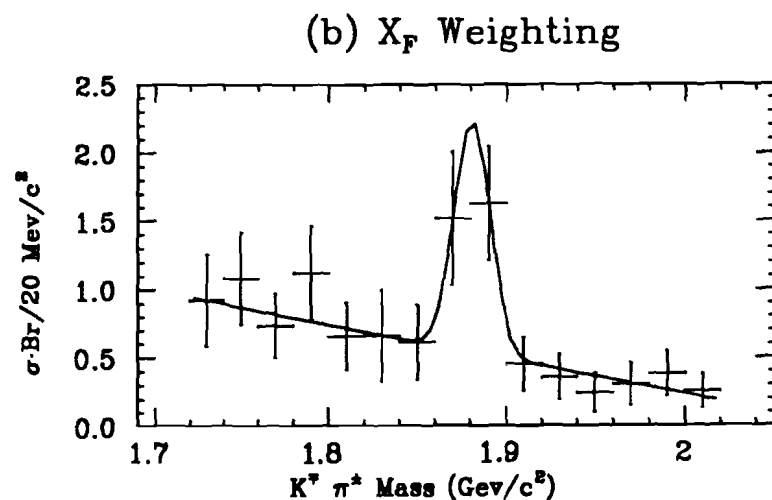
The curves are the results of fits to Equations IV.3 and IV.4.

(a) Energy Weighting

$\sigma \cdot Br = 2.57 \pm 0.76 \ \mu barns/Nucleon$

Cuts

Mass Difference = 142 − 146 Mev/c^2

Cerenkov = Restricted K/P, π's not heavy

$\chi^* < 40$

$L/\sigma_L > 6$

DCA to Primary Vertex < .05″

Primary Vertex in a Target Element

$-.02 < X_F < .3$

(b) X_F Weighting

$\sigma \cdot Br = 2.14 \pm 0.68 \ \mu barns/Nucleon$

Figure IV.9: $\sigma \cdot Br$, Energy and x_F Weighting

The plotted points are the yield of Figure IV.2.g weighted by IV.5.

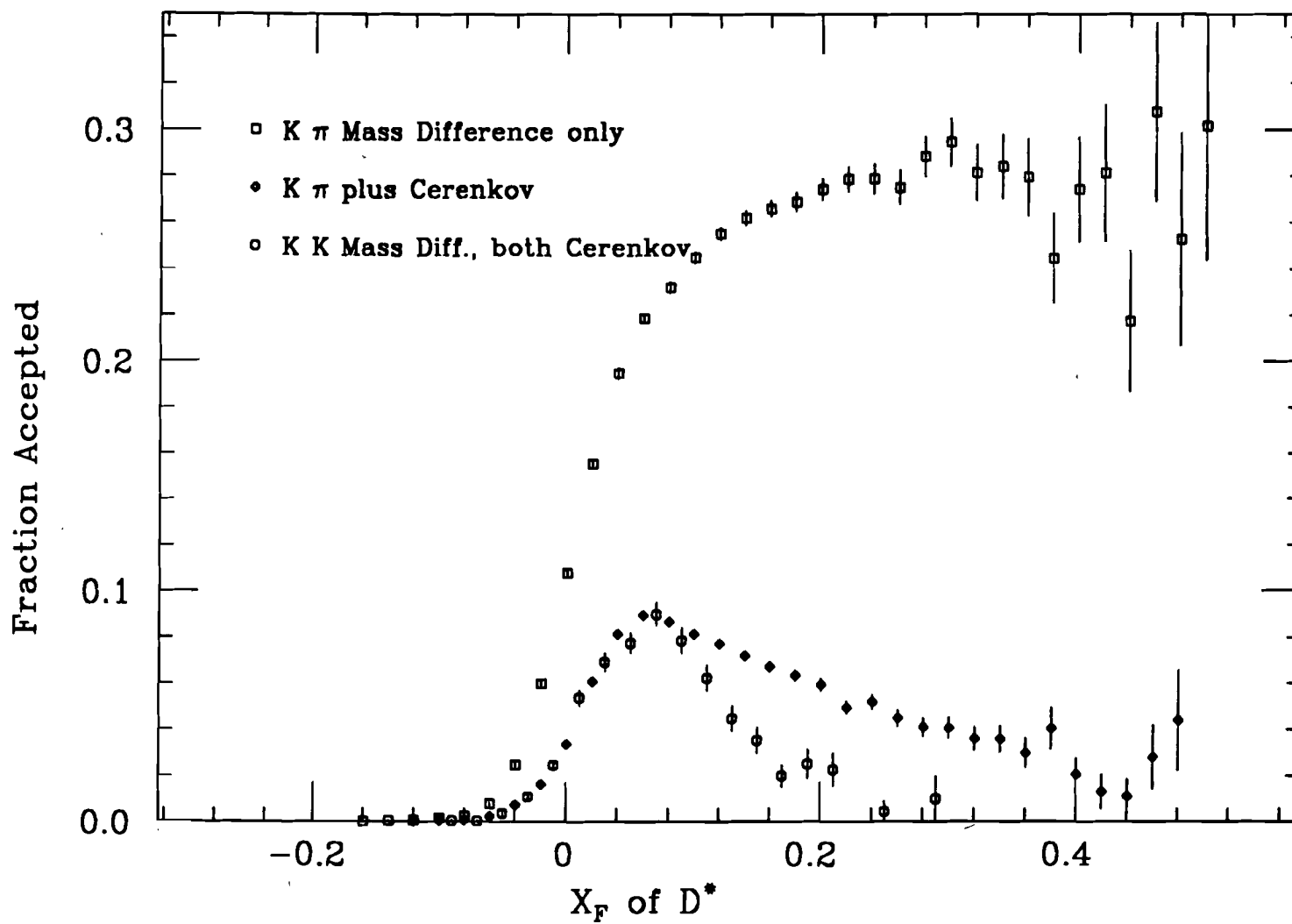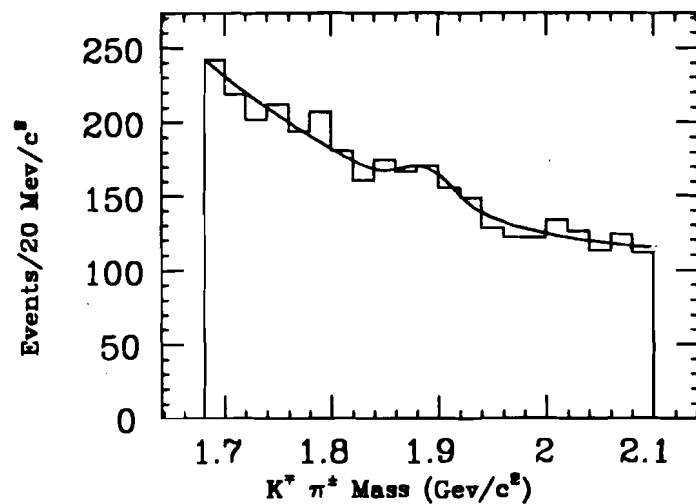The curve is the result of a fit to a Gaussian over a linear background.

Figure IV.10:   Acceptance Curve, Various Cuts

The plotted points are the acceptance determined from the Monte Carlo in bins of Feynman X.

(a) No Cerenkov, $-.02 < X_F < .3$

(b)
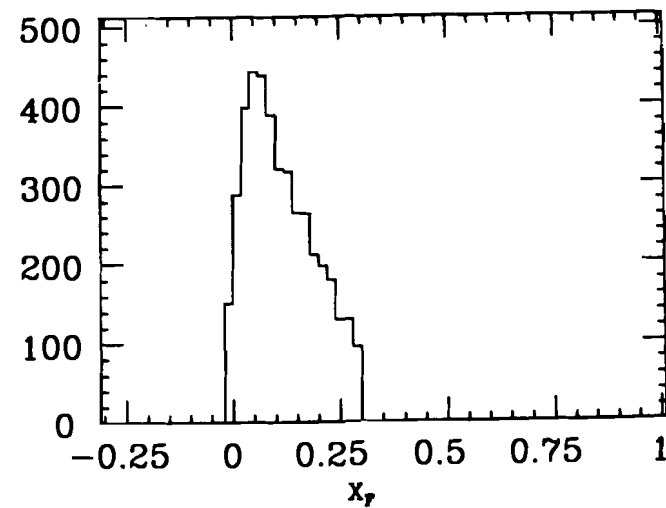
(c) $\sigma \cdot Br$, No Cerenkov, $-.02 < X_F < .3$ Cuts
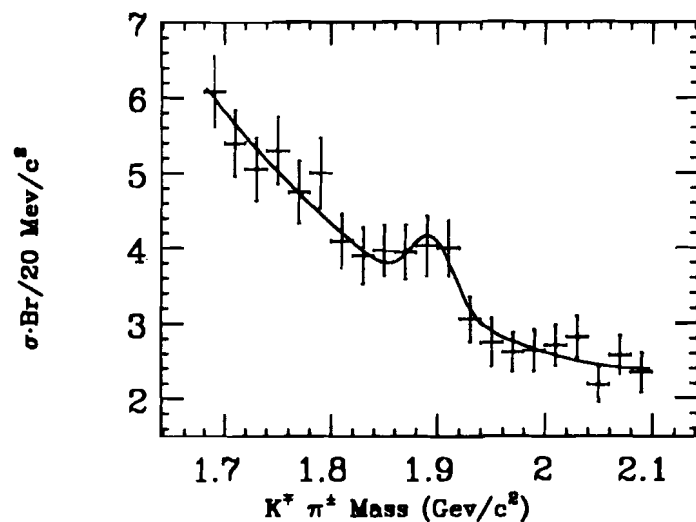
Mass Difference = 142 − 146 Mev/c^2

$\chi^2 < 40$

$L/\sigma_L > 6$

DCA to Primary Vertex < .05"

Primary Vertex in a Target Element

60 ± 52 Events

$\sigma \cdot Br = 2.13 \pm 1.14$ μbarns/Nucleon $-.02 < X_F < .3$

Figure IV.11: $\sigma \cdot Br$, No Čerenkov Cut

Table IV.1 Analysis Cuts

Cut	Yield		Significance
edit cuts	—		—
mass diff.	—		—
$\chi^2_* < 40$	406.0	$\pm$ 99.8	4.0
$\frac{L}{\sigma_L} > 6$	44.3	$\pm$ 27.0	1.6
Čerenkov	43.5	$\pm$ 16.0	2.7
DCA	28.0	$\pm$ 8.5	3.3
Target	26.1	$\pm$ 7.8	3.3

Table IV.2 Lifetime Cuts

Cut	Yield		Significance	$\frac{\text{Signal}}{\text{Background}}$
All but $\frac{L}{\sigma_L}$	258.	$\pm$ 80.3	3.2	.17
$\frac{L}{\sigma_L} > 0$	157.	$\pm$ 65.5	2.4	.17
$\frac{L}{\sigma_L} > 2$	58.2	$\pm$ 18.1	3.2	.65
$\frac{L}{\sigma_L} > 4$	36.9	$\pm$ 11.0	3.4	1.4
$\frac{L}{\sigma_L} > 6$	26.1	$\pm$ 7.8	3.3	2.2
$\frac{L}{\sigma_L} > 8$	17.6	$\pm$ 5.6	3.1	3.8
$\frac{L}{\sigma_L} > 10$	12.9	$\pm$ 4.4	2.9	5.6

$$-.02 < x_F < .3$$

Tables IV.1 & IV.2:   Analysis and Lifetime Cuts

Table IV. 3

	Yield	$\frac{d\sigma}{dx_F}(\bar{x}_F)\cdot$ Br	$\frac{d\sigma}{dx_F}(\bar{x}_F)$
$0. < x_F < .14$, $\bar{x}_F = .07$			
$(K^{\mp} \pi^{\pm}) \pi^{\pm}$ e'gy w't	18.1 ± 5.8	12.1 ± 4.31	$590. \pm 209.$
$(K^{\mp} \pi^{\pm}) \pi^{\pm}$ x_F w't		11.2 ± 3.81	$542. \pm 185.$
$(K^{\mp} \pi^{\pm}) \pi^{\pm}$ no Č e'gy w't	56.1 ± 27.5	11.5 ± 4.94	$559. \pm 240.$
$(K^{\mp} \pi^{\pm}) \pi^{\pm}$ no Č x_F w't		13.2 ± 5.23	$642. \pm 254.$
$(K^+ K^-) \pi^{\pm}$ e'gy w't	$134. \pm 19.$	1.78 ± 0.424	$712. \pm 169.$
$(K^+ K^-) \pi^{\pm}$ x_F w't		2.11 ± 0.424	$845. \pm 169.$
$-.02 < x_F < .3$, $\bar{x}_F = .14$			
$(K^{\mp} \pi^{\pm}) \pi^{\pm}$ e'gy w't	26.1 ± 7.7	7.57 ± 2.24	$368. \pm 109.$
$(K^{\mp} \pi^{\pm}) \pi^{\pm}$ x_F w't		6.31 ± 2.00	$306. \pm 97.4$

Mass Difference = 142 - 146 Mev/c^2

Čerenkov = Restricted K/P$_{amb}$, π's not heavy

$\chi^2_* < 40$

$\frac{L}{\sigma_L} > 6$

DCA to Primary Vertex < .05"

Primary Vertex in a Target Element

Table IV. 3: Comparison of $\frac{d\sigma}{dx_F}(\bar{x}_F)$ for $(K^{\mp} \pi^{\pm}) \pi^{\pm}$ and $(K^+ K^-) \pi^{\pm}$

Table IV.4 Consistency of $\frac{d\sigma}{dx_F}(\bar{x}_F)$

x_F range	Yield	$\frac{d\sigma}{dx_F}(\bar{x}_F)\cdot$ Br	$\frac{d\sigma}{dx_F}(\bar{x}_F)$
$\bar{x}_F = .07$			
-.02 - .16	20.2 ± 6.2	10.21 ± 3.20	$496. \pm 156.$
0.00 - .14	18.1 ± 5.8	11.65 ± 3.67	$566. \pm 178.$
0.02 - .12	13.6 ± 5.6	12.03 ± 4.38	$585. \pm 213.$
0.04 - .10	9.9 ± 4.2	12.82 ± 5.50	$623. \pm 268.$
$\bar{x}_F = .14$			
-.02 - .30	19.6 ± 7.0	5.86 ± 1.89	$285. \pm 91.7$
0.00 - .28	20.0 ± 6.7	6.31 ± 1.93	$306. \pm 93.9$
0.02 - .26	19.3 ± 6.6	6.34 ± 2.04	$308. \pm 99.4$
0.04 - .24	17.2 ± 5.8	5.99 ± 2.04	$291. \pm 99.4$
0.06 - .22	11.8 ± 5.4	4.76 ± 2.21	$231. \pm 108.$
0.08 - .20	8.8 ± 4.4	5.03 ± 2.56	$244. \pm 124.$
0.10 - .18	6.3 ± 4.2	5.48 ± 3.73	$266. \pm 181.$

Mass Difference = 142 - 146 Mev/c^2

Čerenkov = Restricted K/P$_{amb}$, π's not heavy

$\chi_*^2 < 40$

$\frac{L}{\sigma_L} > 6$

DCA to Primary Vertex < .05"

Primary Vertex in a Target Element

Table IV.4:   Consistency of $\frac{d\sigma}{dx_F}(\bar{x}_F)$

Table IV.5

	Yield	$\frac{d\sigma}{dx_F}(\bar{x}_F)\cdot$ Br	$\frac{d\sigma}{dx_F}(\bar{x}_F)$
$\chi_*^2 < 40$	258. $\pm$ 80.9	2.80 $\pm$ 1.45	136. $\pm$ 70.
$\frac{L}{\sigma_L} > 0$	156. $\pm$ 64.4	3.82 $\pm$ 1.18	185. $\pm$ 58.
$\frac{L}{\sigma_L} > 2$	58.2 $\pm$ 18.1	2.58 $\pm$ 0.87	126. $\pm$ 42.
$\frac{L}{\sigma_L} > 4$	36.9 $\pm$ 11.0	3.00 $\pm$ 0.90	146. $\pm$ 44.
$\frac{L}{\sigma_L} > 6$	26.1 $\pm$ 7.7	6.31 $\pm$ 1.99	306. $\pm$ 97.
$\frac{L}{\sigma_L} > 8$	17.6 $\pm$ 5.6	10.0 $\pm$ 4.06	486. $\pm$ 198.
$\frac{L}{\sigma_L} > 10$	12.9 $\pm$ 4.4	26.5 $\pm$ 12.1	1288. $\pm$ 589.

Mass Difference = 142 - 146 Mev/c^2

Čerenkov = Restricted K/P$_{amb}$, π's not heavy

$\chi_*^2 < 40$

$\frac{L}{\sigma_L} > 6$

DCA to Primary Vertex < .05"

Primary Vertex in a Target Element

$-.02 < x_F < .3$

Table IV.5:   Dependence of $\frac{d\sigma}{dx_F}(\bar{x}_F)$ on Lifetime

Chapter V: Analysis of Results

In this chapter the results of Chapter IV are analysed and compared to the results of the LEBC experiment, which studied the production of charm particles in an 800 Gev proton beam at Fermilab using the Lexan Bubble Chamber. The hadronic beam and center-of-mass energy are the closest to the beam characteristics of E400 and makes LEBC the best experiment to compare to E400.

V.A. Comparison to LEBC

Figure V.1 shows the LEBC measurement of $\frac{d\sigma}{dx_F}(\bar{x}_F)$[36]. LEBC concludes that $\frac{d\sigma}{dx_F} + \frac{d\bar{\sigma}}{dx_F} = 150 \pm 75$ μbarns at $\bar{x}_F = .07$ and $\frac{d\sigma}{dx_F} + \frac{d\bar{\sigma}}{dx_F} = 60 \pm 30$ μbarns at $\bar{x}_F = .14$. Using recently published branching ratios[37], the results presented in this thesis imply that $\frac{d\sigma}{dx_F}(\bar{x}_F = .07) = 583 \pm 250$ μbarns/Nucleon and $\frac{d\sigma}{dx_F}(\bar{x}_F = .14) = 337 \pm 110$ for inclusive production of D^{*+} .

Before comparing these results directly, a few remarks are in order. The LEBC cross-section includes all long-lived charm species, presumably D^+, D^-, D^0 , $\overline{D}^0$. The E400 cross-section is for the average of D^{*+} and D^{*-} . Under the assumption of isospin symmetry and that D^* production severly dominates direct D^0 production (as suggested in e^+e^- annihilation), the LEBC result should be divided by four to compare with E400. The target for LEBC was the liquid hydrogen used in the bubble chamber. Figure V.2 shows the dependence of the inclusive differential cross-section for protons as a function of the A of the target nucleus. It is seen that a discrepancy exists between the value for hydrogen as extrapolated from higher A and the measured value[38]. If this trend existed for inclusive charm particle production, the LEBC values should be multiplied by 2 before comparing the E400 values extrapolated from heavier elements. Combining these two factors, the LEBC result should be divided by 2, which leaves their values a factor of 4 or 5 lower than the results of this thesis.

The LEBC collaboration also has published total cross-section results[36]. Their acceptance includes the region $0 < x_F < 1$. By removing the Čerenkov requirement, the acceptance for the E400 data goes to $x_F = 1$ also as shown in Figure VI.9.a. The signal and cross-section that result are shown in Figure V.3. The LEBC result is $\sigma + \bar{\sigma} = 48^{+10}_{-8}$ μbarns. Again the LEBC result needs to be divided by 2 in order to compare to the E400 result of 203 ± 105 μbarns/Nucleon, which again leaves a large discrepancy.

The discrepancy between the E400 cross-section and the LEBC cross-section has caused us to re-examine the issue of the luminosity determination in E400. Table V.1 shows a comparison of the ϕ inclusive cross-section with that of the ACCMOR[39] collaboration. Over the common x_F ranges, the two agree quite well. Table V.2 shows the ratio of the K^{*0} to K^{*+} cross-sections which should be one. Again the agreement is good.

V.B. Mass Shift of D^* and D^* - D^0 Mass-Difference

One should note that the masses, shown in Chapter IV, of the D^* and D^0 are about 21 Mev high as compared to the world average of 2.010 and 1.865 Gev respectively. Also, the peak of the mass-difference in this thesis is 1.5 to 2.0 Mev low (the world average is 145.5 Mev). Presumably this shift reflects a problem with the magnetic analysis of the experiment.

In E400 the longitudinal position and relative field strength of the magnets M1 and M2 were determined by studying Bethe-Heitler pairs produced by the residual photonic beam contamination to our neutron beam. These magnetic parameters were set by requiring that Bethe-Heitler pairs measured in P0 through P4 intersected with zero opening angle at a point upstream of M1. When E687[40] applied this method to set their magnetic corrections, as much as an 8 cm shift was noted in the longitudinal position of M1 relative to its physical survey position. Subsequent analysis suggested that this shift could be ultimately attributed to the failure to correct for electron energy losses due to bremsstrahlung in the material between M1 and M2.

E687 developed a method for checking the position of their magnets. In this method, separate K_s^0 mass distributions are made in bins of an azimuthal angle defined as the angle between the decay plane normal for the decay pions and the principle field direction. If the assumed field is not correct, one can show that the centroid mass of the K_s^0 plotted versus this angle will vary sinusoidally. Figure V.4.a shows that the variation of the K_s^0 mass does occur in the fully processed E400 data. Figure V.4.b shows the mass plots that were fitted to get the masses for Figure V.4.a. Hence, it is clear that the magnets in E400 were not set properly. According to the geometry studies, an oscillation of this magnitude could be due to a misunderstanding of the position of the magnetic field of 8 cm.

To see how such a shift might affect our mass resolution we think of a five Gev pion from the D* decay. If we trace the pion's trajectory from the target, straight down the beam-axis, and then bend it through M1, P2 is struck 24.9 cm from the beam axis. If we maintain that the pion strikes P2 at this point but vary the position of M1 by 8 cm then the bend angle of 80 milliradians varies by ± 2 milliradians resulting in a mismeasurement of the momentum of ± 120 Mev. Such a momentum error will shift the mass according to:

$$P_k \frac{\partial M}{\partial P_k} = E_k^* - \frac{m_k^2}{M} \frac{P}{P_k} \tag{V.1}$$

where E_k^* is the center-of-mass energy of the k'th particle. Using this equation, the 120 Mev error in the pion momentum can correspond to a 1.6 Mev shift in the mass-difference of the D* and D⁰ .

Such a shift in the M1 position, plausibly explains a D* - D mass difference shift of 1.5 MeV. The effects on the D mass might be expected to be much larger owing to the larger Q value for the decay D⁰ → K π . The analysis of this case is more difficult since momentum and opening angle information involves an interplay between both analysis magnets and the simple target constraint is absent.

V.C. Conclusion

This thesis has reported on the investigation of the hadroproduction of D mesons as identified by the reaction D* → (K π) π by E400. A signal was obtained with moderate statistical significance (3.3 σ) but with the proper behavior under successively tighter lifetime cuts. A 20 Mev shift in the centroid of the D⁰ mass and a 1.5 Mev shift in the D* - D⁰ mass-difference relative to the world average was observed. A possible explanation for these shifts in the D⁰ mass , and D* - D⁰ mass-difference is described. The cross-section obtained from this signal agrees favorably with the cross-section from another decay mode as measured by the same experiment. Both E400 cross-sections, as well as those of many other experimental groups are considerably larger than lowest order QCD calculations. A direct comparison was made of both the differential and total cross-sections found by E400 with those found by the LEBC experiment at Fermilab, which closely matched E400's beam energy and beam type, and considerable disagreement was found. E400 and LEBC have vastly different systematics but we have not been able to find an explicit explanation for the discrepancy.
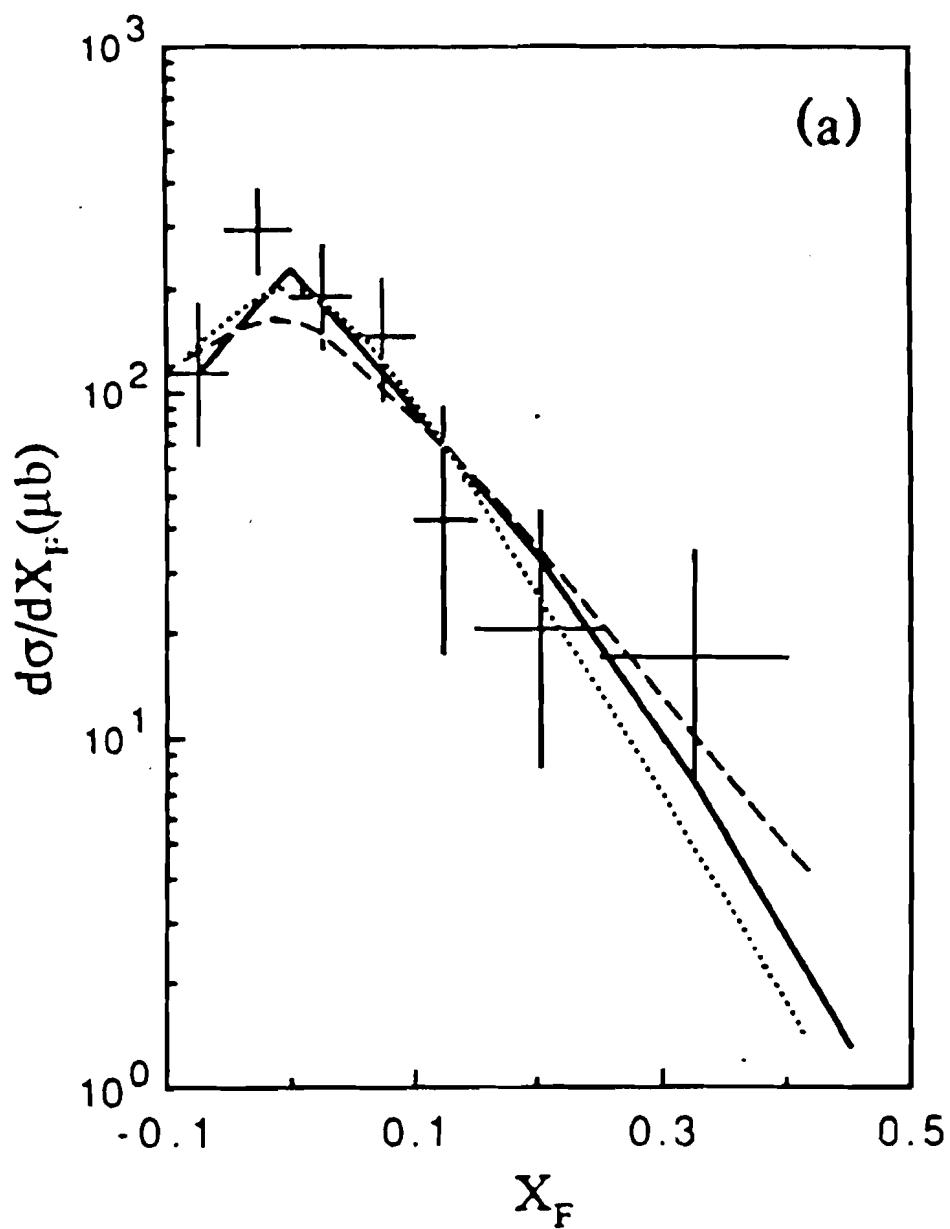
Figure V.1: $\frac{d\sigma}{dx_F}(\bar{x}_F)$ from LEBC

The plotted points are data. The solid line is an empirical fit.

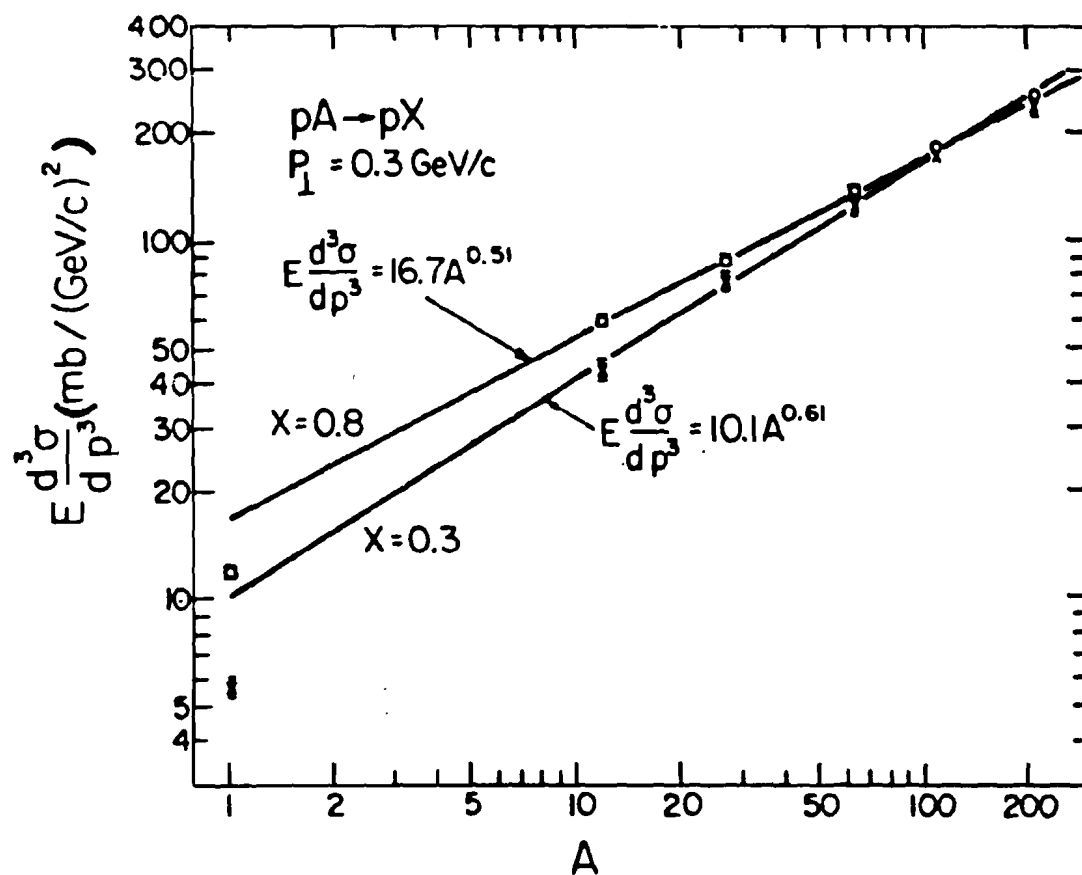The dotted and dashed curves are the results of fusion-model calculations.

Figure V.2:   The Hydrogen Effect for the Extrapolation of A^α

Note that the straight line fits to the data
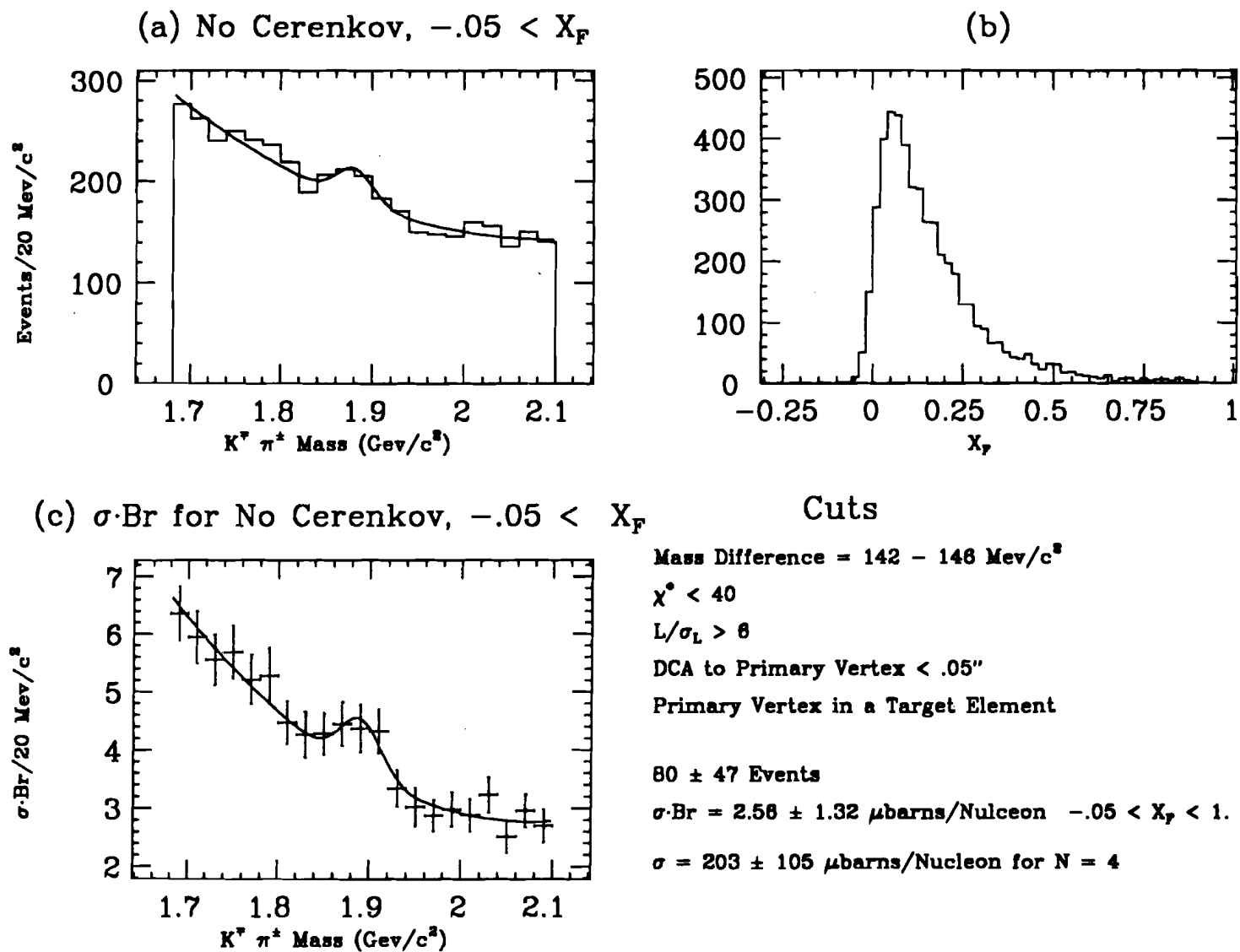
of the heavy elements do not match the data at A = 1.

(a) No Cerenkov, $-.05 < X_F$

(b)

(c) $\sigma \cdot Br$ for No Cerenkov, $-.05 < X_F$

Cuts

Mass Difference $= 142 - 146$ Mev/c^2

$\chi^2 < 40$

$L/\sigma_L > 6$

DCA to Primary Vertex $< .05''$

Primary Vertex in a Target Element

80 ± 47 Events

$\sigma \cdot Br = 2.56 \pm 1.32$ μbarns/Nulceon $\quad -.05 < X_F < 1.$

$\sigma = 203 \pm 105$ μbarns/Nucleon for N $= 4$

Figure V.3: $\quad \sigma$ for $x_F > 0$

The cut in Feynman X has been removed to enable a direct comparison to LEBC.

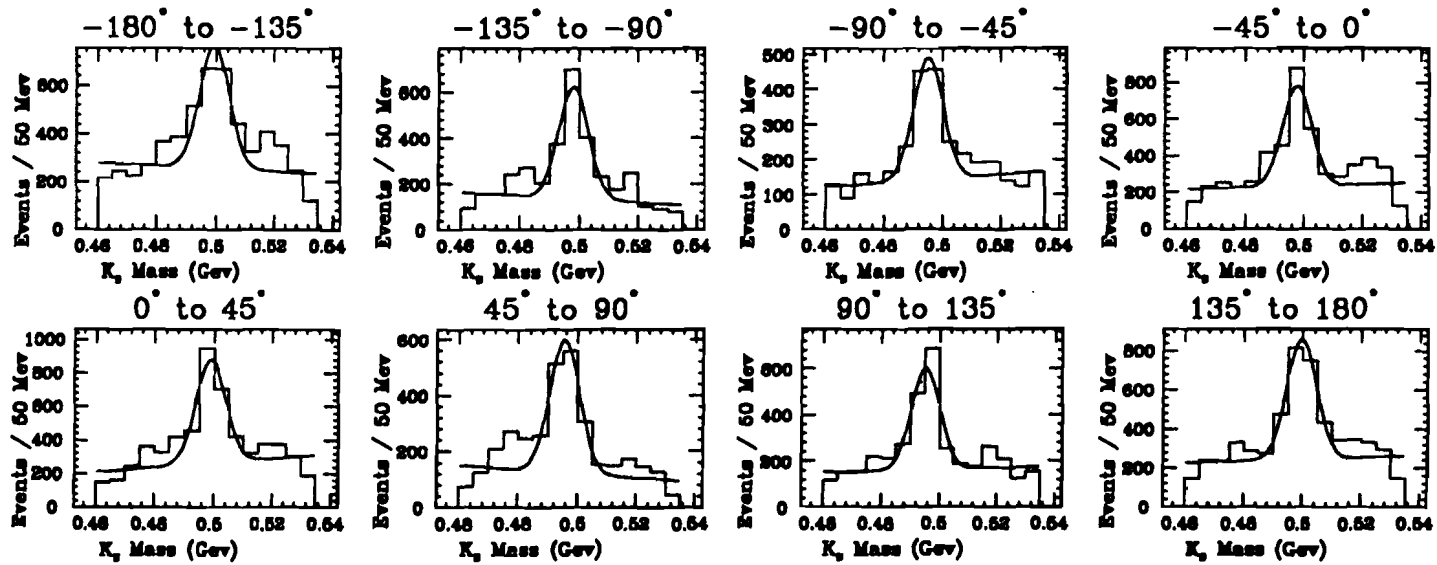## (a) M1 Position Study
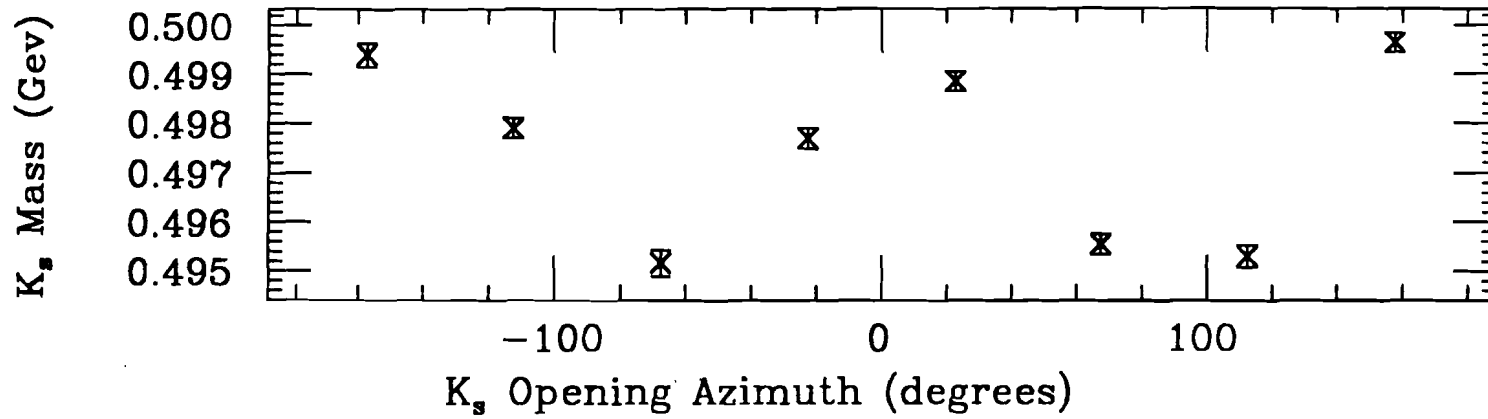
(b) K_s Fits

Figure V.4: Variation of K_s^0 Mass on Azimuth

(a) shows the variation of the K_s^0 mass. (b) shows the fit used.

The fits are a Gaussian with a linear background.

Table V.1 ϕ Inclusive Cross Section

x_f range	dN/dx_f (ACCMOR)	dN/dx_f (μb, $A^{.9}$)	# of events
-.06 to -.02	—	1545 ± 152	11752 ± 1762
-.02 to +.02	—	1010 ± 150	7682 ± 1141
+.02 to +.06	1327 ± 117	1089 ± 109	8287 ± 833
+.06 to +.10	1056 ± 51	1023 ± 79	7785 ± 599
+.10 to +.14	750 ± 35	871 ± 89	6625 ± 677
+.14 to +.18	510 ± 24	753 ± 133	5652 ± 1001

Table V.2 Inclusive K^* Cross Sections

x_f range	$\frac{d\sigma}{dx_f}$ (K^{*0}) (mb)	$\frac{d\sigma}{dx_f}$ (K^{*+}) (mb)	ratio
-.02 to +.02	10.1 ± 1.4	7.5 ± 2.7	$1.33 \pm .51$
+.02 to +.06	6.8 ± 0.8	6.6 ± 1.5	$1.03 \pm .24$
+.06 to +.10	5.1 ± 0.7	4.7 ± 1.1	$1.09 \pm .28$
+.10 to +.14	4.1 ± 0.7	4.1 ± 0.9	$0.99 \pm .27$

Tables V.1 & V.2: ϕ and K^* Cross-sections for Luminosity Verification

Appendix A: Magnets

Many techniques and properties used in the analysis of this experiment (such as track reconstruction, Vee finding, and the impact parameter analysis) depend heavily on a thorough understanding of the magnetic fields of the two analysis magnets. The magnetic fields were measured extensively and these measurements were converted to a digital map for use in the analysis programs. These maps were then used to trace trajectories during reconstruction for improved position and momentum resolution.

A.1. Overview

In the ideal world of first year college physics textbooks, the magnetic field exists only between the pole faces, has straight field lines between these faces, and has a constant field strength. Particles passing through them are bent in a circular arc while in the magnetic field and move in straight lines when outside.

In Figure A.1a, the dotted curve shows the trajectory of a particle through an ideal magnet whose field is shown by the dotted box-like curve. In this ideal system, the magnet can be thought of as giving the particle a transverse momentum "kick", P_k, equal to $\frac{e}{c}HL$ where e is the charge of an electron, c is the speed of light, H is the strength of the magnetic field, and L is the length of the magnetic field. Therefore the trajectory would be deflected through an angle $\theta = \frac{P_k}{P}$. We used this idealism for a first approximation of the particle momentum in the reconstruction (Pass 1). From the wire chamber information we knew the trajectories on either side of M2. By tracing these to the center of the magnet, as shown by the dashed lines in Figure A.1a, we could calculate the the deflection angle and then the momentum of the particle. This was called the "kink method". For stubs, where we only had the trajectory in chambers P0 - P3, we assumed that the particle came from the center of the target. This then allowed us to calculate the bend in M1 and gave us a first approximation of a stub's momentum.

In reality however, the field lines bulge out of the openings which means that the field has components in all three directions and turns on with a finite slope. A first approximation of reality would allow an experiment to be long enough so that the other components of the spectrometer could be placed in areas where residual fields could be ignored. In Figure A.1a, the solid line shows the trajectory of a particle passing through

a simplified field taken from field maps of M2 whose field is shown as the flattened bell curve of Figure A.1a. The difference between this trajectory and the ideal one described above is shown in Figure A.1b. (The reason the difference does not return to 0 at the downstream side is that the plots were generated by a tracing program that used a finite step size to move the particle through the field. Therefore, the $\int B \cdot dl$ could not be exactly matched for the two fields). Outside the field region, the trajectories are the same and barring the effects to be discussed, the kink method would still be valid.

However, a spectrometer built this way would be of tremendous length and have very large transverse dimensions if it were to have adequate angular acceptance. Fixed target experiments should be short along the direction of the beam but should have a large area perpendicular to the beam. Shortening the spectrometer means placing components near the magnets (and sometimes inside them) and magnets with large transverse areas have fields that extend beyond the openings for a significant distance. In our experiment, the wire chamber P3 was at z=155 in the scale of Figure A.1. The magnetic field still exists there and the difference plot shows that the two trajectories have not quite merged yet.

Now our idealism is destroyed. In extrapolating from P4 to P3 and on to the center of M2, the wire chamber information of P3 is not part of a straight line segment. In response a correction was developed to fix this. It is of the form:

$$\Delta y = \frac{1}{P}[A - Bx^2 - Cy^2]. \tag{A.1}$$

This accounts for the momentum dependence of the deflection and the x and y terms reflect the variation of B_x with x and y (as will be shown shortly). This correction was originally developed for P0 as the field of M1 is approximately twice as strong at P0 as M2 is at P3. The correction was eventually applied to both.

The trajectories shown in Figure A.1a are symmetric in that the exit angle is a mirror image of the entrance angle. This places the intersection of the two line segments at the center of the magnet. If the trajectory is not symmetric, then the intersection does not occur at the center. A correction called the bend-center correction was developed to provide the proper offset to account for this. Originally this correction was geometrical,

but as the fields of the magnets were understood more clearly, the bend-center correction and also the P0 and P3 corrections were changed to reflect the new knowledge.

The above procedures and corrections were used for Pass 1 of our analysis chain. The success of E400 depended on our ability to link tracks in the main spectrometer with the Vertex Chamber so that we could increase our momentum and position resolution in subsequent passes of the analysis. This required a greater understanding of the magnetic fields.

A.2. Rotation of the Magnetic Fields

The first effect that was discovered was that the main-field components of the two magnets were not parallel to each other nor to the x coordinate of the experiment. The field of M1 is rotated counter-clockwise about the beam axis by 7.7 milliradians. The main field of M2 was found to be rotated counter-clockwise about the beam axis by 4.125 milliradians.

As a particle passes through the magnet, its trajectory is bent in a plane perpendicular to the main field. The coordinate system of the experiment was a left handed one with z pointing downstream, y pointing up, and x horizontal. The x and y of the coordinate system was determined by the wire chambers and the fields of the magnets were supposed to be parallel to the x axis of the wire chambers. That way the change in trajectory would occur in the slope of y only. Since the main-field component of M1 is not aligned with the x axis, the bending introduces a displacement in x.

$$\Delta x = x - x_0 = z \times \delta y' \times \Theta. \tag{A.2}$$

This is for M1 where the track is being extrapolated from the area of P0 - P2 to the target region. x_0 is the x position of the primary vertex, z is the distance from the center of M1 to the primary vertex (actually the center of the target), $\delta y'$ is the bend in y through M1, Θ is the rotation of the field, and x is the extrapolation of the track to the z of the primary target.

To determine this correction, the primary vertex was found for events with more than four tracks. Stubs were then extrapolated back to this vertex using a single-bend approximation to determine their momenta. The vertex was found again using both tracks and stubs. Then a plot was made of the difference between the x position of the

track or stub at the z of the primary vertex and the x position of the primary vertex verses the bend of the track in M1. From this Θ can be found as seen in Figure A.2 which shows before and after plots. A similar procedure was used for M2 where Δx was defined at P4.

A.3. Traces

For a particle that passes through the full spectrometer, the reconstruction programs gave the trajectory of the particle for the area between the two magnets and downstream of M2. This was done using the kink approximation described above. In order to get more accurate trajectories and extrapolate upstream of M1, a moment expansion method was developed. This allowed more accurate extrapolation of trajectories through the magnets.

In an ideal magnet, with the field solely in one direction (x):

$$\frac{y'}{\sqrt{1 + y'^2 + x'^2}} = \frac{y'_0}{\sqrt{1 + y'^2_0 + x'^2_0}} + \frac{K}{p}, \qquad (A.3)$$

with

$$K(z) \equiv .3 \int_{z_0}^{z} dz_1 B_x(z_1), \qquad (A.4)$$

where primes denote differentiation with respect to z and subscripts refer to initial conditions. Because of the vanishing B-fields we can use some algebraic tricks to obtain

$$\frac{y'}{\sqrt{1 + y'^2}} = \frac{y'_0}{\sqrt{1 + y'^2_0}} + \frac{K'}{p} \equiv g_y \qquad (A.5)$$

with the following definitions:

$$K' \equiv \frac{\sqrt{1 + y'^2_0 + x'^2_0}}{\sqrt{1 + y'^2_0}} K, \qquad (A.6)$$

$$I \equiv \frac{y'_0}{\sqrt{1 + y'^2_0}}, \qquad (A.7)$$

$$\alpha \equiv \frac{K'}{p}. \qquad (A.8)$$

This equation is solved for y', integrated, and then Taylor expanded to get the result

$$y = y_0 - \sum_{j=0}^{\infty} \frac{f^{(j)}(I)}{j!} M_j. \qquad (A.9)$$

This uses the definitions

$$f^{(j)}(I) \equiv \frac{\partial^j}{\partial I^j} \left(\frac{I}{\sqrt{1-I^2}} \right), \qquad (A.10)$$

$$M_j \equiv \int_{z_0}^{z} dz_1 \alpha^j(z_1). \qquad (A.11)$$

The advantage of this method is that all the integrals need to be evaluated only once to tabulate the M_j as a function of z. The value y(z) is obtained by evaluating a polynomial involving the moments M_j and the initial conditions y_0 and y_0'. For x(z) we assume

$$x = x_0 + x_0' z. \qquad (A.12)$$

In addition to these effects, the fact that these are not ideal magnets must be taken into account. The curvature of the field at the openings introduces field components in the y and z directions which also affect trajectories. For B_y and B_z we were able to do similar moment calculations which require a one-time evaluation of the integrals as above.

A.4. Bends in the X Direction

The motion of a particle in a magnetic field, where dS is an element of path length, is given by:

$$\frac{d\vec{P}}{dS} = \frac{g}{P} \vec{P} \times \vec{B}. \qquad (A.13)$$

The value of g = 0.29979 if P (the charge - signed momentum magnitude) is measured

in MeV, B is measured in kGauss, and S is measured in centimeters. An alternative form is:

$$\frac{d}{dz} \frac{x'}{\sqrt{1 + x'^2 + y'^2}} = \frac{g}{P} (y' \, B_z - B_y). \tag{A.14}$$

Expanding the radical in Equation A.14 to second order in x' and y' prior to taking derivative we get:

$$\frac{d^2 x}{dz^2} \approx \frac{g}{P} (y' \, B_z + x' \, y' \, B_x - B_y). \tag{A.15}$$

The first two terms create the weak-focusing effect. One of these terms is due to the off-field component, B_z; while the second term describes the fact that charged tracks follow helical trajectories and thus must change x angle due to the pitch of the helix.

A.4.a. Weak-Focusing Effect

To a good approximation, the B_z is given by:

$$B_z = x \, \frac{\partial B_z}{\partial x} = x \, \frac{\partial B_x}{\partial z}. \tag{A.16}$$

Using the Equation A.16 approximation, the two weak-focusing terms can be written as:

$$y' \, B_z + x' \, y' \, B_x = y' \, \frac{\partial}{\partial z} (x \, B_x) = \frac{\partial}{\partial x} (y' \, x \, B_x) - x \, B_x \, \frac{\partial^2 y}{\partial z^2}. \tag{A.17}$$

The final portion of Equation A.17 is the usual manipulation used to perform integration by parts. The zero order expression for the y motion which follows from Equation A.14 is:

$$\frac{\partial^2 y}{\partial z^2} = \frac{g}{P} \, B_x. \tag{A.18}$$

Inserting this expression into Equation A.17, we obtain:

$$\frac{\partial^2 x}{\partial z^2} \approx \frac{g}{P} \, \frac{\partial}{\partial z} (y' \, x \, B_x) - \left(\frac{g}{P}\right)^2 \, x \, B_x^2. \tag{A.19}$$

Integrating through the magnet:

$$\delta x' = \int\limits_{-\infty}^{\infty} dz \, \frac{\partial^2 x}{\partial z^2} = \frac{g}{P} \, |_{-\infty}^{\infty} \, x \, y' \, B_x - \left(\frac{g}{P}\right)^2 \int\limits_{-\infty}^{\infty} dz \, x \, B_x^2$$

$$= -\left(\frac{g}{P}\right)^2 \int\limits_{-\infty}^{\infty} dz \; x \; B_x^2. \tag{A.20}$$

We have dropped the "parts" part since we assume that $B_x(z = \pm\infty) = 0$.

Equation A.20 demonstrates the classic weak-focusing feature that the x-bend *does not depend on the charge!* It is useful to define an approximate straight line x trajectory relative to the center of gravity (z_{cg}) of the squared B_x field.

$$x \approx \bar{x} + (z - z_{cg}) \, x' \quad \text{where} \quad \int\limits_{-\infty}^{\infty} dz \, (z - z_{cg}) \, B_x^2 = 0. \tag{A.21}$$

Hence:

$$\delta x' = -\left(\frac{g}{P}\right)^2 \, \bar{x} \int\limits_{-\infty}^{\infty} dz \; B_x^2. \tag{A.22}$$

Equation A.22 demonstrates the focusing aspects of the weak-focusing effect – the angular deflection in x is proportional to $\bar{x}$, or the intercept of the track at the squared-field center-of-gravity.

A particularly elegant parameterization of Equation A.22 uses the y-bend angle (δ) and two effective "effective lengths", L and L_*, defined by:

$$L = \int\limits_{-\infty}^{\infty} dz \; \frac{B_x}{B_o} \quad \text{where} \quad B_o = Max(B_x(z))$$

$$\delta = \frac{g}{P} \; B_o \; L$$

$$L_* = \int\limits_{-\infty}^{\infty} dz \; \left(\frac{B_x}{B_o}\right)^2. \tag{A.23}$$

We can re-write Equation A.22 as:

$$\delta x' = -\left(\frac{\delta}{L}\right)^2 \, \bar{x} \int\limits_{-\infty}^{\infty} dz \; \left(\frac{B_x}{B_o}\right)^2 = -\left(\frac{\delta}{L}\right)^2 \, L_* \; \bar{x} \; . \tag{A.24}$$

For the case of a step or box field, we have:

$$B_x(z - z_{cg}) = B_o \quad \text{for} \quad -L/2 < z - z_{cg} < L/2.$$

$$\text{Thus} \quad L_* = \int\limits_{-\infty}^{\infty} dz \ \left(\frac{B_x}{B_o}\right)^2 = L. \tag{A.25}$$

In general, we have an inequality which follows from the fact that $(B_x/B_o) < 1$:

$$\int\limits_{-\infty}^{\infty} dz \ B_x \ \left(\frac{B_x}{B_o}\right) < \int\limits_{-\infty}^{\infty} dz \ B_x \ < B_o \ L.$$

$$\text{Thus} \ L_* = \int\limits_{-\infty}^{\infty} dz \ \left(\frac{B_x}{B_o}\right)^2 < L. \tag{A.26}$$

As seen in Figure A.1, the magnetic field of M2 has some step-like structure with $L \approx 60$ in. Therefore, we expect:

$$\delta x' \leq -\frac{\delta^2}{L} \ \bar{x} \leq -5 \times 10^{-3} \ \delta^2 \ \bar{x} \tag{A.27}$$

or

$$\delta x' = \alpha \ \delta^2 \ \bar{x}. \tag{A.28}$$

A.4.b. B_y Contribution

From Equation A.15, we have that the B_y contribution to the x-bend is:

$$\frac{d^2 x}{dz^2} \approx -\frac{g}{P} \ B_y. \tag{A.29}$$

To an excellent approximation, the B_y field is essentially:

$$B_y = \frac{\partial^2 B_y}{\partial x \partial y} \ x \ y = \frac{\partial^2 B_x}{\partial y^2} \ x \ y \equiv B_o \ \beta(z) \ x \ y \tag{A.30}$$

where $\beta(z)$ gives the normalized y curvature of the B_x field. Hence:

$$\delta x' = -\frac{g B_o}{P} \int\limits_{-\infty}^{\infty} dz \ x \ y \ \beta = -\frac{\delta}{L} \int\limits_{-\infty}^{\infty} dz \ x \ y \ \beta(z). \tag{A.31}$$

In the absence of a shielding plate, one would expect that $\beta(z)$ is essentially symmetric

about the center of the magnets, which we will take as $z = 0$. Let us define symmetry and anti-symmetry operators:

$$S(f) = \frac{f(z) + f(-z)}{2} \quad , \quad A(f) = \frac{f(z) - f(-z)}{2}. \tag{A.32}$$

Only the symmetric part of the $x \, y \, \beta(z)$ will survive under the Equation A.31 integral.

$$S(x \, y \, \beta) = S(x) \, S(y) \, \beta + A(x)A(y) \, \beta. \tag{A.33}$$

Using the approximate x-trajectory given in Equation A.21, the symmetric and anti-symmetric terms are:

$$S(x) = \bar{x} \quad , \quad A(x) = x'. \tag{A.34}$$

The true y trajectory is rather complicated but we will use an approximate kink trajectory given by:

$$y = \bar{y} + y'_a \, z + \frac{\delta}{2} \, \Theta(z) \, z,$$

$$\text{where } y'_a = \frac{y'_d + y'_u}{2} \quad , \quad \Theta(z) = 1 \text{ for } z > 0 \quad , \quad \Theta(z) = -1 \text{ for } z < 0. \tag{A.35}$$

Hence the symmetric and anti-symmetric portions of the y-trajectory are:

$$S(y) = \bar{y} + \frac{\delta}{2} \, z \, \Theta(z) \quad , \quad A(y) = y'_a \, z. \tag{A.36}$$

In light of the foregoing, we have essentially three terms:

$$\delta x' = -\frac{\delta}{L} \, \bar{x} \, \bar{y} \, 2 \int_0^\infty dz \, \beta \; - \frac{\delta^2}{L} \, \bar{x} \int_0^\infty dz \, z \, \beta \; - \frac{\delta}{L} \, x' \, y'_a \, 2 \int_0^\infty dz \, z^2 \, \beta. \tag{A.37}$$

To progress further, we make some speculative limits. For static fields we have:

$$\frac{\partial^2 B_x}{\partial x^2} + \frac{\partial^2 B_x}{\partial y^2} + \frac{\partial^2 B_x}{\partial z^2} = 0. \tag{A.38}$$

This equation shows that quadratic x- and y-variation in the main-field component is

inevitable and one expects strongest variations in the fringe limit. From Figures A.5.d and A.5.e it can be seen that

$$|\frac{\partial^2 B_x}{\partial x^2}| \gg |\frac{\partial^2 B_x}{\partial y^2}|,$$

which means that the x-variation essentially saturates Equation A.38. In this x-saturation limit, $\beta \to 0$, and the B_y contribution becomes negligible. We can consider the opposite limit, the y-saturation limit, where:

$$\frac{\partial^2 B_x}{\partial x^2} \approx -\frac{\partial^2 B_x}{\partial z^2}. \tag{A.39}$$

It is of interest to compare the second term of Equation (A.37) to the weak-focusing effect given by Equation (A.17) in the y-saturation limit (Equation A.39)

$$\delta x' = \frac{\delta^2}{B_o L} \bar{x} \int_0^\infty dz \, z \, \frac{\delta^2 B_x}{\partial z^2}. \tag{A.40}$$

We can write the integrand of Equation A.40 as:

$$z \, \frac{\delta^2 B_x}{\partial z^2} = \frac{\partial}{\partial z} \left(z \frac{\partial B_x}{\partial z} \right) - \frac{\partial B_x}{\partial z}. \tag{A.41}$$

The first term of Equation A.41 will vanish under the Equation A.38 integral while the second term is simple:

$$\delta x' = \frac{\delta^2}{B_o L} \bar{x} \, (B_x(0) - B_x(\infty)) = \frac{\delta^2}{L} \bar{x}. \tag{A.42}$$

Amazingly enough, Equation A.42 nearly cancels the weak-focusing effect of Equation A.27 in the y-saturation limit. However reality is much closer to the x-saturation limit where there is no B_y contribution.

The first term of Equation A.35 would vanish in the Equation A.39 limit since it is then proportional to the first derivative of B_x at $z = 0$ and $\frac{\partial B_x}{\partial z} = 0$ if the field is maximal at center of magnet.

Finally we consider the last term of Equation A.35 in the y-saturation limit,

$$\delta x' = -\frac{\delta}{L}\, x'\, y'_a\, 2 \int\limits_0^\infty dz\, z^2\, \beta = \frac{\delta}{B_o L}\, x'\, y'_a\, 2 \int\limits_0^\infty dz\, z^2\, \frac{\partial^2 B_x}{\partial z^2}. \qquad (A.43)$$

This integral can be considerably simplified by using the identity:

$$z^2\, \frac{\partial^2 B_x}{\partial z^2} = \frac{\partial}{\partial z}\left(z^2\, \frac{\partial B_x}{\partial z}\right) - 2\frac{\partial}{\partial z}(z\, B_x) + 2\, B_x. \qquad (A.44)$$

Both the first and second term of Equation A.44 vanish under the Equation A.43 integration. Hence in the y-saturation limit one obtains for the last term:

$$\delta x' = 2\delta\, x'\, y'_a. \qquad (A.45)$$

If the y-saturation limit were rigorously true (it is assuredly not), Equation A.43 would represent the complete x-bend effect.

A.5. Ziptrak

The Ziptrak was a device assembled by Fermilab to map the field of analysis magnets. It consisted of three mutually-perpendicular coils mounted on a cart that could be positioned in the magnet opening by computer control. Each coil was connected to an integrator and then to an ADC which was read by the computer. The cart moved in the z direction in a hollow beam which was positioned in x and y by manipulators. Measurements of the integrated field were taken at approximately 1 inch intervals in x, y, and z. The beam was placed at each x,y position. The cart then moved from a position approximately 15 inches outside the magnet, through the magnet, stopping approximately 15 inches on the other side of the magnet. The field measurements were integrated at each measurement point with the zero field point being taken to be at the starting point. The cart then returned, re-integrating the field again. For M2, this was done for an x,y area of 20 × 24 inches. M1 had a shield plate on its upstream end. While the magnet had a normal aperture of the coils of 15 × 30 inches , the shield plate restricted the upstream aperture to 4 × 11 inches. This caused the main-field component to fall of more rapidly but as will be seen, it enhanced other components greatly and

had to be accommodated by the Field Maps and Traces. Quite a bit of work had to be done to convert the Ziptrak information into a format that could be used in evaluating our data. The mapped field had to be referenced to the spectrometer coordinate system. This included not only positioning in x, y, and z but also rotations both of the mapping system and of the measuring coils within the mapping system. As might be expected, the Ziptrak system was not set up aligned exactly with the spectrometer system. Also, the coils were not exactly aligned with the Ziptrak coordinates and the coils themselves were not orthogonal to each other.

A.6. Field Maps

In order to use the Traces described above (section A.3), a map of the magnetic fields for each magnet had to be made. The maps were used in evaluating the Trace integrals by stepping particles through the fields according to Lorentz-force equations.

The symmetry of the boundary-value problem for B_x states that the kick should be:

$$\int B_x dz = \text{const} + \text{const}'(cos\frac{\pi x}{a}cosh\frac{\pi y}{a}). \tag{A.46}$$

Because $\frac{\partial B_x}{\partial y} = \frac{\partial B_y}{\partial x}$ the kick of B_y should be

$$\int B_y dz = \text{const}'' - \text{const}'(sin\frac{\pi x}{a}sinh\frac{\pi y}{a}). \tag{A.47}$$

If B_x is expanded in a Taylor expansion to second order, then only a term proportional to xy appears for B_y. However breaking the measured fields down into second order components never adequately matched Equations A.46 and A.47.

Finally B_x was expanded to fourth order:

$$B_x = \text{const} + Ax^2 + By^2 + Cx^2y^2 + Dx^4 + Ey^4. \tag{A.48}$$

Since, by Maxwell's equations: $\frac{\partial B_x}{\partial y} = \frac{\partial B_y}{\partial x}$ and $\frac{\partial B_x}{\partial z} = \frac{\partial B_z}{\partial x}$:

$$B_y = 2Bxy + \frac{2}{3}Cx^3y + 4Exy^3 \tag{A.49}$$

$$B_z = \frac{\partial \text{const}}{\partial z}x + \frac{\partial A}{\partial z}\frac{x^3}{3} + \frac{\partial B}{\partial z}xy^2 + \frac{\partial C}{\partial z}\frac{x^3y^2}{3} + \frac{\partial D}{\partial z}\frac{x^5}{5} + \frac{\partial E}{\partial z}xy^4. \tag{A.50}$$

The Ziptrak data was then broken down into expansions of this form.

A.7. Transformations

In breaking down the fields into fourth order components, the components shown in Equations A.48 - A.50 were not the only components that appeared. For instance, there were terms linear in x and y for B_x, B_y, and B_z. The actual linear terms obtained implied a non-zero curl (Figure A.3) and divergence (Figure A.4) which violate Maxwell's equations. Other components, such as $\frac{\partial B_z}{\partial x}$ (Figure A.5.b) would not be expected to exist at all if the magnet had the reflection symmetry of Equations A.51 - A.53 below. The following investigation determined the reason.

In the work described section A.6, certain symmetries have been assumed. Specifically:

$$B_x(x, y, z) = B_x(-x, y, z) = B_x(x, -y, z) \qquad (A.51)$$

$$B_y(x, y, z) = -B_y(-x, y, z) = -B_y(x, -y, z) \qquad (A.52)$$

$$B_z(x, y, z) = -B_z(-x, y, z) = B_z(x, -y, z). \qquad (A.53)$$

In such a reference frame B_y and B_z would vanish on the "magnetic" z axis (which ideally would be the axis of the beam line), B_x would have only even powers of x and y, B_y would have only odd powers of x and y, and B_z would have odd powers of x and even powers of y. If one expands the fields in a Taylor expansion such as:

$$B_x(x, y, z) = B_x(0, 0, z) + \frac{\partial B_x}{\partial x}x + \frac{\partial B_x}{\partial y}y + \frac{\partial^2 B_x}{\partial x \partial y}xy + \frac{1}{2}\frac{\partial^2 B_x}{\partial x^2}x^2 + \frac{1}{2}\frac{\partial^2 B_x}{\partial y^2}y^2, \quad (A.54)$$

where these partial derivatives are taken on axis $(0, 0, z)$ so that:

$$\frac{\partial B_x}{\partial x} = \frac{\partial B_x}{\partial x}(0, 0, z), \frac{\partial B_x}{\partial y} = \frac{\partial B_x}{\partial y}(0, 0, z), \frac{\partial^2 B_x}{\partial x \partial y} = \frac{\partial^2 B_x}{\partial x \partial y}(0, 0, z), \qquad (A.55)$$

etc. In another reference frame the results of a transverse polynomial fit at fixed $\tilde{z}$ will be:

$$\tilde{B}_x(\tilde{x}, \tilde{y}, \tilde{z}) = \tilde{B}_x(0, 0, \tilde{z}) + \frac{\partial \tilde{B}_x}{\partial x}\tilde{x} + \frac{\partial \tilde{B}_x}{\partial y}\tilde{y} + \frac{\partial^2 \tilde{B}_x}{\partial x \partial y}\tilde{x}\tilde{y} + \frac{1}{2}\frac{\partial^2 \tilde{B}_x}{\partial x^2}\tilde{x}^2 + \frac{1}{2}\frac{\partial^2 \tilde{B}_x}{\partial y^2}\tilde{y}^2. \quad (A.56)$$

For these fits to be valid, these partial derivatives should be evaluated on $(0, 0, \tilde{z})$ which is a different axis than $(0, 0, z)$. In the above expression the term $\tilde{B}_x(0, 0, \tilde{z})$ transforms

as a rank-1 tensor (or vector), the terms $\frac{\partial \tilde{B}_x}{\partial x}$ and $\frac{\partial \tilde{B}_x}{\partial y}$ transform as rank-2 tensors, and the terms $\frac{\partial^2 \tilde{B}_x}{\partial x \partial y}$, $\frac{\partial^2 \tilde{B}_x}{\partial x^2}$, and $\frac{\partial^2 \tilde{B}_x}{\partial y^2}$ transform as rank-3 tensors. The transformation rules can be written in terms of the transformation matrix $a_{i,j}$:

$$a_{i,j} = \begin{pmatrix} 1 & -\epsilon_3 & \epsilon_2 \\ \epsilon_3 & 1 & -\epsilon_1 \\ -\epsilon_2 & \epsilon_1 & 1 \end{pmatrix} \tag{A.57}$$

where (ϵ_1, ϵ_2, ϵ_3) are the small rotation angles linking the two reference frames. In this transformation, certain derivatives will dominate others. For instance, due to the overall magnitude of $\mathbf{B}_x$, $\frac{\partial B_x}{\partial x}$ will dominate any other component in an equation except for $\mathbf{B}_x$. As in Equation A.26, this derivative and other strong derivatives can be substituted into the expansions. The components of the Taylor expansion that should not appear, but do, are actually these strong components that are leaking into other components due to small rotations. In particular a net divergence was found and a net z-component was found for the curl. A curl can be generated if the magnetic unit-vectors are rotated with respect to the coordinate unit-vectors. A divergence can be generated if either the coordinate unit-vectors or magnetic unit-vectors are not not mutually perpendicular. If we denote the B-field rotation-matrix by $b_{i,k}$ and the coordinate rotation-matrix by $a_{j,k}$ with $b \neq a$ we can account for curl components. In addition, if either $a_{j,k} \neq -a_{k,j}$ or $b_{i,k} \neq -b_{k,i}$, due to non-orthogonality of the magnetic probes, a divergence can be generated. The final system was to rotate fields about the x-axis by an angle β, using a b-matrix and rotate the coordinate z-axis about the y-axis by an angle α, using a non-orthogonal a-matrix. These matrices are of the form:

$$a_{i,j} = \begin{pmatrix} 1 & 0 & \alpha \\ 0 & 1 & 0 \\ 0 & 0 & 1 \end{pmatrix} \tag{A.58}$$

$$b_{i,j} = \begin{pmatrix} 1 & 0 & 0 \\ 0 & 1 & -\beta \\ 0 & \beta & 1 \end{pmatrix} \tag{A.59}$$

These transformations give rise to a curl of:

$$(\nabla \times \tilde{B})_z = -\beta \frac{\partial B_z}{\partial z} \qquad (A.60)$$

and a divergence of:

$$\nabla \cdot \tilde{B} = \alpha \frac{\partial B_z}{\partial z}. \qquad (A.61)$$

Again we can substitute $\frac{\partial B_z}{\partial x}$ for $\frac{\partial B_z}{\partial z}$.

Figures A.3 and A.4 show the results of this work for M1. As mentioned above, Figure A.3 shows $\frac{\partial B_x}{\partial y} - \frac{\partial B_y}{\partial x}$. The dashed line in Figure A.3 is $.007 \times \frac{\partial B_z}{\partial x}$ showing that the curl is due to leakage from B_z. Therefore the value of β in Equations A.59 and A.60 is .007. Figure A.4 compares the divergence with $\frac{\partial B_z}{\partial x}$ and shows that α in Equations A.58 and A.61 is .016. Figures A.5 - A.7 show the expansion to fourth order for B_x, B_y, and B_z for M2.

Once a coordinate system that obeys Maxwell's equations has been determined there is still the issue of terms like $\frac{\partial B_z}{\partial x}$ to resolve. Terms such as $\frac{\partial B_z}{\partial x}$ do not follow the symmetry assumptions of Equations A.51 - A.53 so we have termed them "wrong-symmetry" terms. The transformation of equations such as Equation A.56 using rotation-matrices such as A.57 relate partial derivatives evaluated at the same spacial point. The fit parameters, however, are partial derivatives which are evaluated at two different space points related by their coordinate axes as $(0, 0, \tilde{z}) = (-\epsilon_2 z, \epsilon_1 z, z)$. Combining the coordinate translation with the tensor rotation for the rank-2 case (for example) we have the full transformation between fit parameters (to order ϵ):

$$\tilde{C}_j^i(0,0,\tilde{z}) = C_j^i(0,0,z) - \epsilon_2 z \frac{\partial}{\partial x} C_j^i(x,y,z) + \epsilon_1 z \frac{\partial}{\partial y} C_j^i(x,y,z) + a_{i,k} a_{j,l} C_l^k(0,0,z), \quad (A.62)$$

where $C_j^i = \frac{\partial B_i}{\partial X_j}$ and the sum over k and l excludes the already accounted term where k=i and l=j. To use $\frac{\partial B_x}{\partial x}$ as an example we get:

$$\tilde{C}_1^1 = -\epsilon_2 z C_{1,1}^1 + \epsilon_2 C_3^1 + \epsilon_2 C_1^3 \qquad (A.63)$$

or

$$\frac{\partial B_x}{\partial x} = -\epsilon_2 z \frac{\partial}{\partial x} \frac{\partial B_x}{\partial x} + \epsilon_2 \frac{\partial B_x}{\partial z} + \epsilon_2 \frac{\partial B_z}{\partial x}. \qquad (A.64)$$

If one studies the components of Figures A.5 - A.7, one sees that the other eight terms of Equation A.62 are at least an order of magnitude smaller than the ones used in Equation A.64. Figure A.8 shows a comparison of $\frac{\partial B_z}{\partial x}$ with the terms in Equation A.64.

The understanding of the wrong-symmetry terms completes our understanding of the magnetic fit parameters and allows the fields shown in Figures A.5 - A.7 to be transformed into expansions that match Equations A.48 - A.50 for use in the Traces.
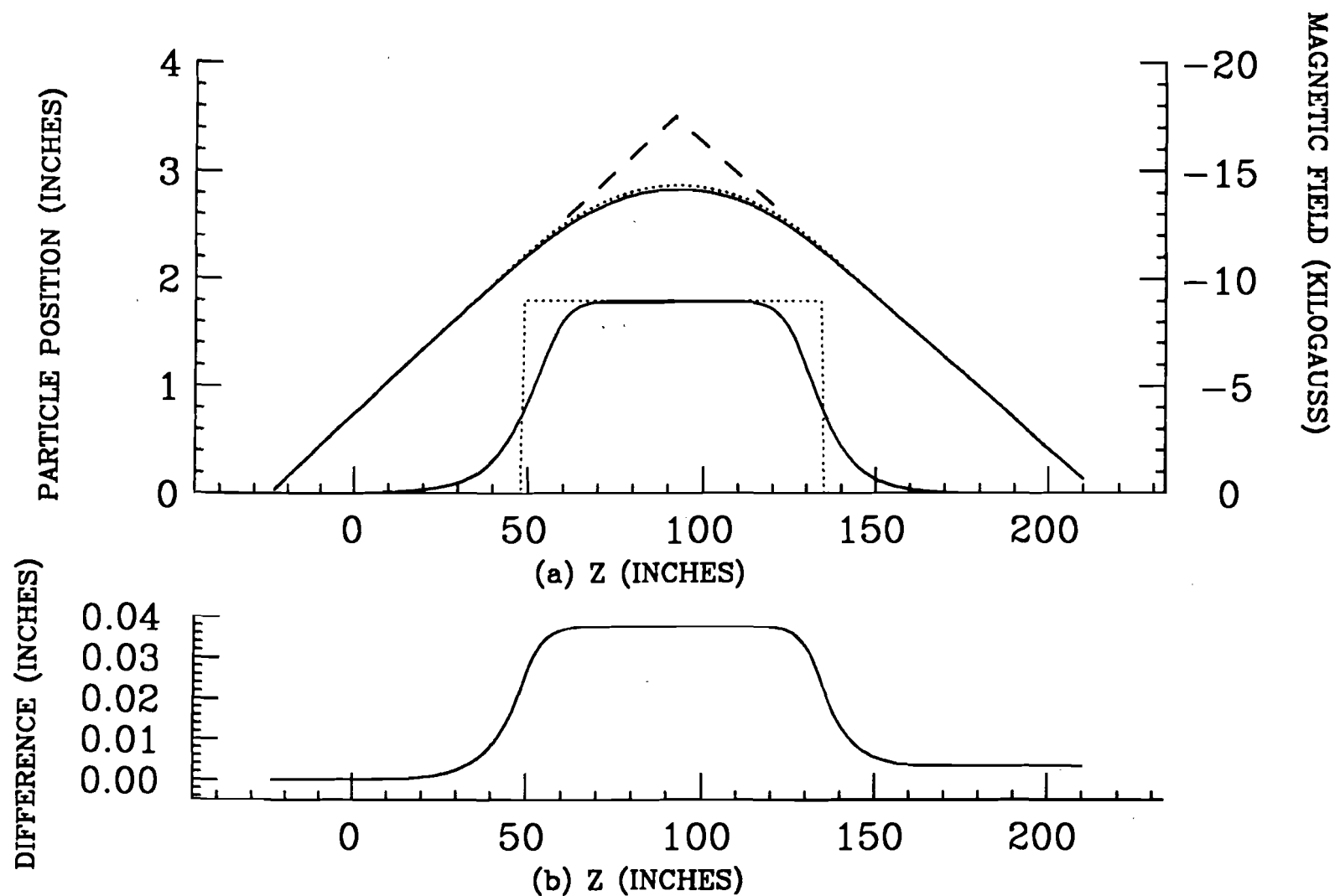
Figure A.1:   Comparison of Box Field to Quadratic Field Map

(a) shows the box and quadratic fields and the trajectories from both.

(b) shows the difference in position between the two trajectories.

No Rotation
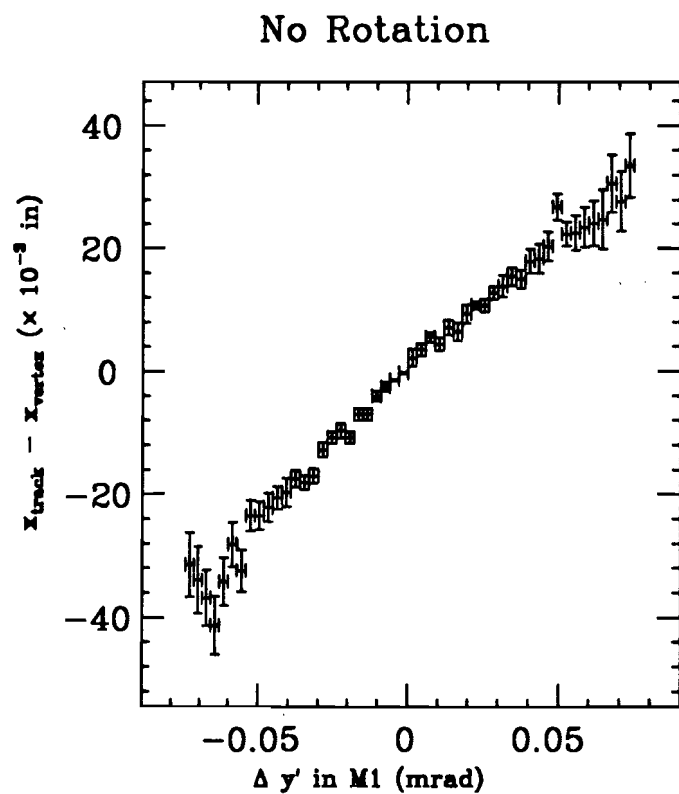
−8.7 mrad Rotation

slope gives −8.7 mrad rotation
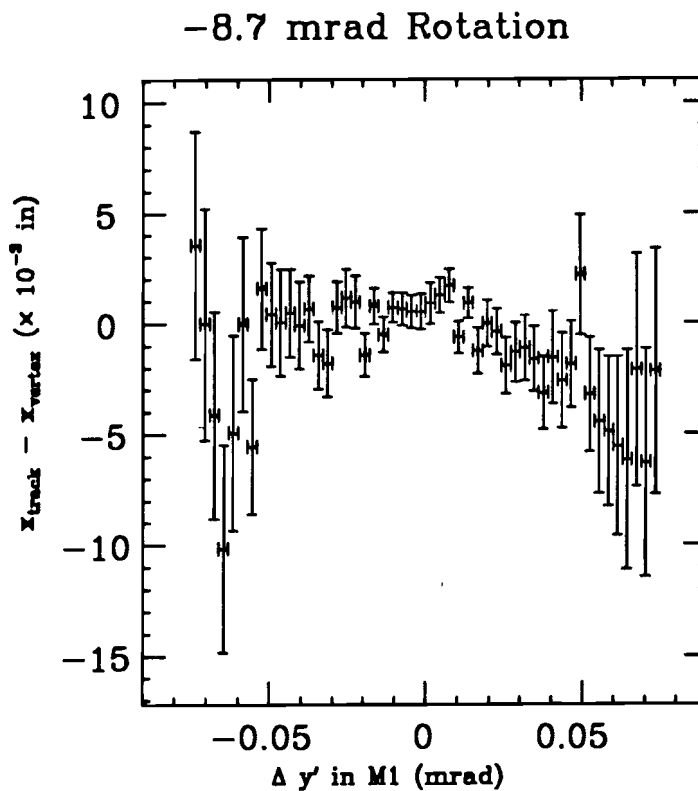
slope gives +.34 mrad overcorrection

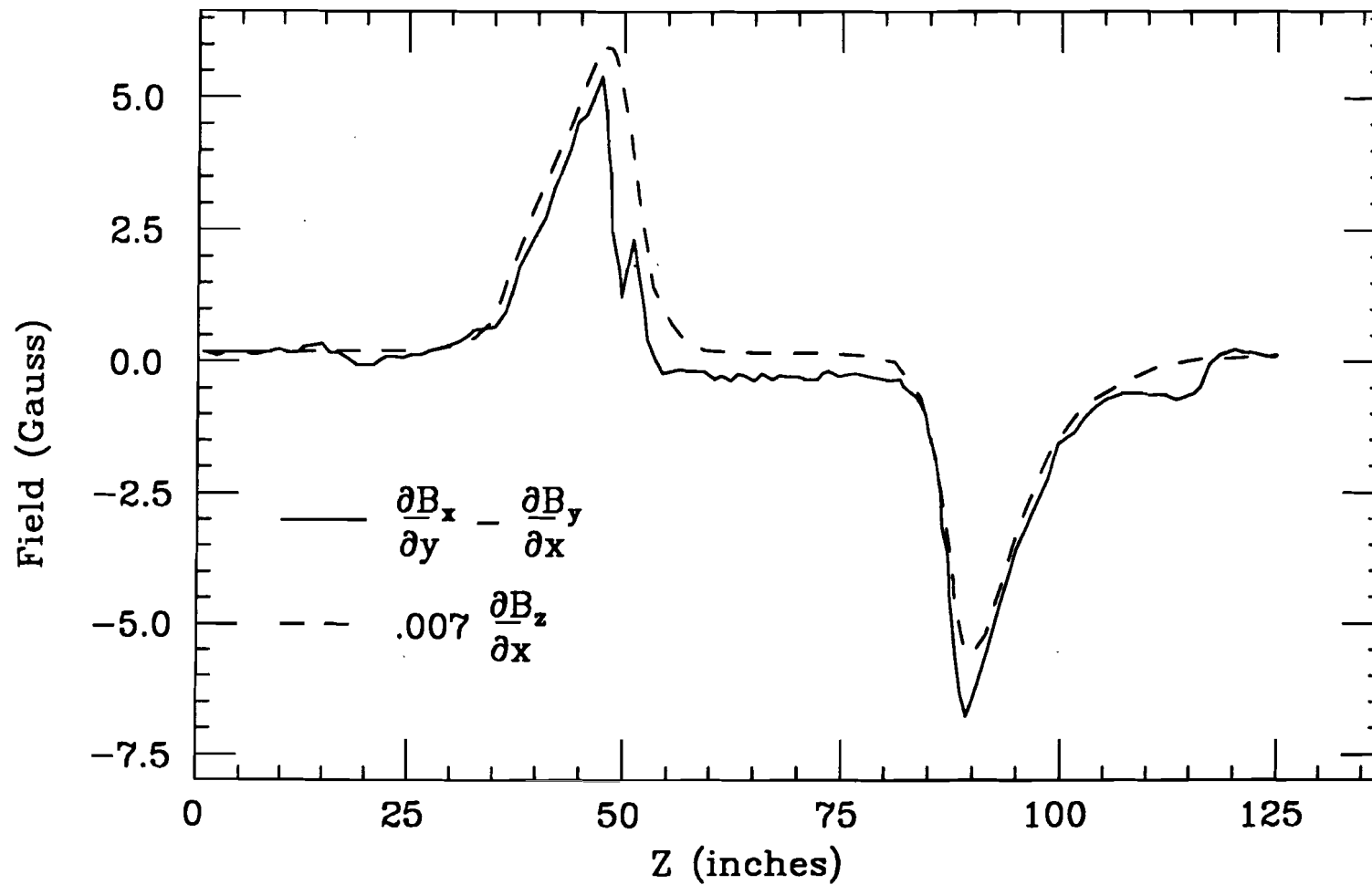Figure A.2: Determination of M1 Rotation

Comparison of Curl to B_z Leakage

Figure A.3: $\nabla \times B$ in M1

The solid line is the z-component of the curl equation for the B-field.

The dashed curve is $.007 \times \frac{\partial B_z}{\partial x}$ due to a rotation of the magnetic unit-vectors.

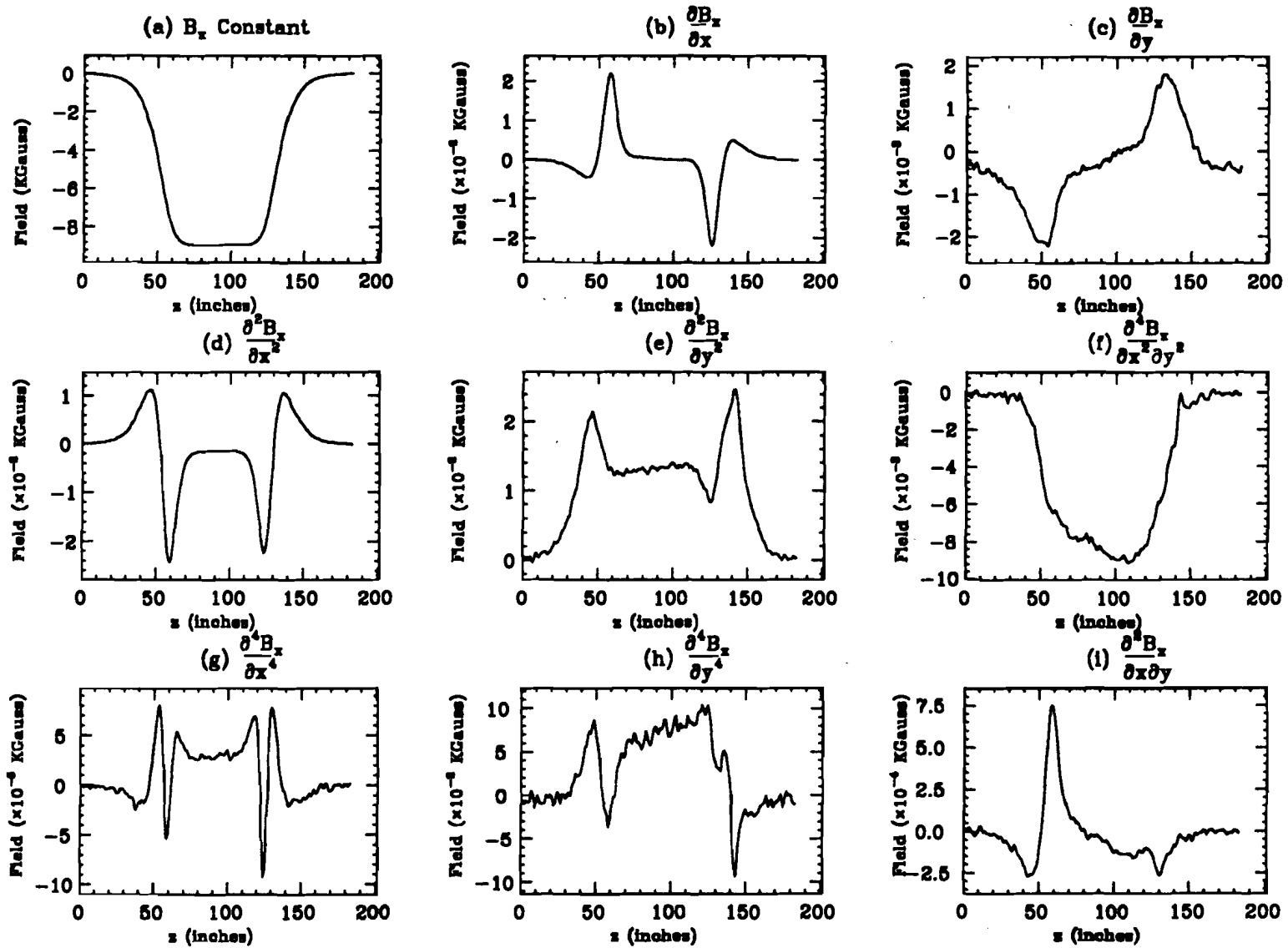# Comparison of Divergence to B_z Leakage
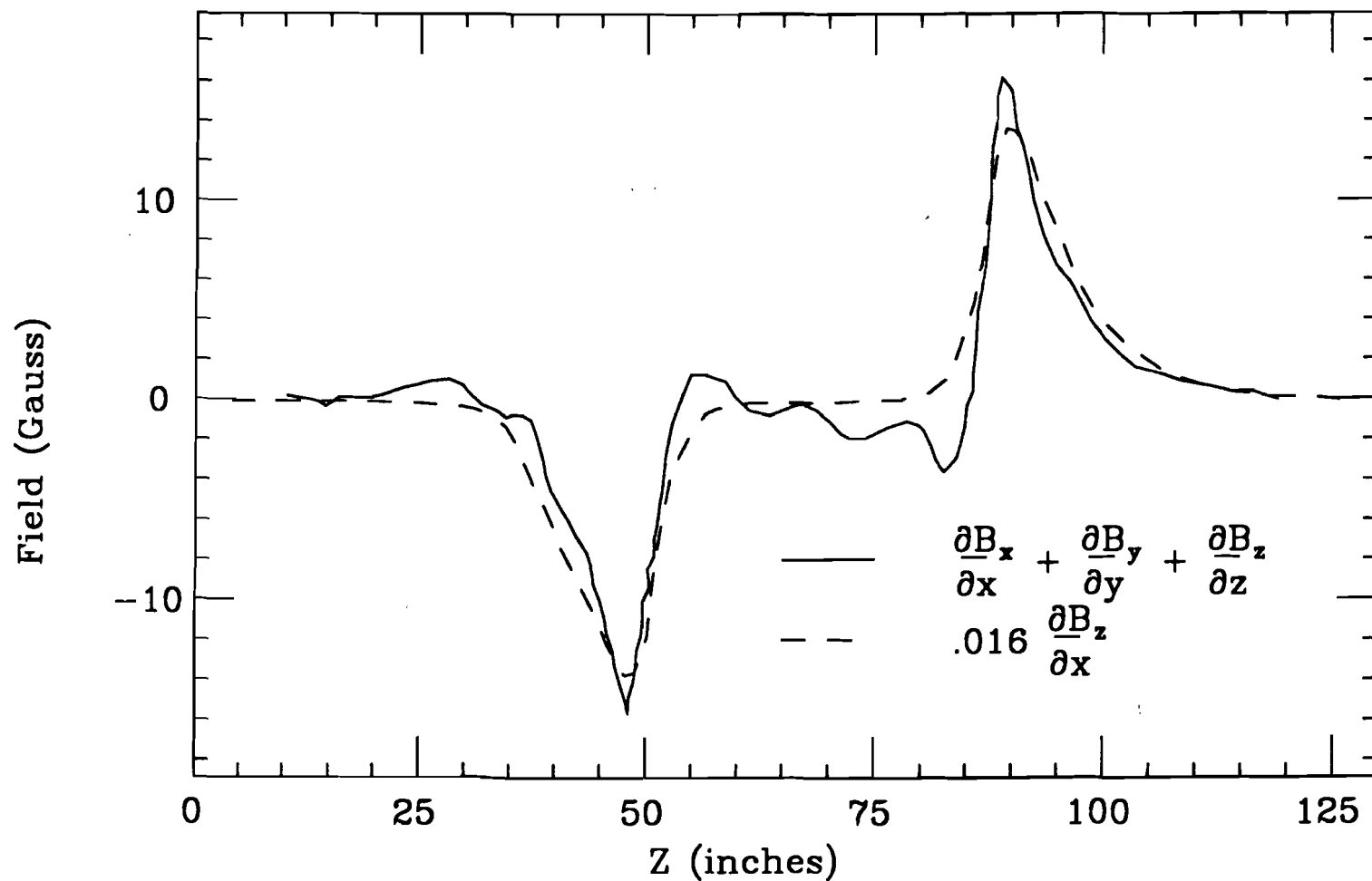
Figure A.4: $\nabla \cdot B$ in M1

The solid line is the divergence of the B-field.

The dashed curve is $.016 \times \frac{\partial B_z}{\partial x}$ due to a non-orthogonality of the magnetic unit-vectors.

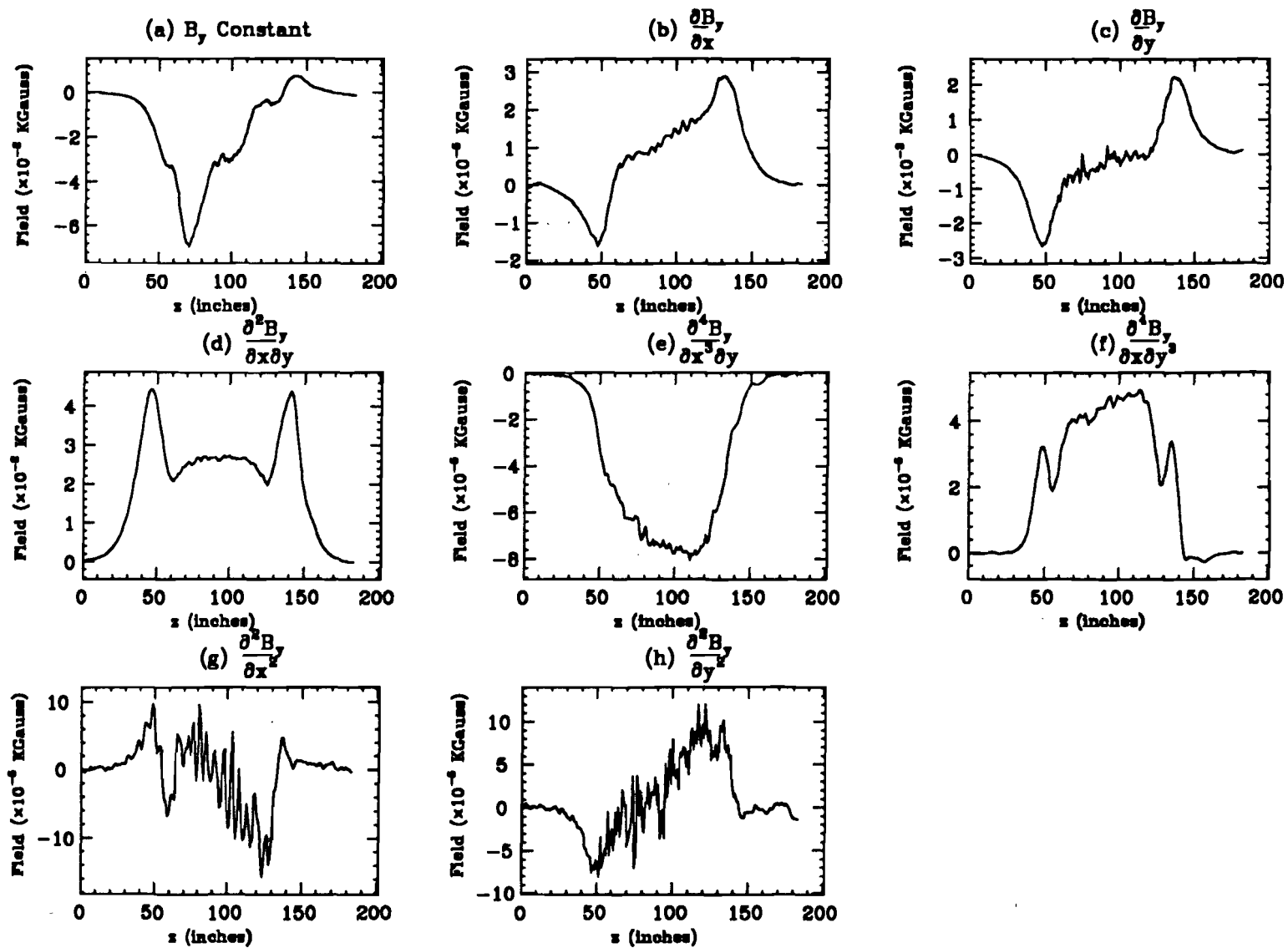Figure A.5: Components of B_x from Quadratic Field Map

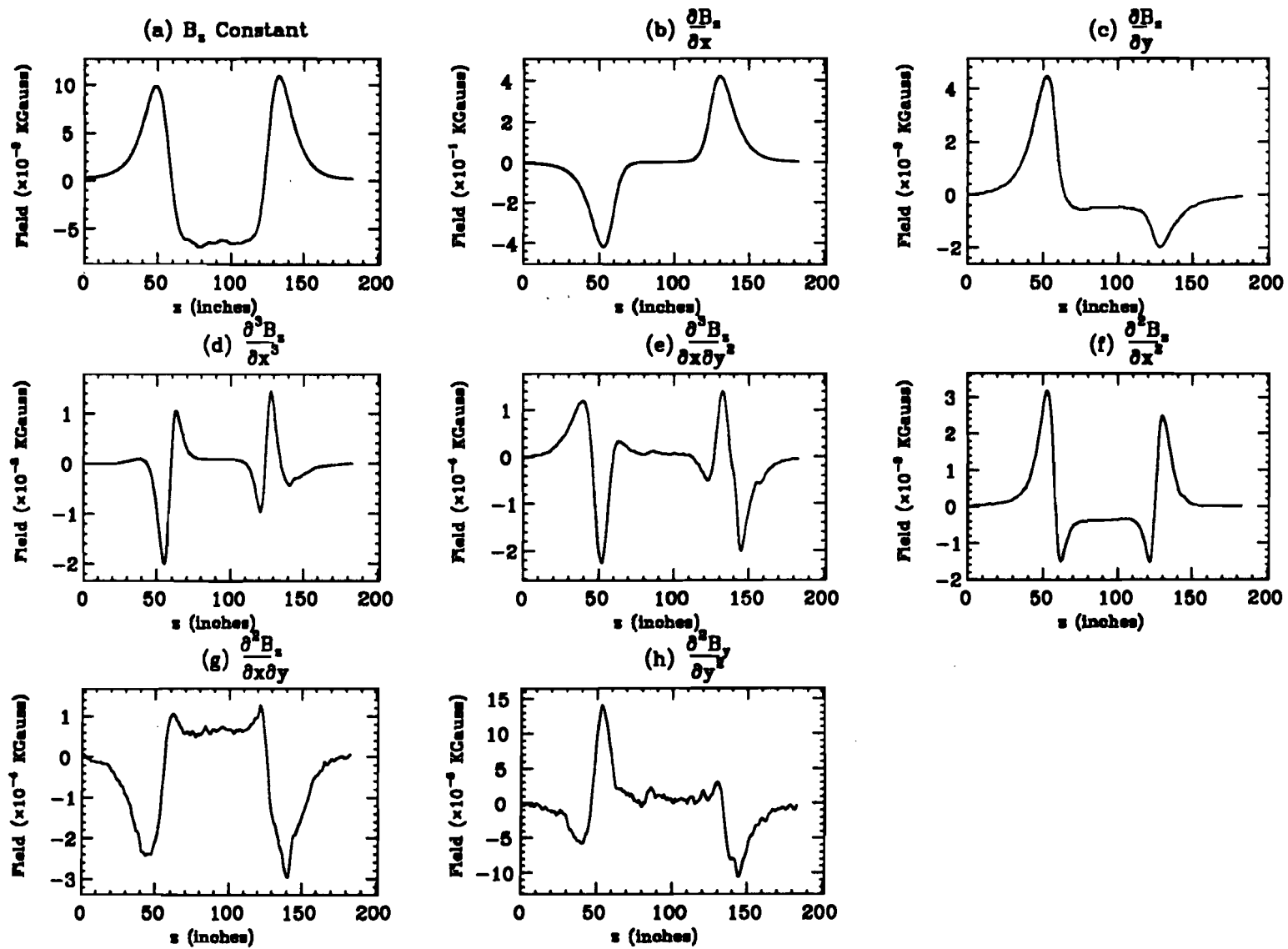Figure A.6:   Components of B_y from Quadratic Field Map

Figure A.7: Components of B_x from Quadratic Field Map

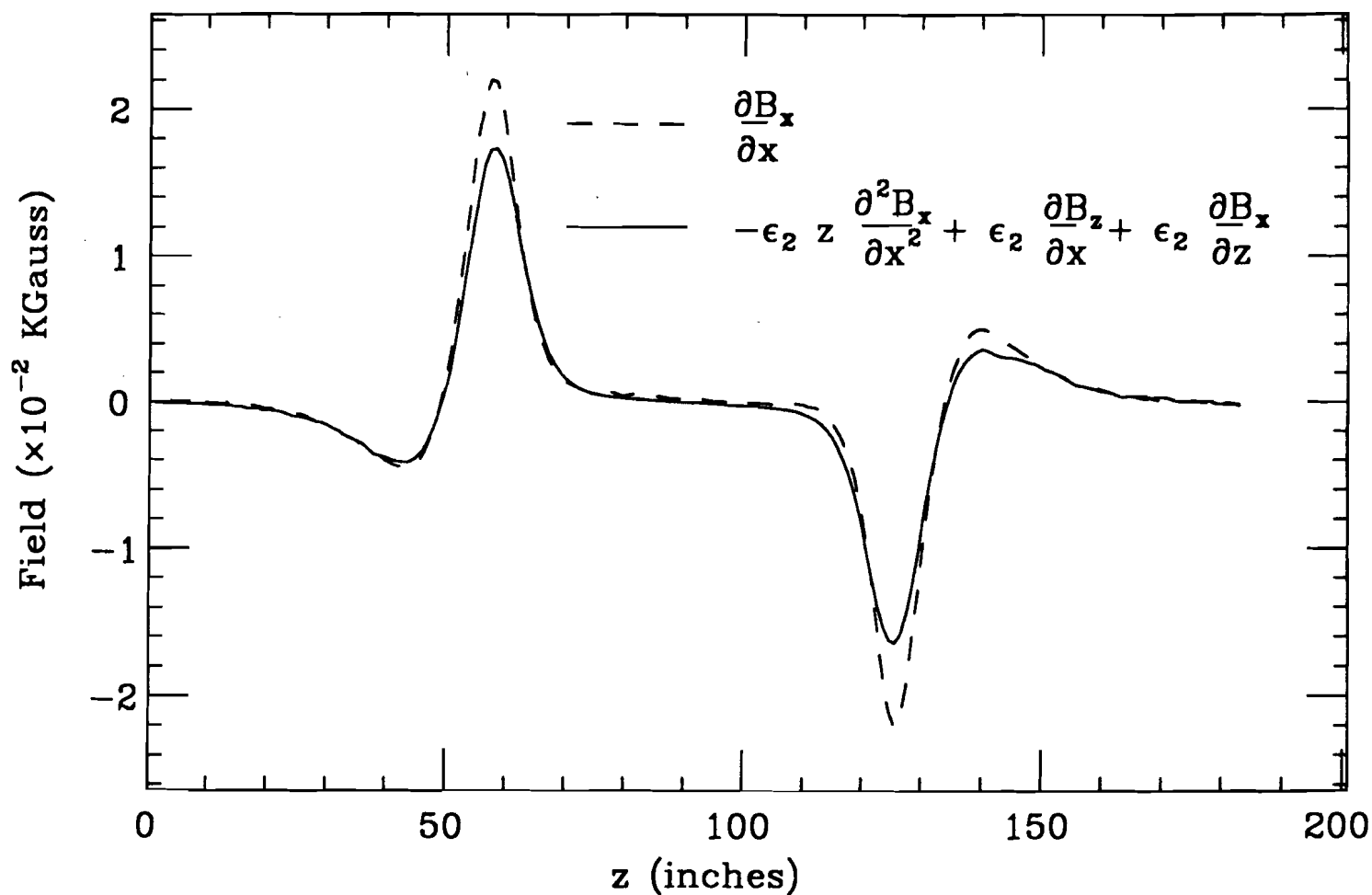# Elimination of $\frac{\partial B_x}{\partial x}$

Figure A.8:   Elimination of $\frac{\partial B_x}{\partial x}$

The dashed curve is $\frac{\partial B_x}{\partial x}$ found in the quadratic expansion of the B-field.

The solid line shows that $\frac{\partial B_x}{\partial x}$ can be explained as a result of the translations

and rotations mentioned in the text.

Appendix B: Cross-section Calculation

This Appendix describes the luminosity factors used in converting a sample of detected charm events into a cross-section and describes the M7 parameterization. Of particular importance is the calculation of the "effective" inelastic cross-section to account for the composition of the Experimental Target.

B.1 Luminosity Factors

In E400, cross-sections are measured by computing the ratio of the charm particle yield to the yield of relatively unbiased inelastic neutron events after appropriately correcting for efficiencies and the effects of analysis cuts.

We can express the yield of two types of processes as:

$$Y_{ch} = \mathcal{L}\, \sigma_{ch} \qquad Y_{MG} = \mathcal{L}\, \sigma_{MG}, \tag{B.1}$$

which gives:

$$\sigma_{ch} = \sigma_{MG}\frac{Y_{ch}}{Y_{MG}}, \tag{B.2}$$

where Y represents the yield of events, $\mathcal{L}$ is the luminosity of beam neutrons, and σ is the cross-section for either a specific charm state (ch) or Master Gate events (MG).

This section will describe how the three quantities on the right hand side of Equation B.2 were calculated. Briefly: Y_{ch} is the detected number of charm events scaled by the detection efficiency, Y_{MG} is the detected number of triggers scaled by the triggering efficiency, and σ_{MG} is the cross-section for such trigger events occurring which has been corrected for the makeup of our target.

B.1.a Master Gate Cross-section

E400 had a target composed of three different elements, tungsten, silicon, and beryllium in the target area. Since the interactions we investigated were between nucleons and elements other than hydrogen, the nucleons that surround the target nucleon affected the interaction in a manner that is not completely understood. We attempted to correct for it as best we could.

In the absence of acceptance effects, the yield of inelastic neutron events for the i'th target segment (Y_i^{in}) is:

$$Y_i^{in} = N_n \ t_i \ \sigma_i^{in} \ \eta_i, \tag{B.3}$$

where N_n is the number of incident neutrons , t_i is the thickness of the i'th target segment , σ_i is the measured[41] inelastic neutron cross-section for the i'th target segment, and η_i is density of scatterers or nuclei per cm^3 for the i'th target segment. The density of scatters is given by the expression:

$$\eta_i = N_A \ \rho_i/A_i, \tag{B.4}$$

where ρ_i is the mass density of target segment, A_i is the atomic weight, and N_A is Avogadro's number. Combining Equations B.3 and B.4 we have for the total inelastic yield:

$$Y^{in} = N_n \ N_A \ \sum_i \frac{\sigma_i^{in} \ \rho_i \ t_i}{A_i}. \tag{B.5}$$

A very similar expression would hold for the yield of charmed particles if one replaced:

$$\sigma^{in} \rightarrow \sigma^{ch} \ A_i^{\alpha}, \tag{B.6}$$

where σ^{ch} is the charmed cross-section per nucleus which we assume scales as A^{α}. Hence:

$$Y^{ch} = N_n \ N_A \ \sigma^{ch} \ \sum_i \rho_i \ t_i \ A_i^{(\alpha-1)}. \tag{B.7}$$

Taking the ratio of the charm to unbiased inelastic yields we get:

$$\frac{Y^{ch}}{Y^{in}} = \sigma^{ch} \ \frac{\sum_i \rho_i \ t_i \ A_i^{(\alpha-1)}}{\sum_i \sigma_i^{in} \ \rho_i \ t_i/A_i}. \tag{B.8}$$

Rearranging Equation (B.8) we obtain:

$$\sigma^{ch} = \sigma^{eff} \ \frac{Y^{ch}}{Y^{in}}, \tag{B.9}$$

where σ^{eff} is given by the expression:

$$\sigma^{eff} = \frac{\sum_i \sigma^{in} \ \rho_i \ t_i/A_i}{\sum_i \rho_i \ t_i \ A_i^{(\alpha-1)}}. \tag{B.10}$$

This "effective" cross-section would equal the total inelastic cross-section per nucleon at high A (roughly 40 mb for elements beyond hydrogen) if charm had the same A-

dependence as the total inelastic cross-section namely $\alpha \approx .71$. However, as Figure B.1 shows, there is considerable variation in σ^{ff} as a function of α, given the target configuration of E400.

B.1.b Master Gate Yield

A number of hardware efficiencies need to be taken into account to compensate for various elements of the trigger. These are the Master Gate, the livetime, the Si33, and the neutron spectrum.

The Master Gate was determined by the coincidence of hits in the T counter and the H×V array. The probability of these counters firing is dependent on their efficiency, the probability of the inelastic cross-section going into a given multiplicity, and the momentum of the particles. In this analysis it has been assumed that the scintillator efficiency is 100%.

If we assume that each particle has an independent probability ($\mathcal{P}$) of firing the H×V array, the master gate efficiency is:

$$\epsilon_{MG} = \frac{\sum_{N=2}^{\infty}\left(1 - (1-\mathcal{P})^N - N\mathcal{P}(1-\mathcal{P})^{(N-1)}\right)\sigma(N)}{\sum_{N=2}^{\infty}\sigma(N)}, \qquad (B.11)$$

where N is a given multiplicity and $\sigma(N)$ is the inelastic p-p cross-section with N charged tracks. The topological cross-section for inelastic hadronic events has been found to be $\sigma_T = 33.6$ mB[41]. (This measurement was for p-p interactions. The interactions studied here are n-A and so could easily vary by 10%.) To find $\mathcal{P}$, we assumed that the secondary particles are uniformly spread in rapidity ($y = \ln(\frac{2E}{M_\perp})$) which gives:

$$\mathcal{P} = \frac{1}{2}\frac{y(625) - y(9)}{y(625) - y(CoM)}, \qquad (B.12)$$

where 625 Gev is the average maximum energy of a secondary (the peak of the energy spectrum), 9 Gev is a typical lower energy for a charged track to strike the H×V array, and CoM represents the lab energy of a secondary at rest in the overall center-of-mass. Assuming $< M_\perp > = 0.205$ Gev (i.e. pions with $P_\perp$ of 150 Mev), $\mathcal{P} = 0.41$.

Using the above analysis and Monte Carlo studies it was determined that the Master Gate efficiency (ϵ_{MG}) is 0.85 ± 0.15.

The live-time of the trigger, ϵ_{lt}, varied with the rate at which a spill took place. The live-time was monitored by the Trigger Electronics and its value for a run was saved on the magnetic tape. The live-time is dependent on exactly which data runs are used but is typically around 0.45. The actual number of Master Gate (Y_{MG}) events was similarly recorded.

An analysis of Pin 2 events with multiplicity greater than 3 determined that the efficiency of the Si33 busline, ϵ_{Si33}, was 0.654. As mentioned in section II.D.1.c, a component of the trigger was that there be a minimum amount of energy deposited in the calorimetry outside a two inch hole along the beam axis. This energy cut corresponded to a requirement that the beam neutron have an energy greater than 300 Gev. Given the shape of the neutron spectrum (Fig. III.4), we were sensitive to 82% of the total spectrum which is symbolized by ϵ_{ns} of Equations IV.5 and B.13.

B.2. M7 Parameterization

The M7 efficiency, ϵ_{M7}, is a function of the particle types, and their energies, that comprised an event. A study of the M7 response was done using Pin 2 (unbiased data) events to categorize the probability of accepting an event according to the momentum range and Čerenkov identification of pions and "heavies" (kaons and protons). Table B.1 shows the parameterization which gives the probability of firing the M7 as a function of the number of tracks in each of the categories. Figure B.2.a shows a comparison of the result of the parameterization with the measured trigger fraction. The slight deviation from one-to-one correspondence is eliminated when the multiplicity is restricted to be less than 16 in Figure B.2.b. The efficiency loss at high multiplicity is probably due to limitations in the Čerenkov algorithms' ability to identify particles in a high multiplicity environment as opposed to a failure of the efficiency parameterization. The probability of satisfying the M7 is assumed to be independent for each track which is seen to be true in Figure B.2.c. The actual trigger fraction in the Pin 2 data matches well with the result of the parameterization, independent of the number of heavy particles in the event.

B.3 Conclusion

Putting all these components together (including ϵ_{MC} from Section IV.C.2) one gets:

$$\sigma_{ch} = \frac{\sigma_{eff} \cdot Y_{ch} \cdot \epsilon_{MG}}{Y_{MG} \cdot \epsilon_{lt} \cdot \epsilon_{M7} \cdot \epsilon_{MC} \cdot \epsilon_{Si33} \cdot \epsilon_{ns}}. \tag{B.13}$$
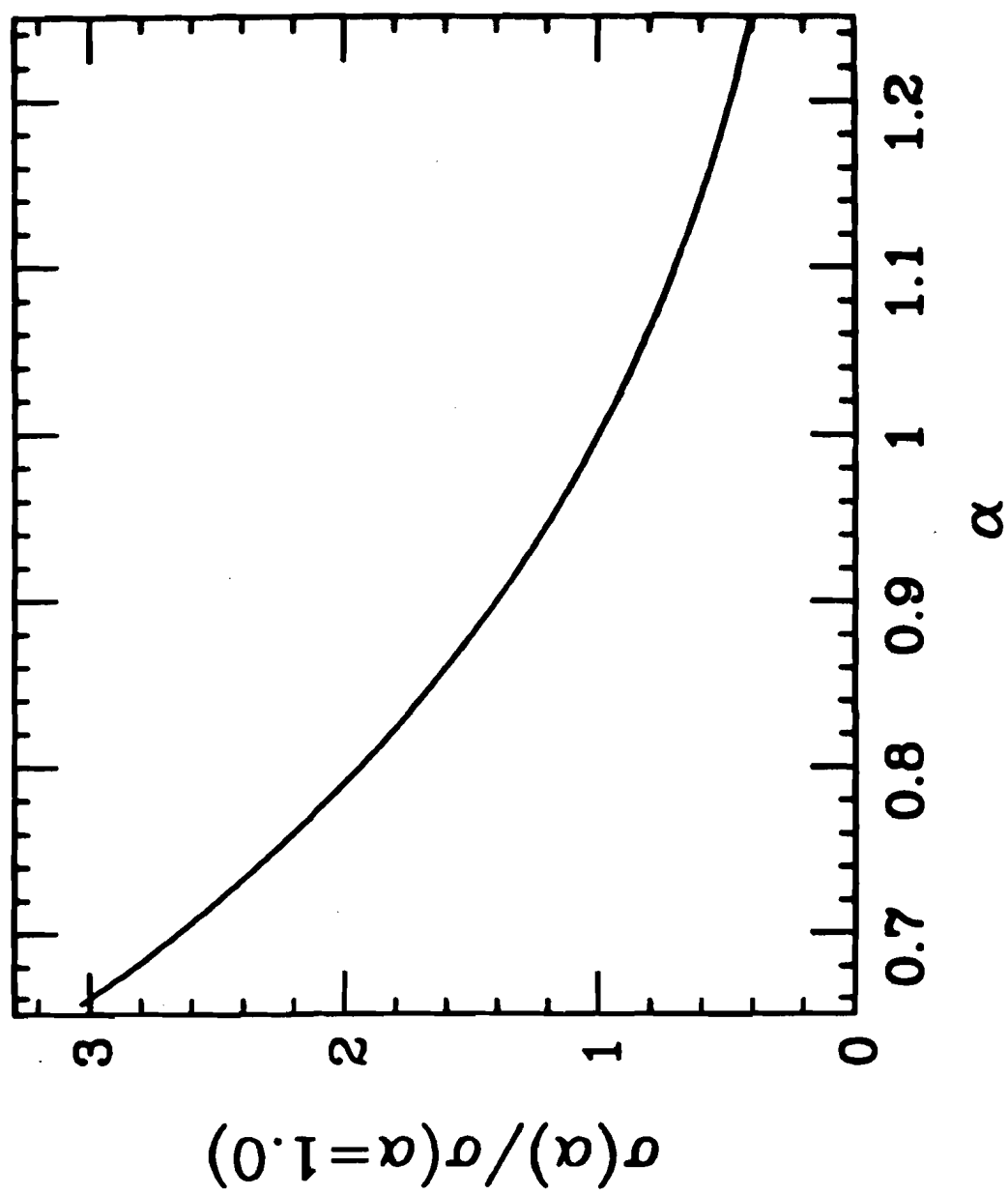
Figure B.1: Variation of σ^{eff} as a function of α

Analysis of M7 Parameterization

(a) Pin 2 Data

Slope = .952
Intercept = -.0012

(b) Pin 2 Data, Mult < 16

Slope = 1.01
Intercept = -.0084

(c)

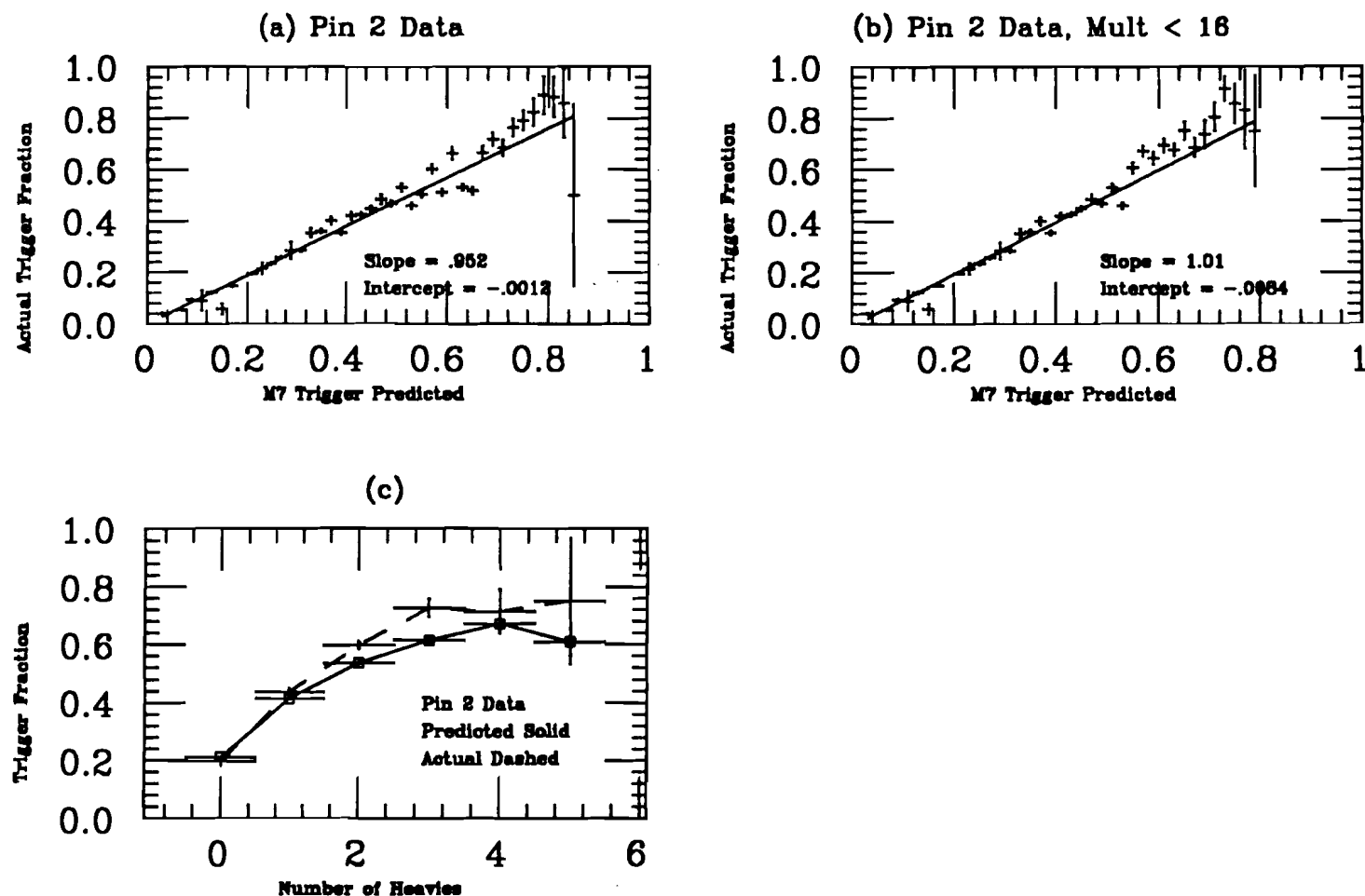Pin 2 Data
Predicted Solid
Actual Dashed

Figure B.2: Analysis of M7 Parameterization

(a) and (b) compare actual and predicted trigger fractions.

(c) compares actual and predicted trigger fractions as a function of the heavy particle multiplicity.

Table B.1

Parameterization of M7 Efficiency

- individual probabilities of satisfying M7 trigger are denoted p_i.

- total probability of satisfying M7 trigger by N_i particles of type i is:

$$P_{M7} = 1 - \prod_{i=1,5} (1 - p_i)^{N_i}$$

i	Čerenkov Id	Momentum	p_i
1	K_{def}	P > 21 Gev	0.33
2	K/P_{ambig}	10 < P < 25 Gev	0.082
3	K/P_{ambig}	P > 25 Gev	0.29
4	P_{def}	P > 40 Gev	0.25
5	all other*	0 < P < ∞	$0.03 + 0.00125 \times N_5$

* all other particles are considered pions:

$$N_5 = N_{tot} - \sum_{i=1,4} N_i$$

Table B.1:   Parameterization of M7 Efficiency

Appendix C:
The Correlated Impact Parameter Fit[30]

The decay of the D^0 meson has a $c\tau$ of 0.013 cm. With a resolution of 70 μm in x and y and .125 cm in z the E400 spectrometer could not see the decay distance of a D^0 decay on an event by event basis. However this section will show that on a statistical level, a resolution of $c\tau = .005$ cm could be achieved which enabled us to identify a sample of events that had a finite lifetime over its zero lifetime background.

If we look a charmed state decaying into n charged tracks at a distance L from the primary vertex (as measured in the lab frame). The ith track emerging from the decay is predicted to have signed impact parameters in X and Y (see Fig. C.1) given by:

$$\Delta X^i = L \left[\frac{P_x^{Ch}}{P^{Ch}} - \left(\frac{P_z^{Ch}}{P^{Ch}} \right) \frac{P_x^i}{P_z^i} \right] \tag{C.1}$$

$$\Delta Y^i = L \left[\frac{P_y^{Ch}}{P^{Ch}} - \left(\frac{P_z^{Ch}}{P^{Ch}} \right) \frac{P_y^i}{P_z^i} \right], \tag{C.2}$$

where P^{Ch} is the momentum of the charmed state and P^i is the momentum of the ith track. Although the exact expressions above were used in the algorithm written for the fit described below, a simple, approximate form for the impact parameters is given for small opening angles as

$$\Delta X^i \simeq L \cdot \theta_x^i \tag{C.3}$$

$$\Delta Y^i \simeq L \cdot \theta_y^i, \tag{C.4}$$

where θ^i is the opening angle between the ith track and the charmed particle (in the lab frame).

Now we look at n tracks of unknown origin (possibly charm). The measured X and Y impact parameters can be represented as ΔX_*^i and ΔY_*^i. Then the best value of

L (denoted as L_*) for this potential charmed state is determined by minimizing a χ^2 defined as:

$$\chi^2(L) = \sum_{i=1}^{n} \left[\left(\frac{\Delta X^i(L) - \Delta X_*^i}{\sigma_x} \right)^2 + \left(\frac{\Delta Y^i(L) - \Delta Y_*^i}{\sigma_y} \right)^2 \right], \qquad (C.5)$$

where σ_x and σ_y are the transverse position errors. Throughout the analysis for this thesis, the n tracks from the D^0 candidate were excluded from the fit that found the primary vertex. Let us denote $\chi^2(L_*)$ as χ_*^2 and $\chi^2(L = 0)$ as χ_o^2 . If this is a charm decay, χ_*^2 will tend to be smaller than χ_o^2 . Real charmed particle decays will favor $L_* > 0$ and small χ_*^2 . These particles are at ultra-relativistic energies, so L_* is essentially proportional to the lab momentum of the charmed particle and a direct cut on L_* will require an unnecessary momentum dependent efficiency correction. Working with the proper decay length, $\frac{L_*}{\gamma}$, would remove this momentum bias as would using $\frac{L_*}{\sigma_L}$ where σ is the anticipated error on the decay length L_*. Neglecting the errors on the Z of the primary vertex (which are typically 50 mills ,or about 1300 μm, as shown in Appendix D), the value of σ is given by the expression:

$$\frac{1}{\sigma} \equiv \sqrt{\sum_{i=1}^{n} \left(\frac{\theta_x^{i\,2}}{\sigma_x^2} + \frac{\theta_y^{i\,2}}{\sigma_y^2} \right)}. \qquad (C.6)$$

Note that for a given charmed particle decay configuration (in the charmed particle center-of-mass frame) the angles θ_x^i and θ_y^i scale as $1/P$ where P is the lab momentum of the charmed state. For this reason, a cut in $\frac{L_*}{\sigma_L}$ is essentially equivalent to a cut in $\frac{L_*}{\gamma}$ when one averages over all possible decay configurations, and is thus essentially momentum independent as well. The advantages of an $\frac{L_*}{\sigma_L}$ cut is that the significance of the vertex detachment is correctly computed for each separate decay configuration as well as for the average decay configuration.

The demand that the secondary vertex for a charmed particle candidate must be significantly downstream of the primary vertex is usually accompanied with the demand that the tracks comprising a candidate converge into a reasonable secondary vertex based on χ_*^2 . This cut tends to eliminate possible background vertices which include badly

measured tracks, and tracks which are part of neutral V^0's. Algebraic manipulation of equations C.5 and C.6 gives:

$$\chi_*^2 = \chi_o^2 - \left(\frac{L_*}{\sigma}\right)^2.$$

$$\text{(C.7)}$$

To improve signal to background, one can demand that χ_*^2 be small and that $\frac{L_*}{\sigma_L}$ be positive (since negative lifetimes are obviously dominated by background) and relatively large. This expression for χ_*^2 shows that a stiff cut on $\frac{L_*}{\sigma_L}$ will insure that χ_*^2 is considerable smaller than χ_o^2 , i.e., the tracks "prefer" originating from the secondary vertex.

For the algorithm used in this dissertation, the transverse errors for full tracks and stubs were the same. The x and x errors were determined from the data in a fit to the form given in Equation D.6. One can use this measurement of the transverse position error to determine the anticipated resolution on the proper lifetime of the charmed state. The proper lifetime of a charmed particle decay is given by:

$$\tau = \frac{ML_*}{cP},$$

$$\text{(C.8)}$$

where M is the mass of the charmed state and P is its momentum. Differentiating equation C.8 gives:

$$\sigma_\tau = \frac{M}{c}\frac{\sigma_L}{P}.$$

$$\text{(C.9)}$$

A plot of σ_L versus P for $D^0 \rightarrow K\,\pi$ gives $\sigma_\tau = .18$ psec.

These results can be checked. Using the expression for the error on L_* we see:

$$\sigma_\tau = \frac{M\sigma_{x,y}}{cP\,\Theta} \quad \text{where} \quad \Theta = \sqrt{\sum_{i=1}^{n}\left(\theta_x^{i\,2} + \theta_y^{i\,2}\right)}.$$

$$\text{(C.10)}$$

In the decay $D^0 \rightarrow K\,\pi$, the two daughters each carry 861 Mev and simple geometry says that $P\Theta$ is ≈ 2.4 Gev. Assuming $\sigma_{x,y} = 2.8$ mills gives $\sigma_\tau = 0.18$ psec. Therefore the data matches the theoretical resolution.
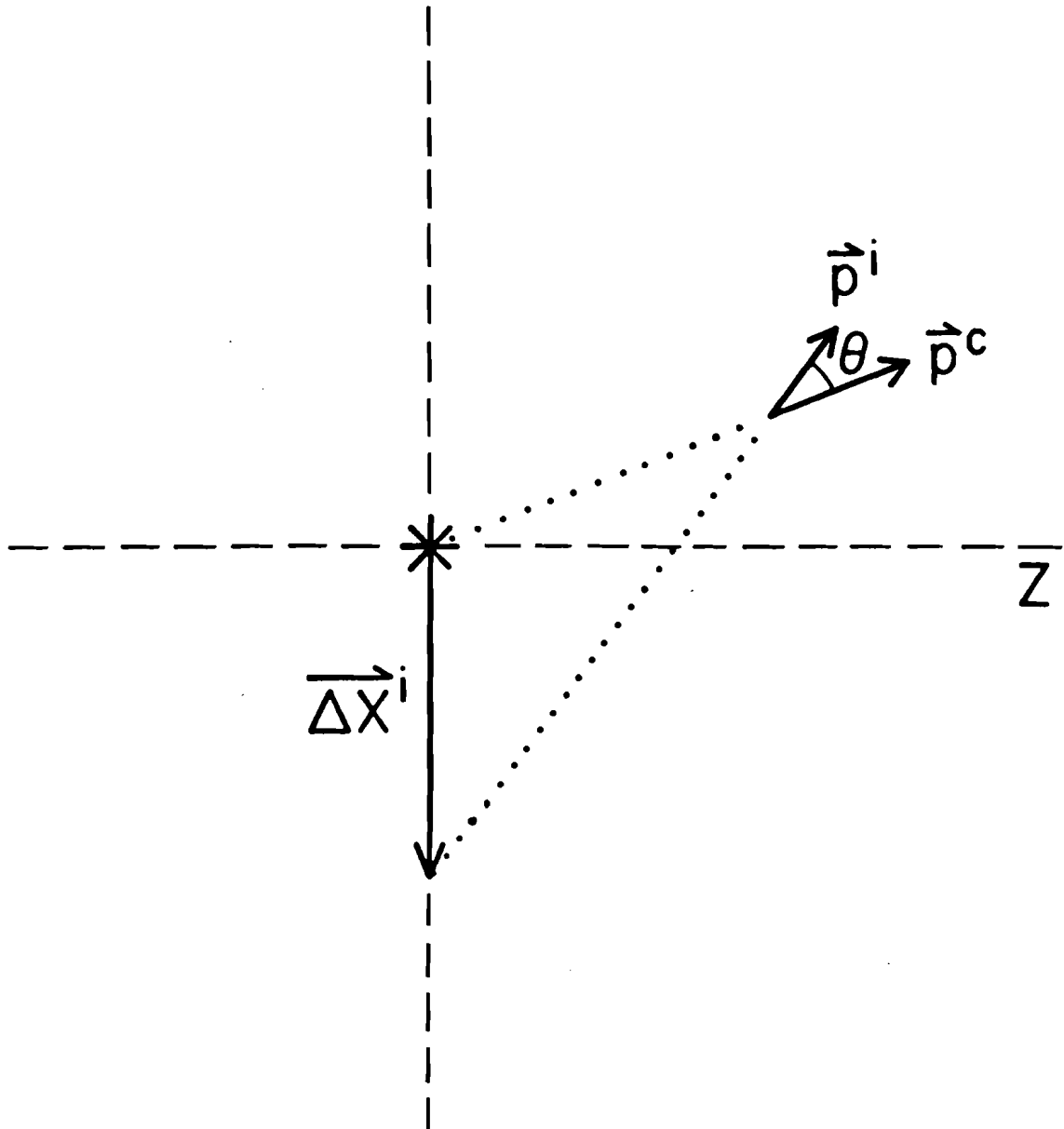
Figure C.1   The impact parameter,ΔX^i, of the ith
track emerging from a charm state decay.

Appendix D:
Determination of the Transverse Position Error[30]

The ability of the vertex chamber to "tag" charmed particles by their short but finite lifetime can be characterized by the transverse position error, which is the error in X or Y when a track is extrapolated to a given Z location, say the center of a given target segment. These transverse errors are identified as σ_x and σ_y. This section begins by discussing the theoretical limits on σ_x and σ_y and compares these limits to the experimental determination of σ_x and σ_y. In Appendix C these measurements are used to compute the anticipated resolution on the proper lifetime for charmed states.

As described in section II.B.3, the wire spacing of the D5 is eight times finer than the wire spacing of the chambers of the main spectrometer. Hence the intercept resolution is essentially the position resolution of the 9 chamber planes of the D5. Conversely, the angular information provided by the main spectrometer is better by a factor of about 8 than the angular information provided by the D5 owing to the much longer length of the main spectrometer. Hence the angular resolution of full tracks and stubs is essentially the angular resolution of the main spectrometer. These considerations lead one to consider three sources of transverse position error:

1. Error in determining the intercept of the track with the D5 due to the D5 wire spacing.

2. Error from extrapolating the intercept of the track with the D5 center to the Z location of the primary vertex due to the main spectrometer angular error.

3. Error due to multiple coulomb scattering of the track from matter located between the D5 and the primary vertex.

For a single D5 plane with wire spacing W, the RMS error in a single coordinate is given by $\sigma = W/\sqrt{12}$. For a set of 3 D5 planes oriented at 0° and $\pm 60^o$, the expected X and Y errors can be shown to be $\sigma_x = \sigma_y = W/\sqrt{18}$. For three such sets one then expects:

$$\sigma_{ws} = \sigma_x = \sigma_y = W/\sqrt{54} = 1.34 \text{ mills,} \qquad (D.1)$$

where the D5 wire spacing is given as W = 9.85 mills (or 250μm). Multiple coulomb

scattering, adjacent wire hits and confusion in the D5 will seriously degrade the performance relative to these theoretical limits.

In order to reduce the effects of extrapolation errors, the D5 was placed as close as possible to the target assembly. By considering the wire spacing and positions of the chamber stations of the main spectrometer, typical angular errors of 50 μrad and 100 μrad are computed for full tracks and stubs, respectively. The distance from the most upstream target segment (tungsten) is 7 inches. Hence the transverse error due to trajectory extrapolation from the D5 is at most expected to be 0.7 mills. Including the effects of this error increases the theoretical limit to $\sigma_x = 1.6$ mills , $\sigma_y = 1.5$ mills for stubs and a nearly negligible increase for full tracks.

Multiple coulomb scattering of a track (with momentum P) passing through the slabs of matter which constitute the target assembly and detectors contributes a momentum dependent term to the transverse position error of the form

$$\sigma_x = \sqrt{\sigma_{ws}{}^2 + \frac{C_{ms}^2}{P^2}} \quad \text{where} \quad C_{ms} = 14 \text{ MeV} \sqrt{\sum_i \left(\frac{t_i}{X_i}\right)(Z_i - Z_v)^2}, \qquad \text{(D.2)}$$

where t_i/X_i is the thickness of a given slab in radiation lengths, Z_i is the position of the slab, and Z_v is the position of the primary vertex. In E400, the material between the tungsten target and the D5 results in $C_{ms} \approx 10$ mill GeV with a significant portion due to the material of the D5 itself. The effects of multiple coulomb scattering from matter downstream of the D5 will increase the value of C_{ms} but by an amount which is difficult to calculate since much of this matter is between planes of the main spectrometer. Hence much of the effect of this multiple scattering is compensated by the track fitting process.

However, an experimental measurement of the transverse extrapolation errors, σ_x and σ_y, can be made by examining the resolution on the Z of the primary vertex. The coordinates of the primary vertex are determined by minimizing the χ^2 given by the expression:

$$\chi^2 = \sum_i \frac{(x_i' Z_v + X_i - X_v)^2}{\sigma_x^2} + \frac{(y_i' Z_v + Y_i - Y_v)^2}{\sigma_y^2}, \qquad \text{(D.3)}$$

where the sum ranges over all tracks which are considered part of the primary vertex, x_i' and y_i' are the slopes of the i'th track (between M1 and M2), and x_i and y_i are the

intercepts of the track at some convenient reference plane (such as the bend center of M2). By forming $\frac{d^2\chi^2}{dZ_v^2}$ one computes that the error on Z_v ,(σ_{Z_v}), should be given by:

$$\sigma_{Z_v} = \frac{\sigma_{x,y}}{\sqrt{\sum_i \left(x_i'^2 + y_i'^2\right)}}, \qquad (D.4)$$

where a single error ($\sigma_{x,y}$) is assumed for all tracks and both X and Y projections.

By comparing the above primary vertex error expression to the observed Z_v distribution width, one can obtain an estimate for $\sigma_{x,y}$. The distributions for the tungsten and downstream Si triggering wafers are studied since they are extremely thin (with total lengths of 12 mills and 43 mills respectively). Monte Carlo calculations demonstrate that the effects of multiple coulomb scattering somewhat complicates the analysis of the primary vertex resolution. These calculations indicate that adding a term in quadrature with the value of σ_{Z_v} is necessary. Including a constant in quadrature implies that the true resolution will approach this constant even as the calculated error (as given by σ_{Z_v} in Equation D.4) approaches zero. A probable explanation for this effect is that primary vertices which are predicted to be very well resolved must include very wide angle stubs. Since hadroproduction is typified by limited $P_\perp$, the wide angle stubs must have very low momentum and must therefore have transverse position errors dominated by multiple scattering which has a 1/P dependence. Since for a given $P_\perp$, the stub production angle also has a 1/P dependence, the contribution of a given wide angle stub in reducing σ_{Z_v} approaches an upper limit typified by C_{ms} and $< P_\perp >$.

By including an additive term in quadrature, one can successfully predict the observed error in Z_v. Figure D.1.a shows the observed error in Z_v for the tungsten target. This figure compares the distribution of the normalized Z_v deviation (i.e., the deviation of Z_v from the nominal tungsten target center divided by the predicted error in the deviation) to a Gaussian distribution of unit (RMS) width shown by the solid curve. The agreement with a unit Gaussian distribution is impressive although there are non-Gaussian tails clearly visible when this data is histogrammed on a logarithmic scale as shown in Figure D.1.b. The value for the predicted error (σ_{pred}) used in Figures D.1.a or D.1.b consists of the calculated error from the slope of the tracks in the primary vertex (as given by Equation D.4) as well as a constant added in quadrature to take

into account finite target thickness, multiple scattering effects, etc. The predicted width expression used was:

$$\sigma_{pred} = \sqrt{\sigma_{Z_v}^2 + (28.6 \text{ mills})^2}, \tag{D.5}$$

where σ_{Z_v} was computed assuming $\sigma_{x,y} = 2.69$ mills.

The above predicted width expression was found using a constant transverse position error ($\sigma_{x,y}$), independent of track momentum. However, a Monte Carlo study reveals that the error in Z_v can be appropriately reproduced by assuming a momentum dependent transverse position error given by:

$$\sigma_{x,y} = \sqrt{(2.13 \text{ mills})^2 + (21 \text{ mill GeV/P})^2}. \tag{D.6}$$

Notice, the asymptotic resolution on $\sigma_{x,y}$ is thus roughly 30 - 40 % larger than the earlier calculated theoretical limit for the chamber assuming "perfect" data (i.e., no missing hits or adjacent wire hits).

Figures D.1.c and D.1.d show the normalized deviation for the three downstream triggering Si target segments using the identical constants for σ_{pred} as found for the tungsten target. The dashed curve is a Gaussian with an RMS width of 0.82 which indicates that the primary vertices in the triggering Si target segments are slightly better resolved than vertices in the tungsten. The improved resolution in the triggering Si target is probably due to a considerably reduced multiple coulomb scattering contribution and a much shorter extrapolation distance from the D5. To summarize – the analysis of the primary vertex width for the two thin targets indicates an effective transverse position error ranging from 2.20 to 2.69 mills (or 56 to 68 μm) depending on the target segment. Incidentally, the error on the primary vertex (in Z) is typically 50 mills (or 1300 μm).

An alternative method for investigating the magnitude of the transverse position error involves studying errors in the determining the secondary vertex for potential charm candidates using the correlated impact parameter fit described in Appendix C. To study the errors we plot L_*/σ for background candidates which presumably have no finite lifetime and hence a background L_*/σ plot represents nothing but resolution

effects. The anticipated error in the secondary vertex is related to the transverse position error in a manner highly analogous to the error in the primary vertex:

$$\sigma_Z = \frac{\sigma_{x,y}}{\sqrt{\sum_i \left(\theta_x^{i\,2} + \theta_y^{i\,2}\right)}} \qquad (D.7)$$

where θ_x^i , and θ_y^i are the angles of the given charm constituent track with respect to the total charmed particle momentum vector. Figure D.2.b shows the normalized deviation plot for background $D^0 \rightarrow K\,\pi$ candidates with momentum exceeding 100 GeV compared to a Gaussian distribution of unit RMS width. The normalized error which was computed using Eqn. D.7 with $\sigma_{x,y} = 2.8$ mills agrees very well with the unit Gaussian distribution giving additional support to this value for the effective transverse position error. Figure D.2.a shows the normalized deviation plot for background $D^0 \rightarrow K\,\pi$ candidates with momentum less than 50 GeV. The solid curve is a unit RMS width Gaussian while the dashed curve has an RMS width of 1.60. Clearly the P < 50 GeV candidates have a worse resolution on the secondary vertex than the P > 100 GeV candidates. This broadening of the resolution presumably reflects the effects of multiple coulomb scattering as well as the effects of the typically 50 mill resolution on the location of the primary vertex which is not taken into account in the anticipated secondary vertex error.
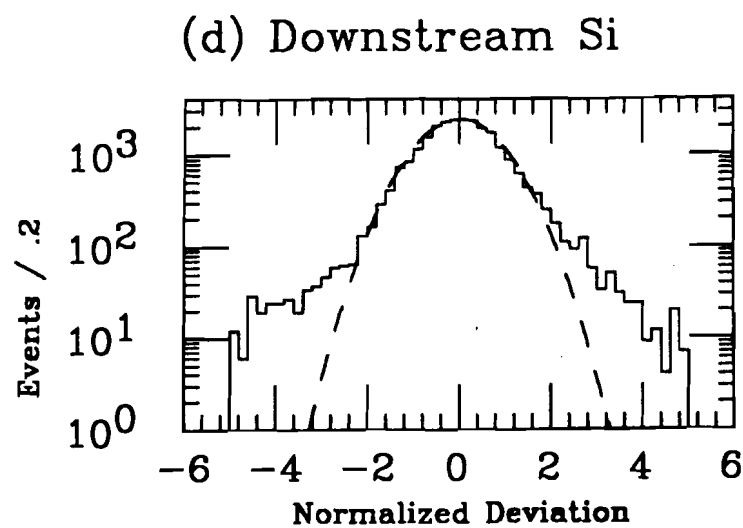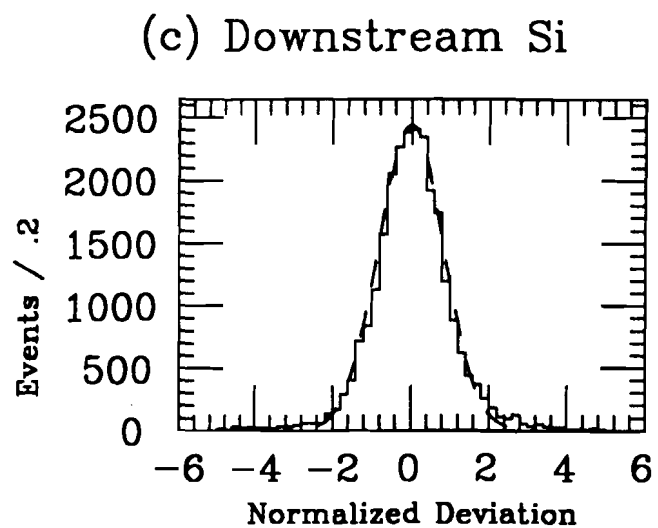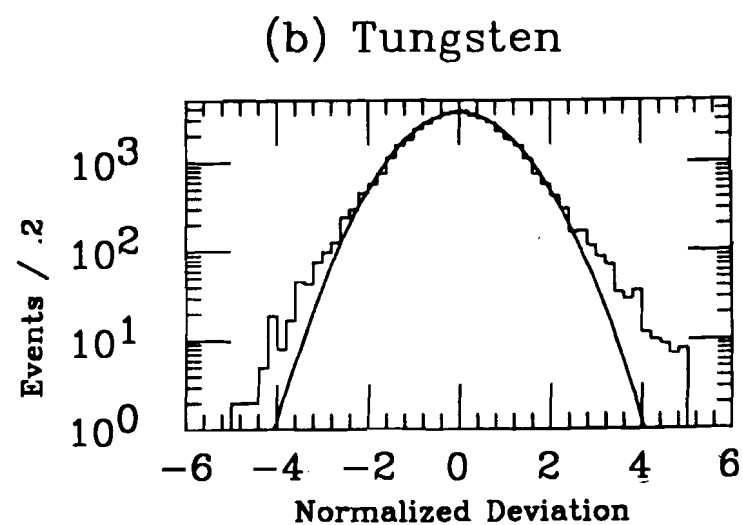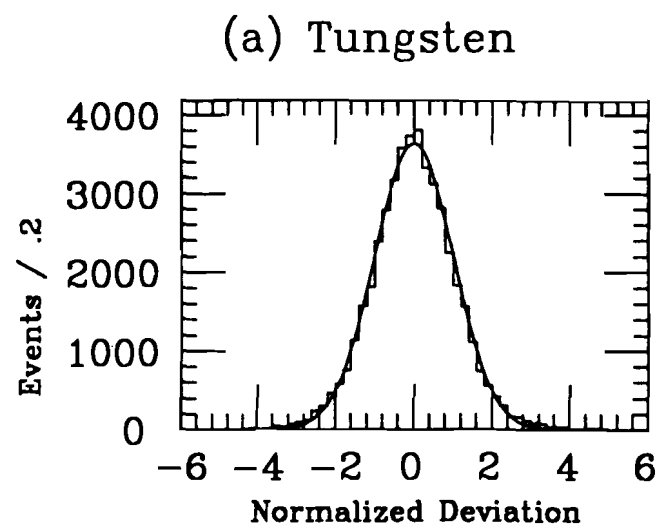
(a) Tungsten

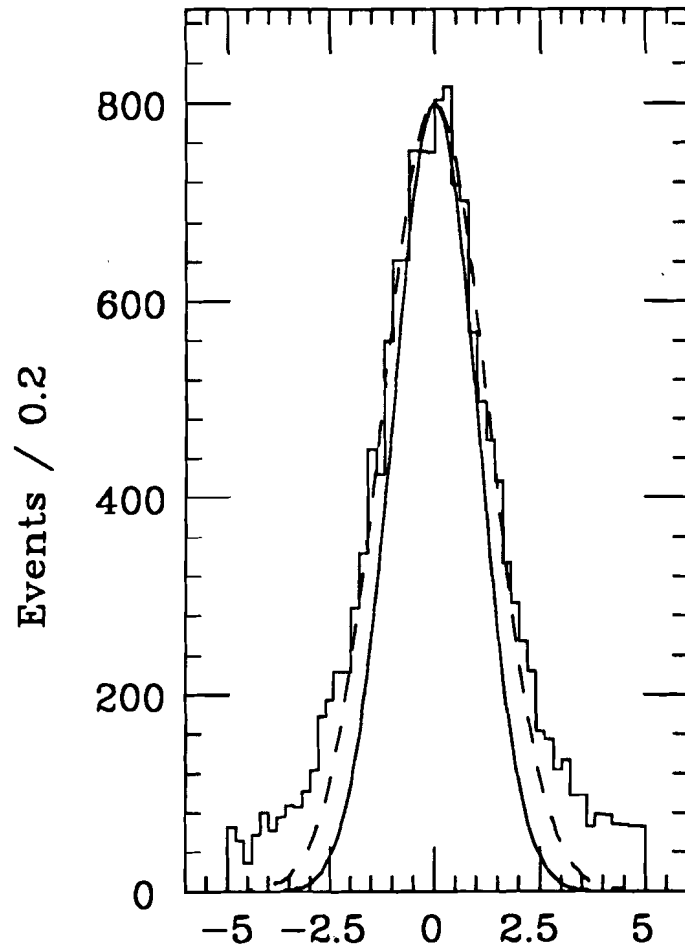## (b) Tungsten

(c) Downstream Si

(d) Downstream Si

Figure D.1:   The observed error in Z_v is compared
to a unit Gaussian, (a) and (b), and .82 times a unit Gaussian, (c) and (d).

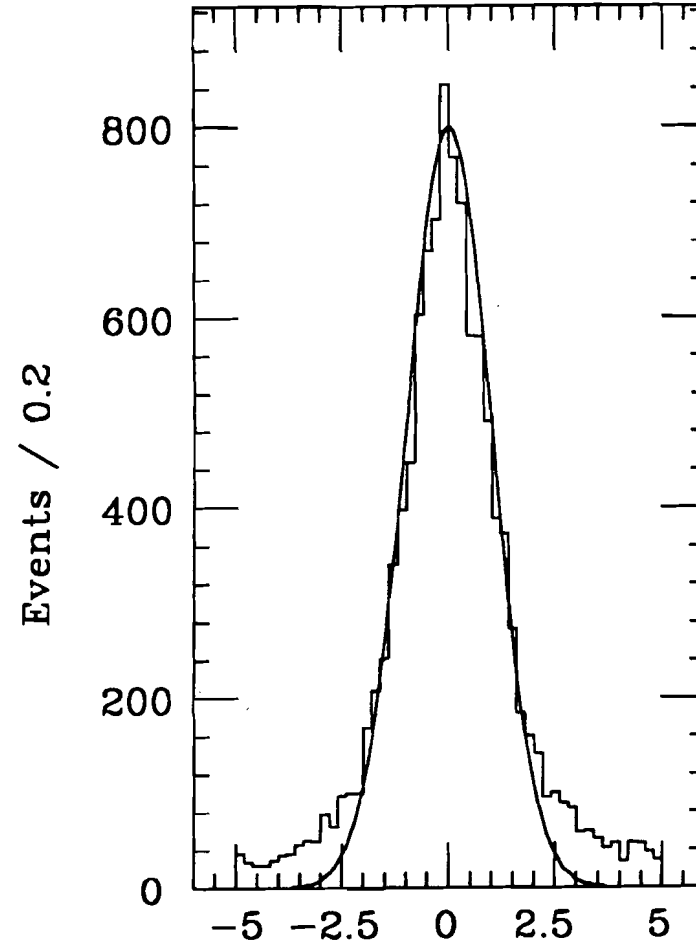(a) L_*/σ, $30 < P < 50$ Gev

(b) L_*/σ, $P > 100$ Gev

Figure D.2:   Normalized deviation for background $D^o \to K\,\pi$ is compared to a unit Gaussian, (a) and (b), and 1.6 times a unit Gaussian, (a).

References

1. E. Fermi, *Nuovo Cimento* **11** (1934) 1.

2. E. Fermi, *Z. Phys.* **88** (1934) 161.

3. S.L. Glashow, *Nucl. Phys.* **22** (1961) 579.

4. S. Weinberg, *Phys. Rev. Lett.* **19** (1967) 1264.

5. A. Salam, *Elementary Particle Theory* ed. N Svartholm (Stockholm: Almqvist, Forlag A B) p367.

6. S.L. Glashow, J. Iliopoulos, and L. Maiani, *Phys. Rev.* **D2** (1970) 1285.

7. J.E. Augustin et al., *Phys. Rev. Lett.* **33** (1974) 1406.

8. J.J. Aubert et al., *Phys. Rev. Lett.* **33** (1974) 1404.

9. G. Goldhaber et al., *Phys. Rev. Lett.* **37** (1976) 255.

10. J.E. Wiss, Ph.D. thesis, University of California, Berkeley (1977).

11. Particle Data Group, Review of Particle Properties, *Phys. Lett.* **170B** (April 1986).

12. J.R. Raab et. al., *Phys. Rev.* **D37** (1988) 2391.

13. M.B. Einhorn and S.D. Ellis, *Phys. Rev.* **D12** (1975) 2007.

14. C.E. Calrson and R. Suaya, *Phy. Rev.* **D14** (1976) 3115.

15. L.M. Jones and H.W. Wyld, *Phys. Rev.* **D17** (1978) 1782.

16. R.K. Ellis and C. Quigg, A Pinacoteca of Cross Sections For Hadroproduction of Heavy Quarks, FNAL preprint FN-445/2013.000, January 1987.

17. J. Gunion, *Phys. Rev.* **D10** (1974) 242.

18. G. Farrar, *Nucl. Phys.* **B77** (1974) 429.

19. V. Barger et al., *Phys. Lett.* **91B** (1980) 253.

20. S.D. Holmes, W. Lee, and J.E. Wiss, *Ann. Rev. Nucl. Part. Sci.* **35** (1985) 397.

21. R.K. Ellis and J.C. Sexton, Explicit formula for heavy flavour production, FERMILAB-Pub-86/111-T, (August 1986).

22. P. Chauvat et al., *Phys. Lett.* **199B** (1987) 304.

23. P. Coteus et al., *IEEE Trans. on Nucl. Sci.* **32**, 1, (1985) 585.*

24. T.F. Droege et al., *IEEE Trans. on Nucl. Sci.* **25**, 1, (1978) 698.*

25. D.J. Harding et al., *IEEE Trans. on Nucl. Sci.* **30**, 5, (1983) 3907.*

26. D.J. Harding et al., *IEEE Trans. on Nucl. Sci.* **30**, 5, (1983) 3768.*

27. P.R. Avery, Ph.D. thesis, University of Illinois, Urbana-Champaign (1980).

28. J.J. Russell, Ph.D. thesis, University of Illinois, Urbana-Champaign (1980).

29. M.J. Lamm, Ph.D. thesis, University of Illinois, Urbana-Champaign (1983).

30. J.E. Filaseta, Ph.D. thesis, University of Illinois, Urbana-Champaign (1987).*

31. C. Shipbaugh, Ph.D. thesis, University of Illinois, Urbana-Champaign (1988).*

32. J. Enagonio, Ph.D. thesis, University of Colorado, Boulder (1987).*

33. R.D. Field and R.P. Feynman, *Nucl. Phys.* **B136** (1978) 1.

34. J.P. Cumalat and C. Shipbaugh, et al., *Phys. Lett.* **210B** (1988) 253.*

35. H. Albrecht et al., *Phys. Lett.* **210B** (1988) 267.

36. R. Ammar et al., *Phys. Rev. Lett.* **61** (1988) 2185.

37. J. Adler et al., *Phys. Rev. Lett.* **60** (1988) 89.

38. D.S. Barton et. al., *Phys. Rev.* **D27** (1983) 2580.

39. H. Dijkstra et al., *Z. Phys. C.* **31** (1986) 375.

40. J. Wiss and J. Wilson, Magnetic Parameter Update, *E687 Memo*, Jan. 3, 1989

41. R. Ammar et al., *Phys. Lett.* **178B** (1986) 124.

Other E400 Publications

Denoted above by *

- P. Coteus et al., *Phys. Rev. Lett.* **59** (1987) 1530.

- M. Diesburg et al., *Phys. Rev. Lett.* **59** (1987) 2711.

- C. Shipbaugh et al., *Phys. Rev. Lett.* **60** (1988) 2117.

- R. Ladbury, Ph.D. thesis, University of Colorado, Boulder (1988).

Vita

██

███. He attended The Ohio State University and earned the degree of Bachelor of Science in Engineering Physics in 1981. While at Ohio State, he was an Undergraduate Research Participant at Argonne National Laboratory during the fall of 1979 and investigated isotopic-safeguard techniques for nuclear reactors. Since August, 1981 he has held teaching and research assistantships in the Physics Department at the University of Illinois at Urbana-Champaign.